Università degli studi di Bologna

Facoltà di Scienze Matematiche Fisiche e Naturali

Dottorato di Ricerca in Fisica

XXI ciclo

Reconstruction of CNGS neutrino events in the emulsions of the OPERA experiment

Author: **Michele Pozzato**

Advisors:

Prof. Giorgio Giacomelli

Dott. Gianni Mandrioli

PhD Coordinator:

Prof. Fabio Ortolani

Bologna, Marzo 2009

Contents

Introduction

Neutrino physics and in particular neutrino oscillations is one of the most challenging and important topics in particle physics. There is a convincing evidence for neutrino oscillation provided by many experiments which studied solar and atmospheric neutrinos such as Gallex, Soudan2, MACRO, SuperKamiokande; in particular atmospheric neutrino experiments favour the hypotesis that the oscillation is purely $\nu_\mu \longrightarrow \nu_\tau$.

The final proof for neutrino oscillations should be the detection of a ν_τ in a terrestrial artificial (almost) pure ν_μ beam (appearance experiment). The distinctive feature of charged current (CC) ν_τ interactions is the decay of the short-lived τ lepton with a *kink* or a *multiprong* topology at submillimeter distance from the primary interaction.

The OPERA experiment aims at the direct observation of $\nu_\mu \longrightarrow \nu_\tau$ oscillations in the CNGS (CERN Neutrinos to Gran Sasso) neutrino beam produced at CERN; since the ν_e contamination in the CNGS beam is low, OPERA will also be able to study the sub-dominant oscillation channel $\nu_\mu \longrightarrow \nu_e$.

OPERA is a large scale hybrid apparatus divided in two supermodules, each equipped with electronic detectors, an iron spectrometer and a highly segmented ~0.7 kton target section made of *Emulsion Cloud Chamber* (ECC) units. Each emulsion-lead unit, called brick, is composed of nuclear emulsion films interspaced with Pb sheets. The production and the decay of the τ lepton is observed thanks to the excellent position resolution of nuclear emulsions (the highest spatial resolution tracking detector). The use of the ECC satisfies the need of a large mass, required in long-baseline neutrino experiments, and a high precision tracking capability to detect tracking capability to detect τ decays.

Due to the large amount of emulsion sheets to be analyzed, a high speed automatic system is needed.

In this thesis I briefly discuss neutrino oscillations in the first Chapter and the OPERA experiment in the second Chapter. Nuclear emulsions and the automatic scanning system performances are the subjects of the third and the fourh Chapters. In the last Chapter I'll present the chain from the connection between Target Tracker and bricks up to the vertex reconstruction using events which I have localized in OPERA bricks during the 2008 run.

Chapter 1

Neutrino oscillations

1.1 A brief history of neutrinos

After some controversial results, in 1914 Chadwick established that electrons emitted in β-decay processes have a continous spectrum. The existence of neutrinos was proposed by W. Pauli in 1930 as an attempt to explain the observations done by Chadwick: he postulated the existence of a new neutral particle as a "desperate way out" to save energy conservation. This particle, named "neutron", should have mass "of the same order of magnitude as the electron mass and in any event not larger than 0.01 proton masses", spin 1/2 and a "penetrating power equal or ten times bigger than γ rays"[1].

In 1933-34 the new particle was renamed *neutrino* by Fermi (in his four-fermion theory of β-decay, formulated in analogy with QED) after that the true neutron had been identified in 1932 by Chadwick and after that he solved the problem of spin and statistics of the nuclei[1]; neutrons are heavy and could not correspond to the particle imagined by Pauli.

Until the end of the 40's, physicists tried to measure the recoil of the nucleus during its beta decay. All the measurements were compatible with the hypothesis of only one neutrino emitted with the electron. It became

[1]This reads: exclusion principle (Fermi statistics) and half-integer spin for an odd number of particles; Bose statistics and integer spin for an even number of particles.

clear that a very abundant source of neutrinos and a very sensitive and huge detector were needed to detect neutrinos.

The experimental discovery of the neutrino is due to Cowan and Reines in 1956 [2]; the experiment consisted in a target made of around 400 liters of a mixture of water and cadmium chloride: the electron anti-neutrinos coming from a nuclear reactor interact with the protons of the target, yielding a positron and a neutron (inverse β decay): $\overline{\nu}_e + p \rightarrow n + e^+$.

Following the first experimental discovery, neutrinos were first shown to always have negative helicity (i.e. the spin and momentum are aligned in opposite directions) by measuring the helicity of gamma-rays produced in the radioactive decay of Europium-152 (knowing the nuclear spin states of the parent and daughter nuclei in the decay, the helicities of the photon and of the neutrino must match).

Later it was established that there were two different types of neutrinos, one associated with the electron and one with the muon. A muon neutrino beam was made using the $\pi \rightarrow \mu\nu_\mu$ decays. The ν_μ interacted in a target producing muons and not electrons $\nu_\mu p \rightarrow n\mu^-$[3].

These experiments, along with many others, have experimentally established that ν_μ and ν_e are the neutral partners of the charged leptons (muon and electron) and helped to shape our understanding of weak interactions in the Standard Model.

In e^+e^- collisions at SLAC was found evidence for a third type of lepton τ^- to which was associated a third neutrino ν_τ.

During the sixties and seventies, electron and muon neutrinos of high energy were used to probe the composition of nucleons. Those experiments gave evidence for quarks and established their properties.

In 1970, Glashow, Illiopoulos and Maiani made the hypothesis of the existence of a second quark family, which should correspond to the second family of leptons; this hypothesis was confirmed by american experiments at the end of 1974.

In 1973 neutral currents (neutrino interaction with matter where neutrinos are not transformed into a charged particle like muon or electron) were discovered at CERN and confirmed at Fermilab.

In 1977 the b quark, that is one quark of the third quark family, was discovered at Fermilab, almost at the same time that Martin Perl discovered the τ lepton at SLAC. The corresponding neutrino ν_τ was finally observed experimentally only in 2001 at Fermilab by the E872 experiment (also known as DONUT).

A complete knowledge of weak interactions came after the discoveries of the W and the Z bosons in 1983 at the CERN SPS $\bar{p}p$ collider; in 1989 the study of the Z^0 boson width at LEP allowed to show that only three lepton families (and then three types of neutrinos) exist.

Precision confirmations of the validity of the Standard Model at low and high energy were experimentally given in the 90's at LEP. Even so, the high energy physics community started turning towards the search for physics beyond the Standard Model, in particular for a non zero neutrino mass and on neutrino oscillations.

1.2 Neutrinos in the Standard Model

The Glashow-Weinberg-Salam theory of the electroweak interaction, combined with Quantum Chromo-Dynamics (QCD) is now called the Standard Model (SM) of particle physics; it is one of the greatest achievements of the 20$^{\text{th}}$ century [4]. The particle content, properties and couplings are shown in Tab. 1.1. The fundamental fermions (quarks and leptons) are grouped into three generations of increasing mass. Particle interactions in the Standard Model are mediated by gauge bosons: the photon for the electromagnetic interaction, the $W^\pm$ and Z^0 bosons for the weak interaction and gluons for the strong force.

Prediction of the SM have been confirmed by many precise experiments: the charmed particles, the b and t quarks, the weak neutral current, the mass of the vector bosons $W^\pm$ and Z^0 are all well known.

However, the SM cannot be considered the final theory of elementary particles because, in this theory, gravity is not included, more than 20 arbitrary fundamental parameters remain to be explained (masses of quarks

Quarks

$-\frac{1}{3}$ **d** 3.5−6.0 MeV	$-\frac{1}{3}$ **s** 70−130 MeV	$-\frac{1}{3}$ **b** 4.13−4.37 GeV
$+\frac{2}{3}$ **u** 1.5−3.3 MeV	$+\frac{2}{3}$ **c** 1.16−1.34 GeV	$+\frac{2}{3}$ **t** 169.1−173.3 GeV

Gauge bosons

0 γ 0 eV	± 1 **W** 80.4 GeV
0 **g** 0 eV	0 **Z** 91.2 GeV

Leptons

-1 **e** 0.511 MeV	-1 μ 105.66 MeV	-1 τ 1.777 GeV
0 ν_e <2 eV	0 ν_μ <0.19 MeV	0 ν_τ <18.2 MeV

Higgs

0 **H** >114.4 MeV

Table 1.1: Fundamental fermions and gauge bosons of the Standard Model. Particle masses and charges are given. The particles are grouped into the fundamental fermions (quarks and leptons) and fundamental bosons; the fermions are further grouped into three families.

and leptons, coupling constants, ...), it lacks any explanations of why in nature there exist three generations of quarks and leptons, etc . More general models have been proposed (GUT, Supersymmetry, Superstrings, ...) and many experimental searches for new physics beyond the SM have been performed. At present the only new physics beyond the SM was found by neutrino oscillation experiments. In the SM, neutrinos are massless, electrically neutral, spin 1/2 particles and do not couple to gluons. They only couple to other Standard Model particles via weak interactions mediated by $W^{\pm}$ and Z^0 bosons.

1.3 Mixing in vacuum

At the present we have no understanding of why the observed leptons and quarks have the masses they do. One of the phenomena which can occur beyond the Standard Model considering neutrinos having a non-zero mass is *neutrino mixing*.

Let's consider the neutrino states ν_e, ν_μ, which couple to electrons and muons respectively; they could be linear combinations of neutrino mass eigenstates ν_1 and ν_2 with masses m_1, m_2.

$$\nu_e = \nu_1 \cos\alpha + \nu_2 \sin\alpha \tag{1.1}$$

$$\nu_\mu = -\nu_1 \sin\alpha + \nu_2 \cos\alpha \tag{1.2}$$

Here α is a mixing angle analogous to the Cabibbo angle θ_C and like the Cabibbo angle it must be determined from experiments. This can be done in principle by studying *neutrino oscillations*, in which a beam of electron neutrinos develops a muon neutrino component whose intensity oscillates as it travels through space; similarly a beam of muon neutrinos develops a corrisponding electron neutrino component. To illustrate this we can consider an electron neutrino produced with momentum $\mathbf{p}$ at time t = 0. The initial state is

$$|\nu_e, \mathbf{p}\rangle = \cos\alpha\,|\nu_1, \mathbf{p}\rangle + \sin\alpha\,|\nu_2, \mathbf{p}\rangle \tag{1.3}$$

After a time t this will become

$$a_1(t)\cos\alpha\,|\nu_1, \mathbf{p}\rangle + a_2(t)\sin\alpha\,|\nu_2, \mathbf{p}\rangle \tag{1.4}$$

where

$$a_i(t) = e^{-iE_i t} \tag{1.5}$$

are the oscillating time factors associated with any quantum mechanical stationary state. For $t \neq 0$, Eq.(1.4) doesn't correspond to a pure electron neutrino state but can be rewritten as a linear combination of ν_e and ν_μ states

$$A(t)\,|\nu_e, \mathbf{p}\rangle + B(t)\,|\nu_\mu, \mathbf{p}\rangle \tag{1.6}$$

where the muon neutrino state is

$$|\nu_\mu, \mathbf{p}\rangle = -\sin\alpha\,|\nu_1, \mathbf{p}\rangle + \cos\alpha\,|\nu_2, \mathbf{p}\rangle \tag{1.7}$$

The functions $A(t)$, $B(t)$ can be found substituting the inverse of the neutrino states into Eq.(1.4):

$$A(t) = a_1(t)\cos^2\alpha + a_2(t)\sin^2\alpha$$
$$B(t) = \sin\alpha\cos\alpha[a_2(t) - a_1(t)]$$

The probability of finding a muon neutrino is

$$P(\nu_e \to \nu_\mu) = |B(t)|^2 = \sin^2(2\alpha)\sin^2[(E_2 - E_1)t/2] \tag{1.8}$$

and thus oscillates with time, while the probability of finding an electron neutrino is reduced by a corresponding oscillating factor, and becomes

$$P(\nu_e \to \nu_e) = |A(t)|^2 = 1 - \sin^2(2\alpha)\sin^2[(E_2 - E_1)t/2] \tag{1.9}$$

Similar effects are predicted even if we start from muon neutrinos; however, in both cases, the oscillations vanish if the mixing angle is zero or if the neutrinos have equal masses (and hence equal rest energies). Of course these oscillation are not possible if both neutrinos have zero masses. The oscillation probability between two neutrinos flavour can also be written in the form below:

$$P(\nu_l \to \nu_l') = \sin^2(2\alpha)\sin^2\left(1.27\frac{|\Delta m^2|\,L}{E}\right) \tag{1.10}$$

The oscillation probability is thus a periodic function of L/E where L is the distance between the neutrino source and the detector measured in km and E is the neutrino energy measured in GeV. The quantity $\Delta m^2 = m_2^2 - m_1^2$ has to be expressed in eV^2.

If we consider three neutrino families the mixing matrix is parametrized by three angles, denoted as θ_{12},θ_{13},θ_{23}, a phase δ due to a possible CP violation ad two Majorana phases α_1,α_2. The last two phases had to be added to take into account the possible Majorana nature of neutrinos even if they can't be observed through oscillations because they don't contribute to the transition probability. If we denote s and c respectively the sine and the cosine functions, the unitary mixing matrix is one below:

$$\begin{pmatrix} \nu_e \\ \nu_\mu \\ \nu_\tau \end{pmatrix} = \begin{pmatrix} c_{12}c_{13} & s_{12}c_{13} & s_{13}e^{i\delta} \\ -s_{12}c_{23} - c_{12}s_{23}s_{13}e^{i\delta} & c_{12}c_{23} - s_{12}s_{23}s_{13}e^{i\delta} & s_{23}c_{13} \\ s_{12}s_{23} - c_{12}c_{23}s_{13}e^{i\delta} & -c_{12}s_{23} - s_{12}c_{23}s_{13}e^{i\delta} & c_{23}c_{13} \end{pmatrix} \begin{pmatrix} e^{i\alpha_1/2}\nu_1 \\ e^{i\alpha_2/2}\nu_2 \\ \nu_3 \end{pmatrix}$$

θ_{12} is conventionally associated to solar neutrino oscillations, so the masses m_1, m_2 differ each other by the quantity $\Delta\mathrm{m}^2_{\mathrm{sol}}$. The angle θ_{23} is associated to the atmosferic neutrino oscillations: so the difference between m_2 and m_3 is denoted by $\Delta\mathrm{m}^2_{\mathrm{atm}}$. Now m_3 could be greater or less than m_1 and m_2, the former is called *normal hierarchy*, the latter *inverted hierarchy*.

The determination of the angle θ_{13} should give indication about the correct mass hierarchy with some phenomenologic results: $\theta_{13} \neq 0$ would indicate CP violation in the lecptonic sector and would have some strong implication in the study of the matter-antimatter asymmetry.

1.4 MSW effect

If we consider a neutrino beam pruduced by an accelerator and directed to a detector some km away from the source, this beam travels through matter and not in the vacuum. So the oscillation probability expression has to be modified according to this. As a first approssimation we can assume that this kind of interaction mantains the flavour (as foreseen by the SM). Interaction with matter could take place in two different ways. The first one could happen only for a ν_e which can interact with an electron through the exchange of the boson W. This scattering give an extra-term to the potential energy of interaction for ν_e in matter:

$$V_W = +\sqrt{2}G_F N_e \tag{1.11}$$

where G_F is the Fermi constant and N_e is the medium electronic density. If we consider an anti-neutrino beam the sign of the potential V_W is negative. The second one consists into the exchange of the boson Z with an electron, proton or neutron and is flavour independent. If the matter is electrically neutral (thus the electron density is equal to the proton one) the electronic contribution erases the one due to protons. As a consequence the extra-term to the potential energy will depend only from the neutron density:

$$V_Z = -\frac{\sqrt{2}}{2} G_F N_n \tag{1.12}$$

where the sign is reversed if we consider an anti-neutrino beam.

The flavor change inside matter is called **Mikheyev-Smirnov-Wolfenstein effect** (MSW). The neutrino propagation through matter could be well described by a Schrödinger equation; the hamiltonian is obtained by the sum of the vacuum term with both terms above. It could be demonstrated [5] that

$$H_M = \frac{\Delta m^2}{4E} \begin{pmatrix} -(\cos 2\theta - x) & \sin\theta \\ \sin\theta & \cos 2\theta - x \end{pmatrix} \tag{1.13}$$

where the parameter

$$x \equiv \frac{V_W/2}{\Delta m^2/4E} = \frac{2\sqrt{2} G_F N_e E}{\Delta m^2} \tag{1.14}$$

gives a measurement of MSW-effect importance related to Δm^2. From the last equation it is clear that x is proportional to the neutrino energy.

In the case of *normal hierarchy* x is positive for neutrinos and negative for anti-neutrinos; these signs are reversed for *inverted hierarchy*. There is an asymmetry between ν and $\bar{\nu}$ oscillations due to MSW-effect and not related purely to CP violation. The study of such asymmetry could help to determinate the neutrinos hierarchy. Defining

$$\Delta m_M^2 \equiv \Delta m^2 \sqrt{\sin^2 2\theta + (\cos 2\theta - x)^2} \tag{1.15}$$

$$\sin^2 2\theta_M \equiv \frac{\sin^2 2\theta}{\sin^2 2\theta + (\cos 2\theta - x)^2} \tag{1.16}$$

the oscillation probability bettwen two different flavours in matter is

$$P(\nu_l \to \nu_l') = \sin^2(2\theta_M) \sin^2\left(\left|\Delta m^2\right| \frac{L}{4E}\right) \tag{1.17}$$

that has an identical structure to the oscillation probability in vacuum replacing θ and Δm^2 with the values in matter.

1.5 Experimental evidences for massive neutrinos

1.5.1 Neutrino absolute mass determination

All the knowledge about neutrinos absolute masses could come from kinematical studies, experiments on the double beta decay without neutrino emission ($0\nu\beta\beta$) and astrophysical and cosmological considerations. Studies about neutrino oscillations are not interesting from the absolute mass point of view because they give only informations about Δm^2.

Kinematical analysis related to nucleus (or particle) decay with a ν in the finale state permitted to set upper limits to neutrino mass independently from any theoretical model [6]. From the β decay study of ^3H or ^{187}Re it is possible estimate an upper limit on neutrino effective mass defined as:

$$m_\beta^2 = \sum |U_{ei}|^2 m_i^2 \tag{1.18}$$

This kind of analysis can be done using spectrometric or calorimetric experiments. Spectroscopic method is mainly used in tritium decay studies. Among these experiments we can cite **Mainz** [7], **Trotsk** [8] which obtained

$$m_\beta < 2.2\ \mathrm{eV}\,(95\%\mathrm{C.L.}) \tag{1.19}$$

Calorimetric methods are used for ^{187}Re decay studies; we can cite **MANU2** and **MIBETA** realized in Genova and Milano-Como. [9][10]. Up to now the best estimate for neutrino absolute mass is given by (1.20), in the near future, some experiments are planned to investigate the sub-eV region with a sensitivity of 0.2 eV (*KATRIN* and *MARE*) [11] which could give indications about the correct hierarchy mass.

Another way to retrieve information about neutrino absolute mass is to observe a double beta decay without neutrino emission. This process can happen only if neutrinos are massive and if neutrinos are of Majorana type. Indications for this process are presented by some members of **Heidelberg-Moskow** experiment [12] realized at *Laboratori Nazionali del Gran Sasso*, Italy for which

$$0.22 \text{ eV} < |m_{\beta\beta}| < 1.6 \text{ eV} \tag{1.20}$$

To confirm such observation, at least one other experiment has to see the effect: future experiments involved in this "hunt "are NEMO3, Super-NEMO, CUORE, Majorana, GERDA, XMASS, COBRA and others.

Astrophysical and cosmological informations on neutrino masses come from CMB (Cosmic Microwave Background) and studies of the universe large scale structure (LSS). The limit obtained from these studies is

$$\sum m_k < 0.2 \text{ eV} \, (2\sigma) \tag{1.21}$$

and it depends from cosmological data, from the model choosen and from the number of neutrino types.

1.5.2 Neutrino oscillation studies

The slow development of neutrino physics is mainly due to the problem of building detector with mass and quality suitable for detecting particles with low cross-section ($\sim 10^{-44} \div 10^{-38}\text{cm}^2$). In the fifties and sixties knowledge of neutrino propreties grew thanks to the setting up of nuclear reactors and thanks to particle accelerator which, giving high neutrino flux, reduced the low cross-section problem.

There are different ways to produce neutrinos:

- solar neutrino ν_e with energy less than 10 MeV produced by termonuclear reactions in the center of the Sun;

- ν_μ or $\overline{\nu}_\mu$ beams with energy of ∼10 GeV obtained by pions and kaons fly-decay;

- $\nu_\mu, \overline{\nu}_\mu, \nu_e$ beams with energy of about few tens of MeV coming from the muon and kaon decay, produced with low energy accelerators;

- $\overline{\nu}_e$ with about 1 MeV energy produced by β^- decay coming from reactors;

- $\nu_\mu, \overline{\nu}_\mu, \nu_e, \overline{\nu}_e$ fluxes produced by primary cosmic rays interacting with atmosphere. The energy spectrum ranges from few hundred MeV up to TeV;

- neutrinos emitted by stars during Super-Novae gravitational collapses.

Experiments to detect neutrinos with beam-experiments can be grouped into two classes depending on what value of L you want to investigate. The first class is called *short-baseline* (SBL) where the distance between source and detector is up to some km; the second class is called *long-baseline* where the distance is hundreds of kilometers.

1.5.3 Solar neutrinos

According to the Solar Standard Model (SSM), all the solar energy is produced in a series of thermonuclear reactions and decays at the center of the sun (Fig. 1.1).

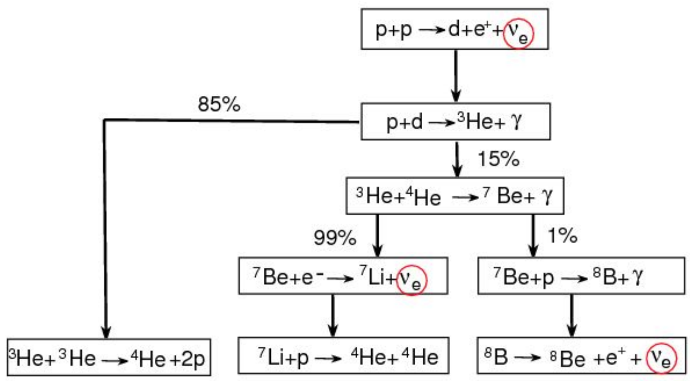

Figure 1.1: The solar processes with relative percentage probabilities for the various chains.

Neutrinos escape quickly from the sun, while the emitted photons suffer an enormous number of interactions and reach the sun surface in about one million years undergoing to an energy degradation (from ~MeV to ~eV).

An important fraction of the energy of the sun is emitted in the form of ν_e energies from 0.1 to 14 MeV (Fig. 1.2).

Solar neutrino studies offer a unique tool to probe for neutrino oscillations at very small Δm^2.

Most of the emitted neutrinos come from the $p+p \rightarrow d+e^+ +\nu_e$ reaction, which yields ν_e's with energies $0 < E_{\nu_e} < 0.42$ MeV; they have interaction cross-sections of $\sim 10^{-45}$ cm^2. The highest energy neutrinos, coming from ^{8}B, have energies $0 < E_{\nu_e} < 14.06$ MeV and cross-sections $\sim 3 \times 10^{-43}$ cm^2. On Earth should arrive $\sim 7 \times 10^{10}$ ν_e cm^{-2} s^{-1}.

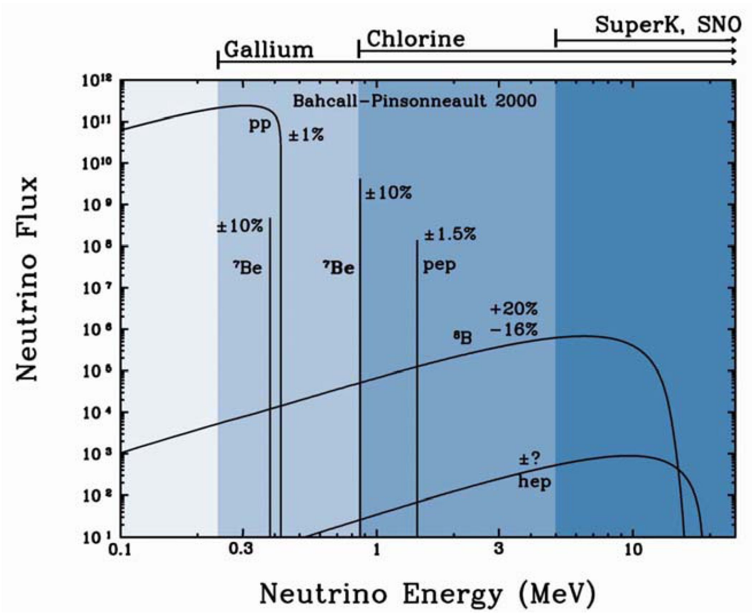

Figure 1.2: The energy spectrum of solar neutrinos produced by various processes in the sun. Also shown is the energy range covered by various experimental techniques.

There are two types of solar neutrino experiments: radiochemical experiments (Homestake, Sage, Gallex, GNO) and scattering experiments (νe^-) (Super-Kamiokande and SNO). The Homestake experiment in the Homestake mine in Lead, South Dakota detects solar neutrinos through the process $\nu_e +^{37} Cl \rightarrow^{37} Ar + e^-$; this experiment is sensitive to solar neutrinos above 814 keV produced by ^8B decay and from electronic capture by ^7Be (see Fig.

1.2). Experimental results with ^{37}Cl indicated a ν_e flux near 1/3 of the flux predicted by SSM. The gallium experiments, Sage, Gallex, GNO use the process $\nu_e +^{37} Ga \rightarrow^{37} Ge + e^-$ (Charged Current interaction), which has a lower threshold allowing the experiment to detect the primary pp neutrinos with energies down to 233 keV. Gallex worked between 1991 and 1997 with a 30 ton detector; the same detector was used by the GNO collaboration up to Genuary 2003. Solar neutrinos interaction rate has been found to be $69.3 \pm 4.1\,(\mathrm{stat}) \pm 3.6\,(\mathrm{sist})\,\mathrm{SNU}(1\sigma)$ [2] The predicted ν_e interaction rate over ^{71}Ga energy ranges from 125 to 140 SNU depending on the model taken into account.

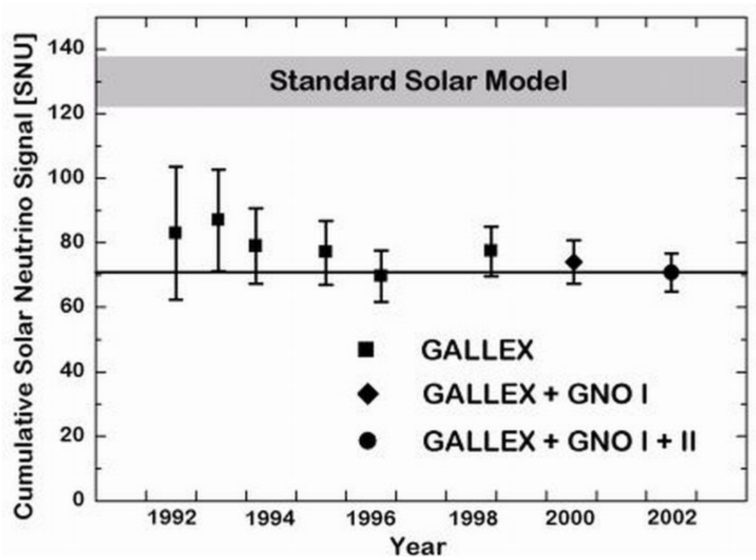

Figure 1.3: Gallex and GNO combined results; the deficit from theoretical flux is well visible.

The Super-K experiment uses the elastic scattering process, $\nu + e^- \rightarrow \nu + e^-$, in a 22.5 ktons fiducial mass water detector to measure the solar flux above 5 MeV. This process has good directional information and shows a clear angular peak pointing toward the sun. The Sudbury Neutrino Observatory (SNO) used 1 kton of heavy water as a target. SNO detected ^{8}B solar neutrinos through the reactions:

[2] 1 SNU (Solar Neutrino Unit) = 10^{-36} captures per second per absorber nucleus.

$$\begin{aligned} \nu_e + d &\rightarrow p + p + e^- &&\text{SNO CC} \\ \nu_x + d &\rightarrow p + n + \nu_x &&\text{SNO NC} \\ \nu_x + e^- &\rightarrow \nu_x + e^- &&\text{Super-K and SNO} \end{aligned}$$

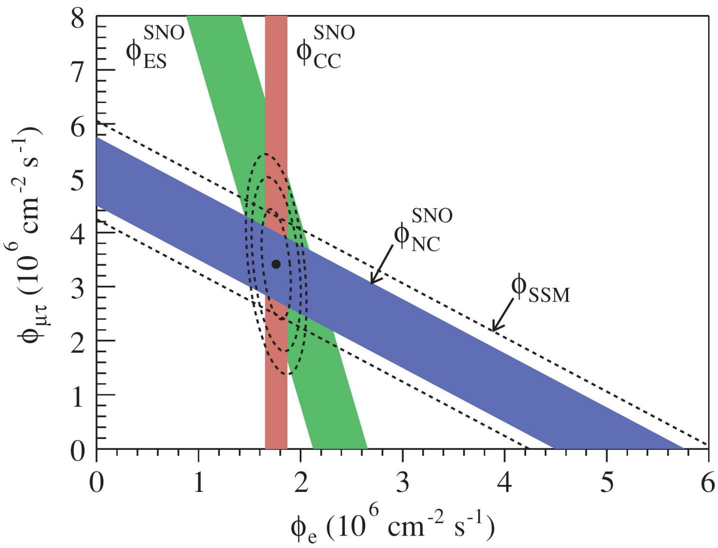

Figure 1.4: (Color)Flux of ^8B solar neutrinos that are μ or τ flavour vs flux of electron neutrinos from three neutrino reactions in SNO. The diagonal bands show the total ^8B flux as predicted by th SSM (dashed line) and that measured with the NC reaction in SNO (solid band). The intercepts of these bands with the axes represent th $\pm 1\sigma$ errors. The bands intersect at the fit values for ϕ_e and $\phi_{\mu\tau}$, indicating that the combined flux results are consistent with neutrino flavour transformation with no distortion in the ^8B neutrino energy spectrum.

The charged current reaction (CC) is sensitive only to ν_e, while the NC reaction is equally sensitive to all active neutrino flavours ($x = e, \mu, \tau$).

The elastic scattering reaction (ES) is sensitive to all flavours, but with reduced sensitivity to ν_μ and ν_τ. Sensitivity to the three reactions allowed SNO to determine the electron and non-electron neutrino components of the solar flux.

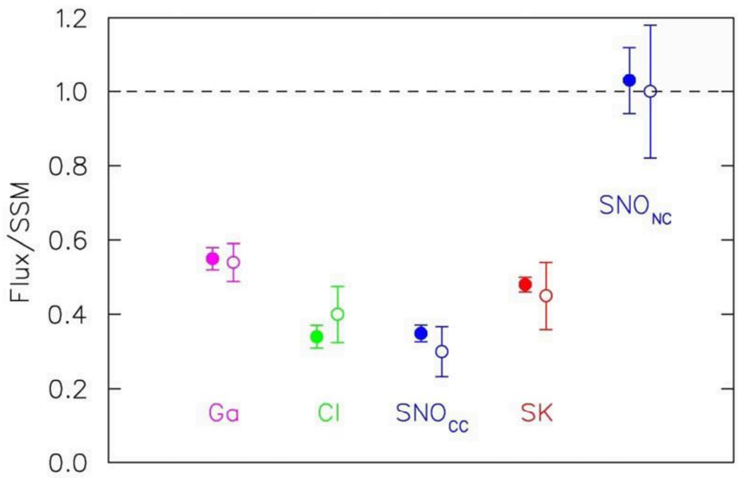

Figure 1.5: Solar neutrino flux compared with SSM (without neutrino oscillation) for some experiments. Filled points are experimental data (uncertanties are only the experimental ones) while the empty ones are the theoretical values predicted by the SSM with the best fit parameters coming from KamLAND and from solar neutrino data (combining uncertanties from SSM and from fit on oscillations). All CC experiments show a deficit and are in agreement with expected values.

The fluxes of ^{8}B neutrinos for $E_{\rm eff} \geq 5$ MeV are (10^6 cm^{-2}s^{-1}):

$$\phi_{CC} = 1.76^{+0.06+0.09}_{-0.05-0.09}, \quad \phi_{ES} = 2.39^{+0.24+0.12}_{-0.23-0.12}, \quad \phi_{NC} = 5.09^{+0.44+0.46}_{-0.43-0.43} \qquad (1.22)$$

The fluxes of electron neutrinos, ϕ_e, and of $\nu_\mu+\nu_\tau$, $\phi_{\mu\tau}$, are (10^6 cm^{-2}s^{-1}):

$$\phi_e = 1.76^{+0.05+0.09}_{-0.05-0.09}, \quad \phi_{\mu\tau} = 3.41^{+0.45+0.48}_{-0.45-0.45} \qquad (1.23)$$

The errors on the flux values are comprehensive of statistical errors (the 1st ones) and systematical errors (the 2nd ones).The flux $\phi_e + \phi_{\mu\tau}$ is that expected from the Standard Solar Model. Combining statistical and systematic uncertainties in quadrature, $\phi_{\mu\tau}$ is $3.41^{+0.66}_{-0.64}$, which is 5.3σ above zero, providing evidence for neutrino oscillations $\nu_e \to \nu_\mu, \nu_\tau$ with $\Delta m^2 \simeq 5.0 \times 10^{-5}$ eV^2, $\sin^2 2\theta \simeq 0.833$.

1.5.4 Atmosferic neutrinos

Atmospheric neutrinos are produced in the decay of secondary particles, mainly pions and kaons, created in the interactions of primary cosmic rays with the nuclei (N) of the Earth's atmosphere. The ratio of the numbers of muon to electron neutrinos is about

$$R = \frac{N_{\nu_\mu} + N_{\bar{\nu}_\mu}}{N_{\nu_e} + N_{\bar{\nu}_e}} = \simeq 2$$

The exact value of R can be affected by several effects, such as the primary energy spectrum and composition, the geomagnetic cut-off, the solar activity and the details of the model for the development of the hadronic shower in atmosphere. However, although the absolute neutrino flux is rather badly known (predictions from different calculations disagree by $\simeq 20\%$), the ratio R is known at $\simeq 5\%$. Neutrino oscillations could manifest as a discrepancy between the measured and the expected value of the ratio R.

Atmospheric neutrinos are well suited for the study of neutrino oscillations, since they have energies from a fraction of GeV up to more than 100 GeV and they travel distances L from few tens of km up to 13000 km; thus L/E_ν ranges from ~ 1 km/GeV to $\sim 10^5$ km/GeV.

One may consider that there are two sources for a single detector: a near one (downgoing neutrinos) and a far one (upgoing neutrinos).

In the no-oscillation hypothesis, the zenith angle distribution must be up-down symmetric, assuming no other phenomena affecting the neutrino angular distribution relative to the local vertical direction. Conversely, any deviation from up-down symmetry could be interpreted as an indication for neutrino oscillations.

Several large underground detectors, located below a cover of 1-2 km of rocks, studied (and are studying) atmospheric neutrinos. The Soudan 2 [13], MACRO [14] and SuperKamiokande [15] detectors reported deficits in the ν_μ fluxes with respect to Monte Carlo (MC) predictions and a distortion of the angular distributions, which may be explained in terms of $\nu_\mu \longleftrightarrow \nu_\tau$ oscillations.

Results from the Soudan 2 experiment

The Soudan 2 experiment used a modular fine grained tracking and showering calorimeter of 963 t. It was located ~2100 meters of water equivalent (m.w.e.) underground in the Soudan Gold mine in Minnesota. The bulk of the mass consisted of 1.6 mm thick corrugated steel sheets interleaved with drift tubes. The detector was surrounded by an anticoincidence shield.

An event having a leading, non-scattering track with ionization dE/dx compatible with that from a muon was a candidate CC event of ν_μ flavour; an event yielding a relatively energetic shower was a candidate ν_e CC event. Events without hits in the shield are called *Gold Events*, while events with two or more hits in the shield are called *Rock Events*.

After corrections for cosmic ray muon induced background, the Soudan 2 double ratio for the whole zenith angle range ($-1 \leq \cos\Theta \leq 1$) is $R' = (N_\mu/N_e)_{DATA}/(N_\mu/N_e)_{MC} = 0.68 \pm 0.11_{stat} \pm 0.06_{sys}$ which is consistent with muon neutrino oscillations.

The (L/E_ν) distributions for ν_e and ν_μ charged current events show the expected trend for $\nu_\mu \to \nu_\tau$ oscillation. The ν_e data agree with the no oscillation MC predictions, while the ν_μ data are lower; this is consistent with oscillations in the ν_μ channel and no oscillations for ν_e.

The 90% C.L. allowed region in the $\sin^2 2\theta - \Delta m^2$ plane, computed using the Feldman-Cousins method [16] is shown in Fig. 1.9b, where it is compared with the allowed regions obtained by the SK and MACRO experiments.

Results from the MACRO experiment

The MACRO detector was located in the Gran Sasso Laboratory, at an average rock overburden of 3700 hg/cm^2 [14]. The detection elements were planes of streamer tubes for tracking and liquid scintillation counters for timing.

Events are classified according to energy and directions:

• **Upthroughgoing muons ($E_\mu > 1$ GeV)** They come from interactions in the rock below the detector of ν_μ with $\langle E_\nu \rangle \sim 50$ GeV.

The MC uncertainties arising from the neutrino flux, cross section and

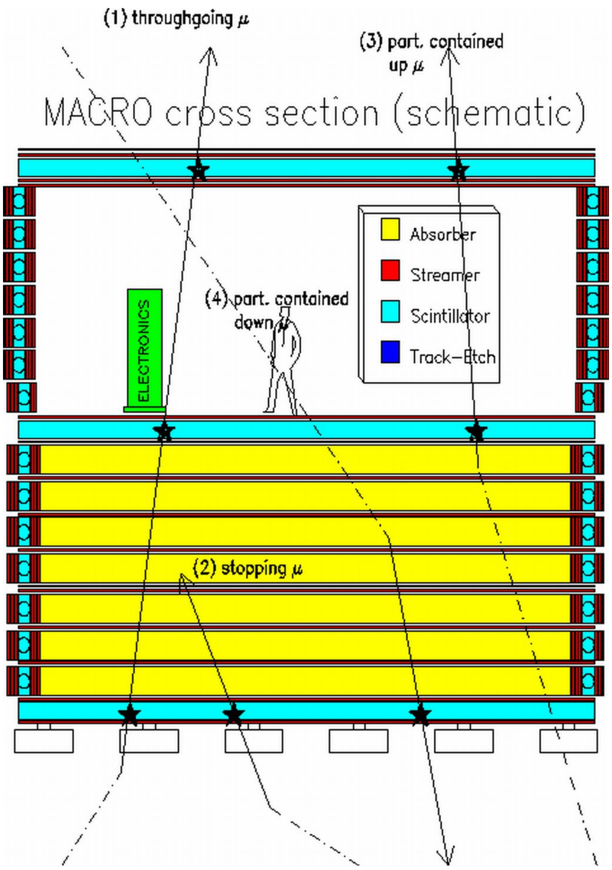

Figure 1.6: Section of the MACRO detector and different event topology induced by ν_μ interactions inside and outside the detector

muon propagation on the expected flux of upthroughgoing muons were estimated to be of ∼17%. In order to verify that different flux simulations affect the zenith distribution at the level of only a few percent (while there is an effect of the order of ąń 25% on the event rates) MACRO compared data with the predictions of the Bartol96 [17], FLUKA [18] and HKKM01 [19], see Fig. 1.7(a). The shape of the angular distribution and the absolute value strongly favour neutrino oscillations with $\Delta m^2 = 0.0023$ eV^2 and maximum mixing.

The absolute values of the MACRO upthroughgoing muon data are 25% higher than those predicted by the FLUKA and HKKM01 MC, while the shapes of the oscillated and non oscillated angular distributions from the different MCs agree within 5%.

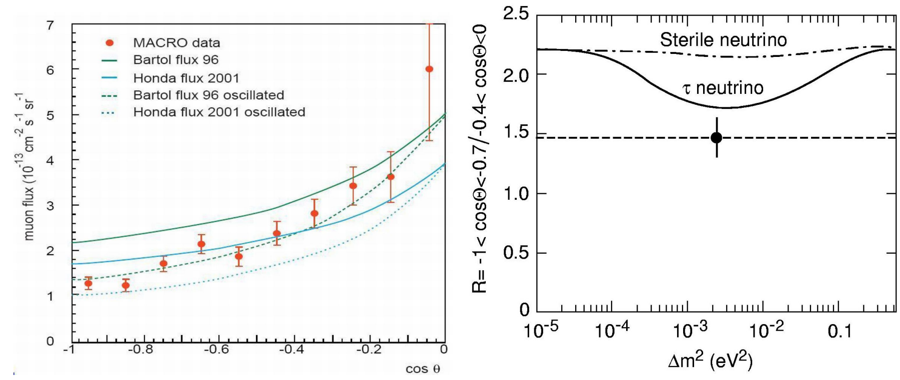

(a) (b)

Figure 1.7: (a) Zenith distribution of the upthroughgoing muons in MACRO. Comparison between data (red points) and prevision done with MC Bartol96 and Honda2001 considering mixing (shaded line) with maximal mixing and $\Delta m^2 = 2.3 \cdot 10^{-3}$ eV^2 and considering no mixing (continuous line). (b) Ratio of events with -1 $< \cos\theta <$ 0.7 to events with -0.4 $< \cos\theta <$ 0 as a function of Δm^2 for maximal mixing. The black point with error bar is the measured value, the solid line is the prediction for $\nu_\mu \rightarrow \nu_\tau$ oscillations, the dash-dotted line is the prediction for $\nu_\mu \rightarrow \nu_{sterile}$ oscillations.

The 90% C.L. allowed region in the $\sin^2 2\theta - \Delta m^2$ plane, computed using the Feldman-Cousins method [16] is shown in Fig. 1.9b, where it is compared with those obtained by the SuperKamiokande and Soudan 2 experiments.

• **Low energy events** *Semicontained upgoing muons* (IU) come from ν_μ interactions inside the lower apparatus. *Up stopping muons* (UGS) are due to external ν_μ interactions yielding upgoing muons stopping in the detector; the semicontained downgoing muons (ID) are due to downgoing ν_μ with interaction vertices in the lower detector; the lack of time information prevents to distinguish between the two subsamples. An almost equal number of UGS and ID events is expected. The average parent neutrino energy for all these events is 2-3 GeV.

The low energy data show a uniform deficit of the measured number of events over the whole angular distribution with respect to the predictions (Bartol96); the data are in good agreement with the predictions based on $\nu_\mu \longleftrightarrow \nu_\tau$ oscillations with the parameters obtained from the upthroughgoing muon sample.

• $\boldsymbol{\nu_\mu \longleftrightarrow \nu_\tau}$ **against** $\boldsymbol{\nu_\mu \longleftrightarrow \nu_{sterile}}$ Matter effects due to the difference between the weak interaction effective potential for muon neutrinos with respect to sterile neutrinos, which have null potential, yield different total number and different zenith distributions of upgoing muons. In Fig. **??**b the measured ratio between the events with $-1 < \cos\Theta < -0.7$ and the events with $-0.4 < \cos\Theta < 0$ is shown [14]. One concludes that $\nu_\mu \longleftrightarrow \nu_{sterile}$ oscillations (with any mixing) are excluded at 99% C.L. compared to the $\nu_\mu \longleftrightarrow \nu_\tau$ channel with maximal mixing and $\Delta m^2 = 2.3 \cdot 10^{-3}$ eV^2.

Results from the SuperKamiokande experiment

SuperKamiokande [15] (SK) is a large cylindrical water Cherenkov detector containing 50 kt of water; it is seen by inner-facing phototubes. The detector is located in the Kamioka mine, Japan, under 2700 *m.w.e.*

Atmospheric neutrinos are detected in SK by measuring the Cherenkov light generated by the charged particles produced in the neutrino CC interactions with the water nuclei. Thanks to the high PMT coverage, the experiment is characterised by a good light yield ($\sim$ 8 photo-electrons per MeV) and can detect events of energies as low as $\sim$ 5 MeV.

Fully contained events can be subdivided into two subsets, the so-called *sub-GeV* and *multi-GeV* events, with energies below and above 1.33 GeV, respectively. In SK jargon FC events include only single-ring events, while *multi-ring* ones (MRING) are treated as a separate category. Another subsample, defined as the *partially contained* events (PC), is represented by those CC interactions where the vertex is still within the fiducial volume, but at least a primary charged particle, typically the muon, exits the detector without releasing all of its energy. For these events the energy resolution is worse than for FC interactions. *Upward-going muons* (UPMU), produced

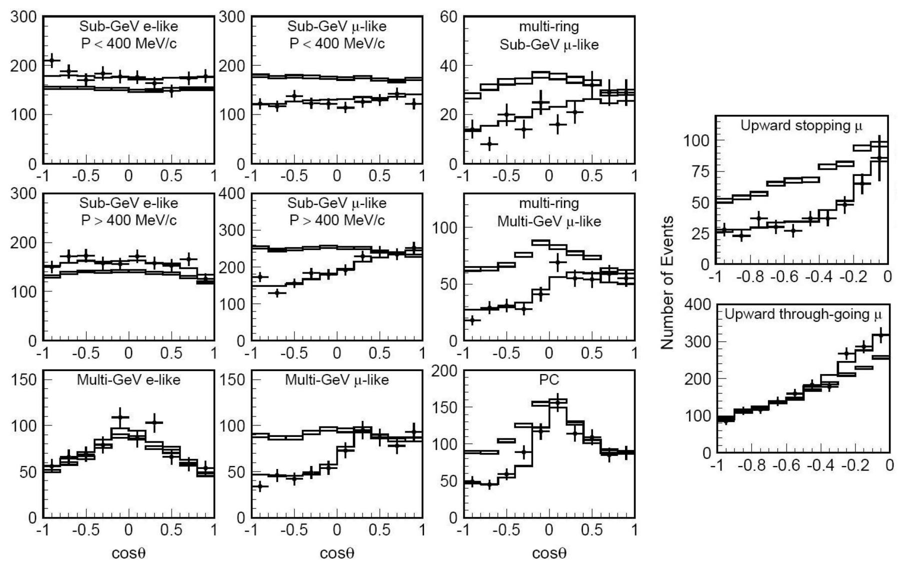

Figure 1.8: Zenith distributions for SK data (black points) for e-like and μ-like sub-GeV and multi-GeV events and for throughgoing and stopping muons. The solid lines are the no oscillation MC predictions, the dashed lines refer to $\nu_\mu \longleftrightarrow \nu_\tau$ oscillations with maximal mixing and $\Delta m^2 = 2.4 \cdot 10^{-3}$ eV^2.

by neutrinos coming from below and interacting in the rock, are further subdivided into *stopping muons* ($\langle E_\nu \rangle \sim 7$ GeV) and *throughgoing muons* ($\langle E_\nu \rangle \sim 70 \div 80$ GeV), according to whether or not they stop in the detector. The samples defined above explore different ranges of neutrino energies.

Particle identification in SuperKamiokande is performed using likelihood functions to parametrize the sharpness of the Cherenkov rings, which are more diffused for electrons than for muons. The algorithms are able to discriminate the two flavours with high purity (of the order of 98% for single track events). The zenith angle distributions for e-like and μ-like sub-GeV and multi-GeV events are shown in Fig. 1.8. The electron-like events are in agreement with the MC predictions in absence of oscillations, while the muon data are lower than the no oscillation expectations. Moreover, the μ-like data exhibit an up/down asymmetry in zenith angle, while no significant asymmetry is observed in the e-like data [15]. More recent value for the double

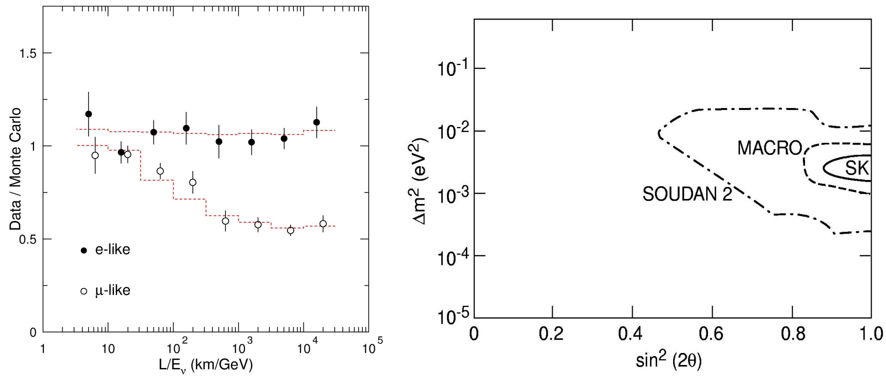

(a) (b)

Figure 1.9: (a) SK ratios between observed and expected numbers of e-like and μ-like events as a function of L/E_ν. (b) 90% C.L. allowed region contours for $\nu_\mu \longleftrightarrow \nu_\tau$ oscillations obtained by the SuperKamiokande, MACRO and Soudan 2 experiments.

ratio R' reported by SK, based on 1289 days of data, is $0.638^{+0.017}_{-0.017} \pm 0.050$ for the sub-GeV sample and $0.675^{+0.034}_{-0.032} \pm 0.080$ for the multi-GeV sample (both FC and PC). The ratio between observed and expected numbers of e-like and μ-like events as a function of L/E_ν is shown in Fig. 1.9a. The ratio e-like events/MC do not depend from L/E_ν while μ-like events/MC show a dependence on L/E_ν consistent with the oscillation hypothesis. Interpreting the muon-like event deficit as the result of $\nu_\mu \longleftrightarrow \nu_\tau$ oscillations in the two-flavour mixing scheme, SuperKamiokande computes an allowed domain for the oscillation parameters [15], see Fig. 1.9b. The events are binned in a multi-dimensional space defined by particle type, energy and zenith angle, plus a set of parameters to account for systematic uncertainties. The best fit using FC, PC, UPMU and MRING events [15] corresponds to maximal mixing and $\Delta m^2 = 2.5 \cdot 10^{-3}$ eV^2, Fig. 1.9b.

SK reported also data on upthroughgoing muons, which agree with the predictions of an oscillated flux with the above parameters.

- **$\nu_\mu \longleftrightarrow \nu_\tau$ against $\nu_\mu \longleftrightarrow \nu_{sterile}$**

If the observed deficit of ν_μ were due to $\nu_\mu \longleftrightarrow \nu_{sterile}$ oscillations, then the number of events produced via neutral current (NC) interaction for up-going neutrinos should also be reduced. Moreover, in the case of $\nu_\mu \longleftrightarrow \nu_{sterile}$ oscillations, matter effects will suppress oscillations in the high energy ($E_\nu > 15$ GeV) region. The following data samples were used to search for these effects: (a) NC enriched sample, (b) the high-energy ($E > 5$ GeV) PC sample and (c) upthroughgoing muons. The excluded regions obtained by a combined ((a),(b)and(c)) analysis and by the analysis of 1-ring-FC show that $\nu_\mu \longleftrightarrow \nu_{sterile}$ oscillations are disfavored with respect to $\nu_\mu \longleftrightarrow \nu_\tau$ oscillations at a C.L. of 99% [15].

All muon data are in agreement with the hypothesis of two flavour $\nu_\mu \longleftrightarrow \nu_\tau$ oscillations, with maximal mixing and $\Delta m^2 \sim 2.5 \cdot 10^{-3}$ eV^2. The hypothesis of $\nu_\mu \longleftrightarrow \nu_{sterile}$ oscillations is disfavoured at 99% C.L. for any mixing. The 90% C.L. contours of Soudan 2, MACRO and SuperKamiokande overlap, see Fig. 1.9b.

1.5.5 Neutrinos from reactors

Nuclear reactors pruduce $\overline{\nu}_e$ through β-decay coming from fission fragments.

KamLAND is a *long baseline* experiment built to detect $\overline{\nu}_e$ produced by a large number of reactors distribuited in a wide area in the middle of Japan; it consists of 1000 tons of liquind scintillator and it is located in the Kamioka mine. Combining the oscillations parameters from the solar neutrinos experiments and KamLAND gives the best-fit parameters $\Delta \mathrm{m}^2 = 8.0^{+0.6}_{-0.4} \cdot 10^{-5}\mathrm{eV}^2$ and $\tan^2\theta = 0.45^{+0.09}_{-0.07}$ (Fig 1.8). This results raises some dubts about MSW effect: KamLAND results are consistent with solar neutrinos even if reactor neutrinos don't go through matter as it happens for solar neutrinos.

LNSD experiment set up in Los Angeles detected neutrinos coming from a 800 MeV linear accelerator and it was 30 m far away from the source; it was made cylindrical tank filled with 167 tons of scintillating liquid. The results of LNSD are the unique clashing note among all other results: as a matter of fact, even if it observed a possible $\nu_\mu \longleftrightarrow \nu_e$ oscillation signal, oscillating parameters are low mixing angle and Δm^2 quite high.

1.5.6 Long Baseline experiments

From the equations about neutrino oscillations it's clear that, in order to explore quite low values of Δm^2, it is necessary to design long baseline experiments with low energy neutrino beam. The first of this kind of experiment was K2K in Japan: muonic neutrinos produced by 12 GeV KEK protosincrotron were detected 250 km far away from the source by SK. If ν_μ oscillates into ν_τ the observed ν_μ flux should be reduced respect to the predicted one (without oscillation). In March 2003 K2K published a first result in which it was claimed that SK observed 56 ν_μ events instead of 80. Another analysis done on February 2004 found 108 muonic events instead of $150.9^{+11.6}_{-10.0}$, supporting the oscillating thesis.

A combined fit with SK data gives $\Delta m^2 = (2.6 \pm 0.4) \cdot 10^{-3} eV^2$ and $\sin^2 2\theta = 1.00^{+0.00}_{-0.05}$.

1.6 Results and perspectives

Up to now data collected by experiments performed with atmosferic, solar, reactor neutrinos lead to the believe that neutrinos are massive and a superimposition of different flavour eigenstates.

Results from all experiments (except for LSND) are consistent with three flavour mixing interpretetion , parametrized by three neutrino masses (m_1, m_2, m_3), three mixing angles $\theta_{12}, \theta_{23}, \theta_{13}$ and a possible phase δ to take into account CP violation. Data fit give **??**:

$$\Delta m^2_{12} = (8.0 \pm 0.3) \cdot 10^{-5} \text{ eV}^2$$
$$\sin^2(2\theta_{12}) = 0.86^{+0.03}_{-0.04}$$
$$\Delta m^2_{32} = 1.9to3.0 \cdot 10^{-3} \text{ eV}^2$$
$$\sin^2(2\theta_{23}) > 0.92$$
$$\sin^2(2\theta_{13}) < 0.19 \text{ CL} = 90\%$$

A conclusive test on neutrino oscillation hypotesis $\nu_\mu \longleftrightarrow \nu_\tau$ which is the most plausible explanation of the observed ν_μ deficit, will be the direct observation of ν_τ starting from a pure ν_μ beam. This is the target of OPERA experiment.

Chapter 2

The OPERA experiment

The **OPERA** experiment (**O**scillation **P**roject with **E**mulsion t**R**acking **A**pparatus) is made in the context of the project **CNGS** (CERN Neutrinos to Gran Sasso) whose main aim is the investigation of neutrino oscillations.

OPERA is a long baseline experiment, designed to observe directly ν_τ's produced by ν_μ oscillations; this will be a conclusive test to understand the oscillation phenomenology. A pure ν_μ beam is produced at CERN from the SPS accelerator (Fig. 2.1) and is detected 730 km away at LNGS where the detector has been assembled. The appearance signal of the occurence of $\nu_\mu \longleftrightarrow \nu_\tau$ oscillations is the CC interaction of ν_τ inside the detector target: $\nu_\tau N \to \tau^- N$. The reaction is identified by the detection of the lepton τ ($c\tau = 87.11\mu$m) in the final state through the decay topologies in its decay modes $\tau^- \to e^- \nu_\tau \overline{\nu}_e$, $\tau^- \to \mu^- \nu_\tau \overline{\nu}_\mu$, $\tau^- \to h^- \nu_\tau (n\pi^0)$. This observation is possible thanks to a massive detector made of lead sheets (absorber) spaced with nuclear emulsions (high resolution tracking detector). For historical reasons the base cell is called *Emulsion Cloud Chamber* (ECC) [12] [20]; in the past this tecnique was used in the DONUT experiment permitting the first direct ν_τ observation. By piling-up a series of cells in a sandwich-like structure one obtains a *brick*, which constitutes the detector element appropriate for filling more massive planar structures (walls). A series of walls plus the related electronic tracker planes and a magnet constitute a *supermodule*.

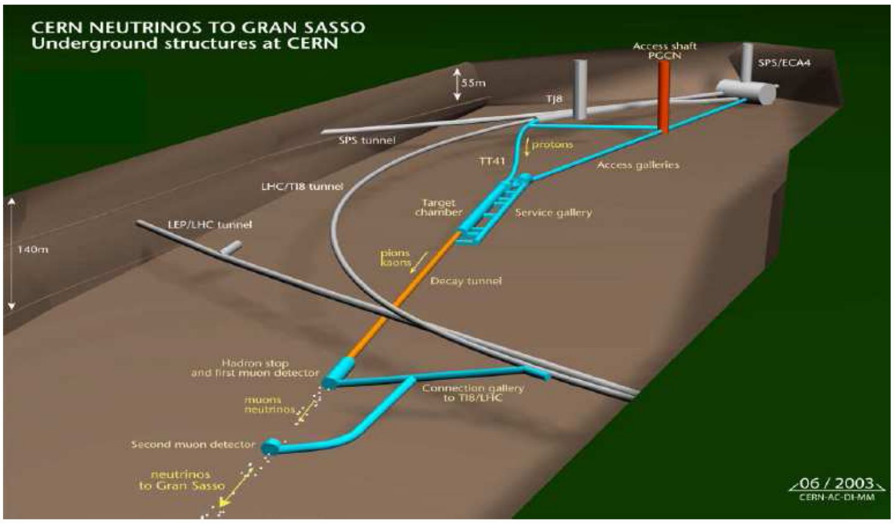

Figure 2.1: Schematic view of the CNGS neutrino beam path at CERN.

OPERA is made of two supermodules, each with a target section, which is a sequence of modules, and a downstream muon spectrometer.

The installation of OPERA in the Hall C of LNGS started in Summer 2003. After completion of the first magnet a support structure was installed in August 2004 to hold the first instrumented target. The installation of the walls started in October 2004 and was completed in May 2006. Detector filling (with more than 150000 bricks) was completed at the beginning of the 2007 run.

2.1 The CNGS beam

The CNGS beam was designed and optimized for the appearance study of ν_τ starting from a pure beam of ν_μ. A schematic layout of the CNGS beam at CERN is shown in (Fig. 2.2). The SPS 400 GeV extracted proton beam hits a graphite target made of rods, for an overall target length of 2m, producing secondary pions and kaons. The target rod diameter is 4 mm so that the proton beam is well contained within the target. The first coaxial lens, the *horn*, starts at 1.7 m from the focus of the proton beam. The second element,

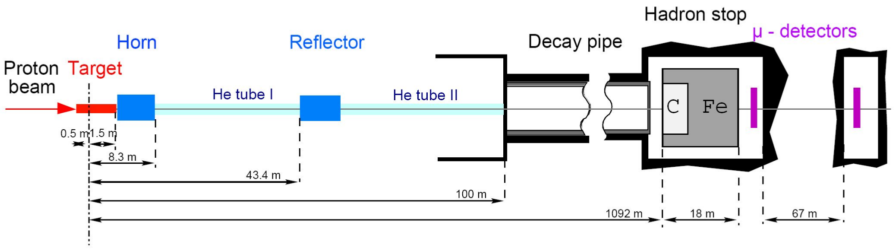

Figure 2.2: Layout of the CNGS beam at CERN. The coordinate origin is the focus of the proton beam.

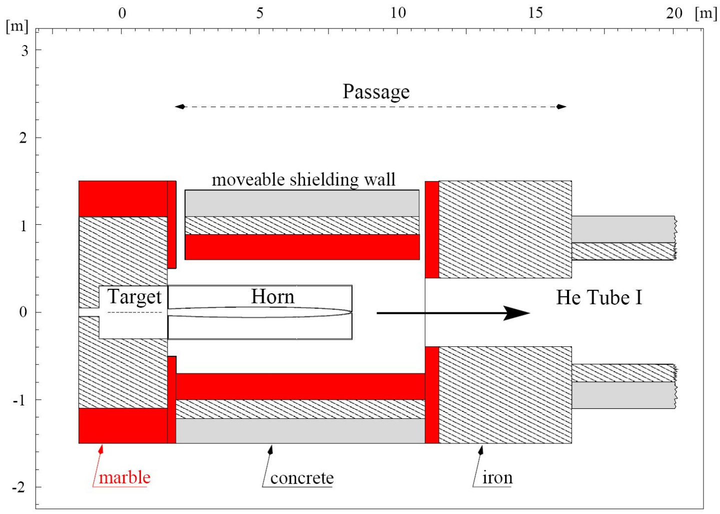

Figure 2.3: Close-up of the region around the target and the horn.

the *reflector*, is 43.4 m downstream of the focus. The nominal current for the horn is 150 kA, for the reflector is 180 kA.

Helium tubes are placed in the free spaces along the beam in order to reduce the interaction probability for secondary hadrons. A first tube is located between the horn and reflector, while a second one fills the gap between the reflector and the beginning of the decay tunnel. A detailed view of the target/horn region is shown in Fig. 2.3.

Pions and kaons focused form a parallel beam in the decay tunnel, where they decay into $\mu + \nu_\mu$. The lenght of the decay is about 1 km. Given the angular distribution of the parent mesons, the longer the decay tunnel the larger must be its diameter. A tunnel of 2.45 m diameter and 1000 m length was chosen for the CNGS. A massive iron hadron stopper is situated at the end of the decay tunnel. The signals induced by muons in two arrays of silicon detectors, the first placed in the hadron stopper and the secondo in the middle of the μ shield, are used for the online monitoring and tuning of the beam (steering of the proton beam on target, horn and reflector alignment). The separation of the two arrays, equivalent to 25 m of iron, allows a rough measurement of the muon energy spectrum and of the beam angular distribution.

ν_μ (m^{-2}/pot)	$7.45 \cdot 10^{-9}$
ν_τ CC events/pot/kton	$5.44 \cdot 10^{-17}$
$\langle E \rangle_{\nu_\mu}$	17
ν_e/ν_μ	0.8%
$\bar{\nu}_\mu/\nu_\mu$	2.0%
$\bar{\nu}_e/\nu_\mu$	0.05%

Table 2.1: Nominal features of the CNGS beam [21].

The mean beam energy $\langle E_{\mu_\nu} \rangle$ is ∼17 GeV, well above the threshold of the lepton τ^- production. The value L/E, ∼43 km/GeV, is high enough to study the region of low Δ m^2.

The sensitivity of the experiment is limited by beam contamination uncertainties. Contamination of ν_τ from D_s decay is negligible and, as it is shown in Tab. 2.1; the contamination due to $\overline{\nu}_\mu$ is 2.0%. ν_e ($\overline{\nu}_e$) contamination is low and allows to investigate the sub-dominant oscillation channel $\nu_\mu \leftrightarrow \nu_e$ [22].

Due to the radius of curvature of the Earth, the neutrinos produced at CERN will arrive at LNGS with an estimated slope of 3 degrees with respect to the horizontal plane. Assuming a proton beam integrated intensity of $4.5 \cdot 10^{19}$ protons on target (p.o.t) per year, during all data taking (about 5 years) OPERA will detect ∼31000 neutrino events due to CC and NC interactions in the target. Assuming $\Delta m^2 = 2{\cdot}10^{-3}$ eV^2 ($3 \cdot 10^{-3}$ eV^2) and maximal mixing, it is expected 95 (214) to be ν_τ CC interactions. Considering the overall efficiency to detect the τ, OPERA should collect $10 - 15$ signal events with less than one background event.

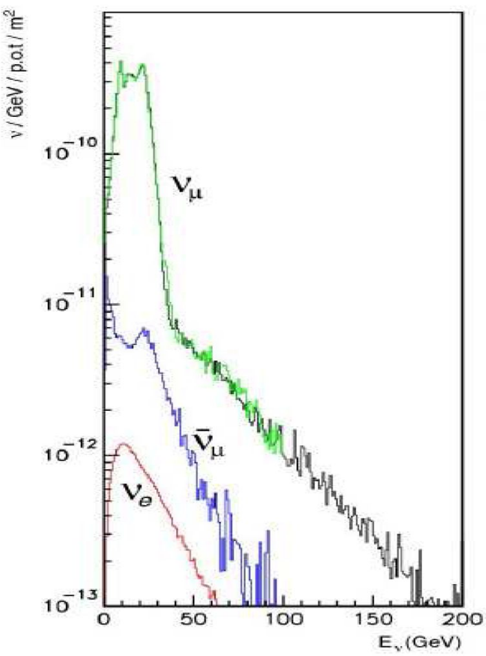

Figure 2.4: Expected neutrino fluxes at LNGS. Two different simulations are reported for the main component (green and black lines)

2.2 The OPERA Detector

The OPERA detector is located in the Hall C in the underground laboratories at LNGS. The detector is a *hybrid* detector composed of electronic detectors and a large amount of nuclear emulsions. The electronic detectors select the brick in which the interactions took place and identify the muon determining also its momentum and charge; nuclear emulsions are used to study in detail the neutrino interactions and to indentify the daughter particles produced.

2.2.1 The Veto

Following the beam line, the first OPERA detector component is the Veto, designed to reduce wrong triggers due to particles produced by neutrino interactions in the rock, in the mechanical structures and in the Borexino detector. Veto is also used to monitor CNGS beam counting muons which pass through it.

The system is composed by two planes of 9.6 x 9.2 m^2 of a glass-RPC matrix, 64 glass-RPC altogether. The two planes are separated by 10 cm, and the whole system is located 2 m from the first Supermodule (**SM1**).

2.2.2 The Target

The target has an overall mass of about 625 ton/Supermodule and it has a modulare structure whose basic cell is made of a sheet of lead (1mm thick) and a thin nuclear eumulsion. The nuclear emulsion films are produced industrially by Fuji Film Co. Ltd. for a total amount of 9 x 10^6 films. Each emulsion film is made of two layers (each with a nominal thickness 44 μm) separated-out by a plastic base (nominal thickness of 200 μm). The used lead has a low percentage of Calcium (~0.04%) to improve mechanical characteristics [24]. An OPERA *brick* is obtained piling up 56 cells and adding an extra-emulsion film. Brick transversal dimensions are 12.7 x 10.2 cm^2, while the total thickness is about 7.5 cm (that means 10 X_0[1]): one brick has a weight of 8.3 kg. Each brick is assembled and wrapped with a special fiberglass tape to avoid light contamination. After this each brick is equipped with a plastic box containing two emulsion sheets kept in contact, called *Changeable Sheets* (CS), see Fig 2.5. The aim of this doublet is to permit a confirmation of the trigger provided by the electronic detectors without developing all the brick [25]. Only if the trigger is confirmed by the CS the brick will be developed, otherwise the CS will be replaced and the brick put back into the detector.

To reduce cosmic-rays background all the bricks are assembled in the

[1] X_0 is the radiation lenght

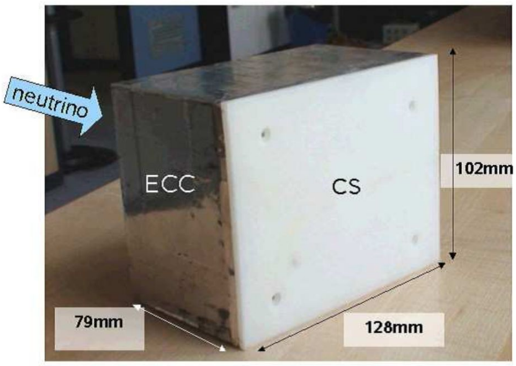

Figure 2.5: Picture of an OPERA-brick.

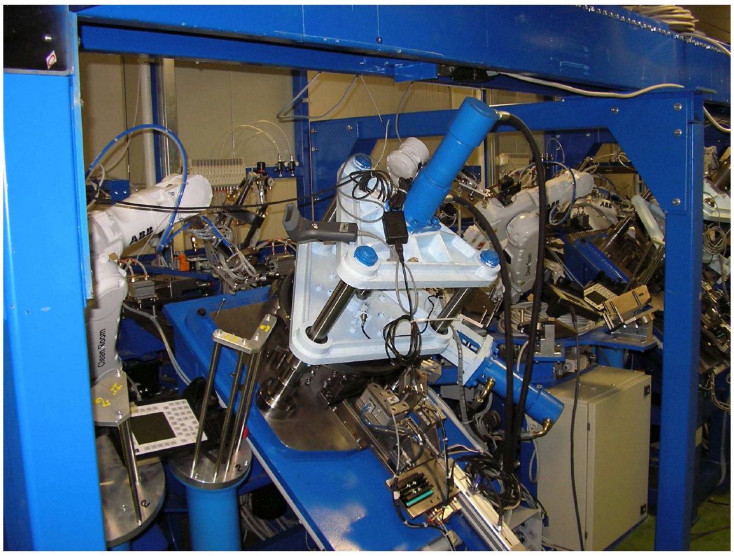

Figure 2.6: One of the five piling and pressing stations of the BAM.

underground laboratories at LNGS. The requested speed in order to accomplish the task of assembling all the bricks in one year is about two bricks per minute: this is achieved by an assembly line done using antropomorphic robots. The *Brick Assembly Machine*(BAM) was designed taking into account the need of a high piling precision and bricks stability over time. It was produced by Tecno-Cut and now it is located between hall A and hall B in the underground laboratories at LNGS (Fig 2.6).

Bricks are mounted into 29 walls of each SM, into a 52 x 51 matrix. Each

Figure 2.7: Lateral view of an OPERA wall.

wall (Fig. 2.7) is an ultra-light stainless-steel structure made of two identical and independent parts called *Semi Wall* (SW) designed to reach a 1 mm precision in the brick location and minimize the amount of passive material around the bricks (mass less then 0.4 % of the total mass). Each SW is made of 27 stainlesssteel ribbons suspended from above and tensioned from below by means of a spring-tensioning system. 64 horizontal trays are welded to the ribbons.

Even for the insertion of the bricks in the structure, is used an automatic system, developed by the Collaboration, called *Brick Manipulator System* (BMS) (Fig 2.8). The BMS is able to put a brick inside a tray with a precision of about 1 mm and to exract the selected bricks in a realtime mode.

In one day of data-taking, the expected number of neutrino interactions (and of selected bricks) is $\sim$30; it is needed a very fast scanning system to analyze the huge amount of nuclear emulsions, and this task is accomplished in two different ways by the European part of the Collaboration and differently from the Japanese side (see the next chapter). In Tab. 2.2 there is a summary of the techinacal of SM specs.

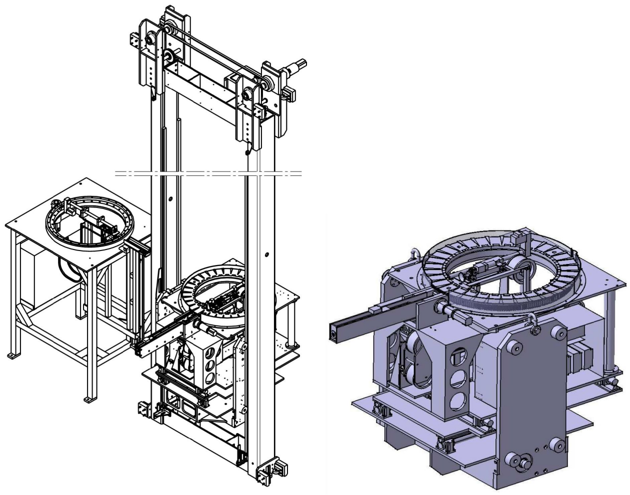

Figure 2.8: Left: drawing of a complete BMS system with its loading station. Right: detailed view of the platform with the varios system allowing the movements of the bricks.

2.2.3 The Target Tracker

Electronic detectors located after each brick wall, are used to select the brick in which neutrino interactions took place. The CS use allows a moderate spatial resolution (reducing electronics costs).

Plastic scintillators coupled with *Wave Length Shifting* (WLS) fibers are chosen to perform this task; they are used to sample hadronic showers energy and contribute to identify and reconstruct high penetrating tracks. Each wall is followed by two planes of electronic trackers ($\sim$ 6.7x6.7 m^2), each of them contains 256 scintillating strips. (Fig. 2.9)

Scintillating strips are 2.6 cm wide and 1 cm thick and have an energy resolution equal to that expexted for sampling calorimeters.

$$\frac{\Delta E}{E} \sim \frac{0.65}{\sqrt{E(\mathrm{GeV})}} + 0.16 \tag{2.1}$$

Each Hamamatsu photomultiplier tubes has 64 channels are connected to fibers. Both sides are read by the photomultiplier. The localization efficiency is limited essentially by back-scattering: particles produced by neutrino in-

OPERA Dimension [m^3]	∼10x10x20
Pb-emulsion thickness [mm]	1.3
Number of emulsion films/brick	57 + 2CS
Brick cross section [cm^2]	12.7 x 10.2
Brick thinkness [cm]	7.5 without packaging
Brick thinkness [X_0]	∼10
Brick mass [kg]	∼8.3
Module thickness [cm]	12
Number of walls/supermodule	29
Max number of bricks/supermodule	77375
Target mass/supermodule [ton]	∼625

Table 2.2: OPERA detector general features.

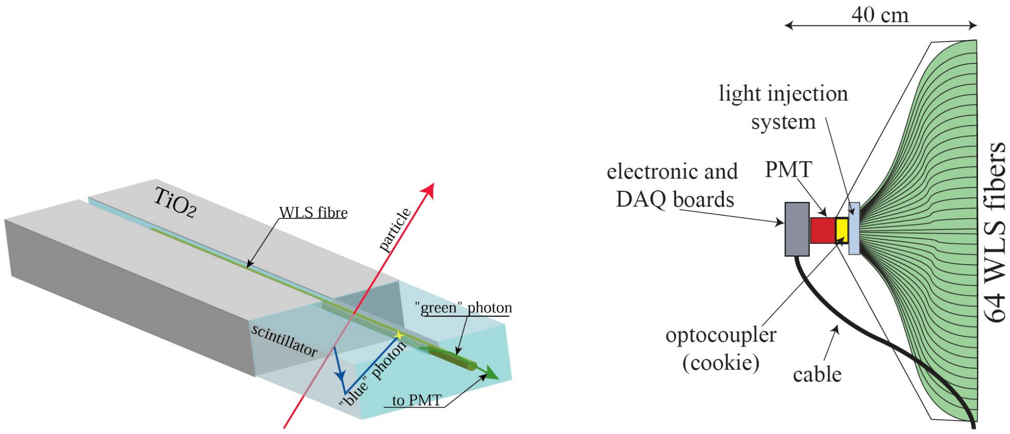

Figure 2.9: Left: Schematic view of a scintillator strip with WLS fiber. Right: Schematic view of a scintillator strip end-cap with the fron end DAQ board.

teractions can reinteract giving particles moving in the opposite direction of the beam. This can be a source of errors in the wall location procedure.

Events with at least one particle back-scattered are mainly caused by *Deep Inelastic Scattering* (DIS) than for *Quasi Elastic* (QE) events; the difference increases with the neutrinos beam energy.

2.2.4 The Muon Spectrometers

The OPERA spectrometers allow to determine pulse and charge of passing-through charged particles measuring deflection in a magnetic field by RPC and drift tube chambers [28]. These informations are very useful in the kinematical reconstrution of ν_μ CC and ν_τ CC events when τ decays in the muon channel. It is also useful to reduce the background due to charmed particle decays (characterized by topology similar to the τ one). Each spectrometer is made of a dipolar magnet (10 x 8.2 m^2 of cross section), carried out by two iron walls, connected by two flux return paths. In the walls (tracking volume), the magnetic field is essentially uniform, with a flux density of 1.55 T. The field lines are vertical and of opposite orientations in the two magnet walls. The walls consist of 12 iron layers 5 cm thick interleaved with RPC's (Inner Trackers), Fig. 2.10. Each iron layer consists of 7 plates placed side by side (12.5 x 82 x 5 cm^3). RPC's are used to reconstruct tracks due to particles stopping inside the iron wall and to give calorimetric measurements of the hadronc component. Each spectrometer is equiped with 6 plates of 48 drift tubes (Precision Trackers), located in front and behind the magnet as well as between the two walls, to measure the muon momentum. Downstream of the magnet there are a couple of RPC (called XPC) to improve angular resolution of entering tracks. XPC strips are tilted 42.6° with respect to the horizontal and vertical planes. The overall tracking efficiency is $\sim$99% and the spatial resolution is $\sim$300 μm.
Muon identification is larger than 95% including TT efficiency. The momentum resolution is near 15% for p $<$ 40 Gev/c and near 20% for higher values of momentum. The mis-determination of muon charge ranges from 0.1% up to 0.3% in the energy range 1-30 GeV [29].

OPERA has a low data rate from events due to neutrino interactions well localized in time, in correlation with the CNGS beam spill. The synchro-

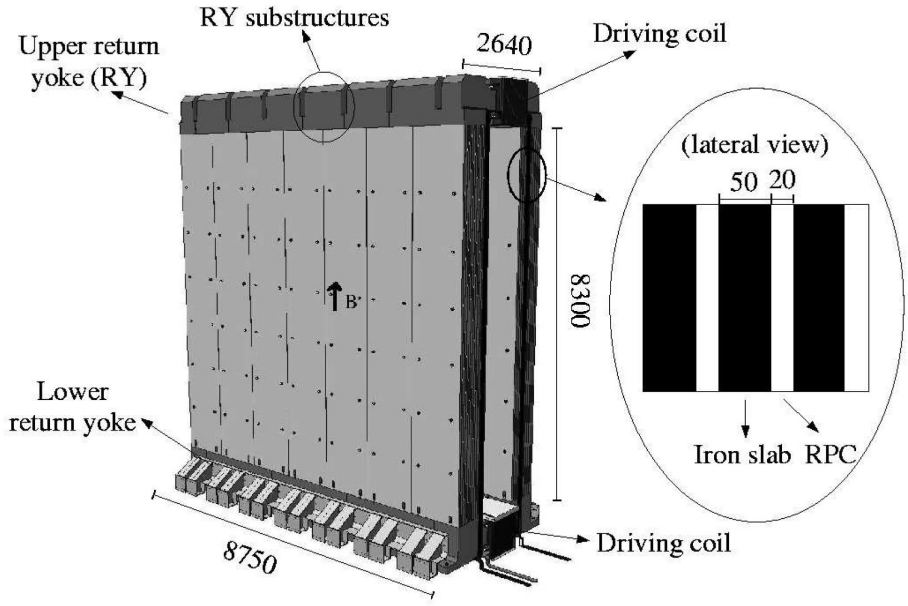

Figure 2.10: Three dimensional view of one OPERA magnet. Units are in mm. The blow-up insert shows the dimensions of three of the twelve layers of an arm.

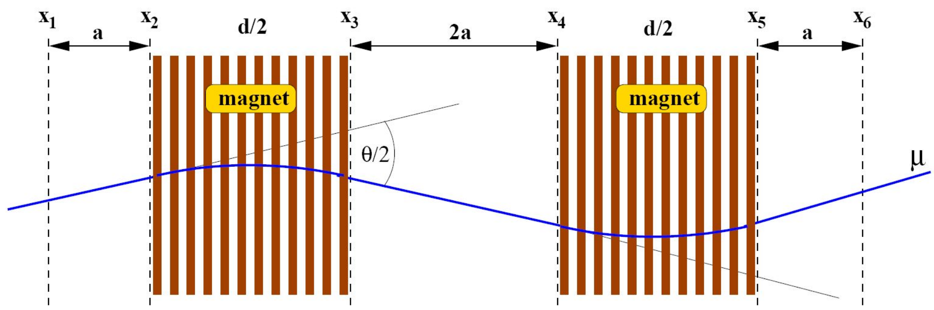

Figure 2.11: Schematic layout of one half of the muon spectrometer. The six drift tube chambers are denoted x_1-x_6. With three chamber pairs the initial momentum can be evaluated from the two indipendent measurements of the deflections of the charged particle in the magnetic field.

nization with the spill is done offline via GPS. The detector remains sensitive during the inter-spill time and runs in a trigger-less mode. Events detected out of the beam spill (cosmic-ray muons, background from environmental radioactivity, dark counts) are used for monitoring.

2.3 Physics performances

2.3.1 τ detection

The signal of the occurrence of $\nu_\mu \leftrightarrow \nu_\tau$ oscillations is the CC interaction of ν_τ's in the detector target ($\nu_\tau N \rightarrow \tau^- X$), through the decay topologies of the τ^- decay modes:

$$\begin{array}{ll}
\tau^- \rightarrow e^- \nu_\tau \overline{\nu}_e & (B.R. = 17.8\%) \\
\tau^- \rightarrow \mu^- \nu_\tau \overline{\nu}_\mu & (B.R. = 17.4\%) \\
\tau^- \rightarrow h^- \nu_\tau (n\pi^0) & (B.R. = 49.5\%) \\
\tau^- \rightarrow \pi^+\pi^-\pi^- \nu_\tau (n\pi^0) & (B.R. = 14.5\%)
\end{array}$$

For the typical τ energies expected with the CNGS beam one obtains the decay length distribution shown in Fig. 2.12.

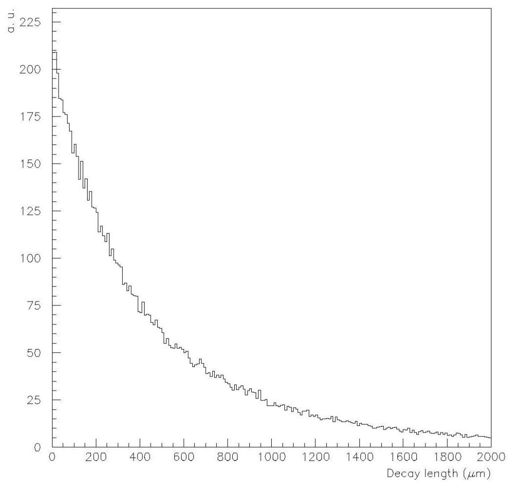

Figure 2.12: τ decay length distribution.

If a τ is produced in a lead plate it will decay either in the same plate (*short decays*) or further downstream (*long decays*). The former will occur in 60% of the times, the latter in 40%.

For long decays, the τ is detected by measuring the angle between the charged decay daughter and the parent τ direction. Fig. 2.14 shows the distribution of the τ decay kink angle for the electron channel. For this measurement the directions of the tracks before and after the kink are reconstructed (in space) by means of the pair of emulsion films sandwiching the lead plate where the decay vertex occurred (Fig. 2.13).

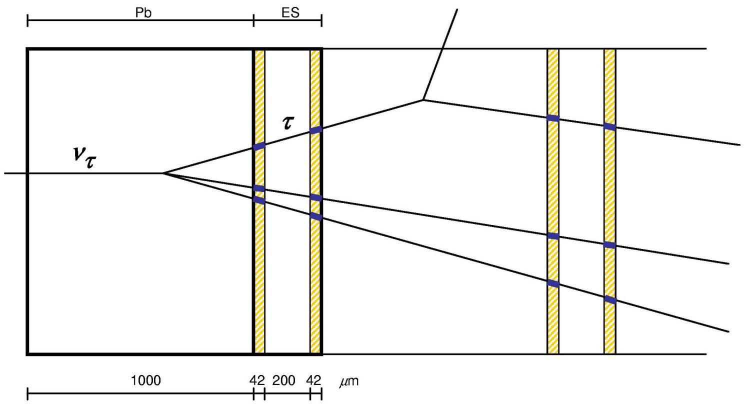

Figure 2.13: Schematic structure of an ECC cell in the OPERA experiment. The τ decay kink is reconstructed in space by using four track segments in the emulsion films.

The τ can also decay in one of the films downstream of the vertex plate (e.g. in its plastic base). Even then, the kink angle can be reconstructed, albeit with a lower angular resolution, from the track segments in the emulsion layers on either side of the base. A fraction of the short decays is detectable by measuring a significant impact parameter (IP) of the daughter track with respect to the tracks originating from the primary vertex.

The detection of the τ decay into an electron benefits from the dense brick structure given by the compact cell design, which allows electron identifica-

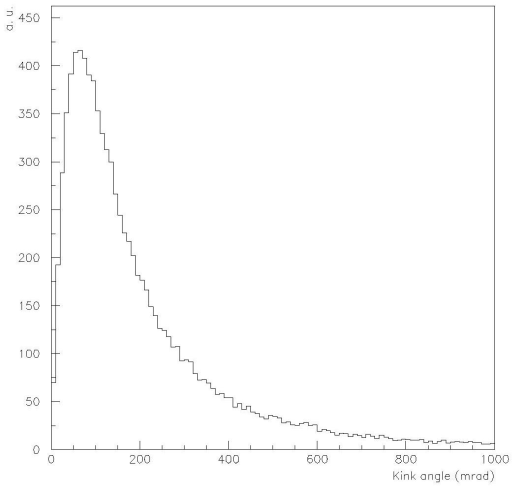

Figure 2.14: τ kink angle distribution for the $\tau \to e$ decay mode.

tion through its showering in the downstream cells (Fig. 2.15). The main background source for this channel is due to *charmed* particles production in ν_μCC interactions (Fig. 2.16)

For the muonic decay mode the presence of the penetrating (often isolated) muon track allows an easier event vertex finding. The potential background from large angle scattering of muons produced in ν_μ CC interactions can be reduced to a tolerable level by applying cuts on the kink angle and on the transverse muon momentum at the decay vertex. Another background is due to muon produced by charmed particle decays (Fig. 2.16).

Hadronic decay modes have the largest branching ratio but are affected by background due to hadron reinteractions. One of the primary hadrons, in fact, can interact in the first lead plates and, if the main lepton of this interaction are not detected in the emulsion, it may simulate the charged single-prong decay of the τ (Fig. 2.16). Kinematical cuts can be used to reduce this background. An important tool for background rejection is the determination of the transverse momentum of the daughter particle with respect to the direction of the τ track candidate. For electronic τ decays the ECC technique is well suited to identify electrons and to determine their energy by measuring the density of track segments associated to their showering

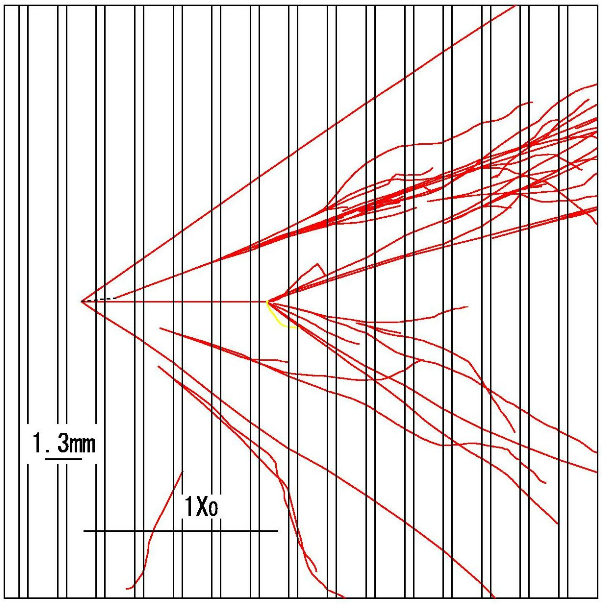

Figure 2.15: Simulated ν_τ event with τ decaying into an electron.

in the brick. For charged hadrons and muons, the momentum is deduced from the measurement of the multiple scattering in the lead plates. As discussed in the following, the muon momentum is also measured by the electronic detectors in a large fraction of the cases.

2.4 Efficiencies, background and sensitivity of the experiment

The signal detection efficiency of OPERA was estimated on the basis of tests and simulations. The latter have been tuned with data obtained in previous emulsion experiments such as CHORUS and DONUT.

All single-prong τ decay modes are used to search for the so-called long τ decays. These are events in which the τ track is long enough to exit the lead plate where the primary vertex occurs. Short decays (in which the τ track is contained within the vertex plate) are considered for the $\tau \rightarrow e$ channel.

Long decay candidates are selected by detecting a kink topology and

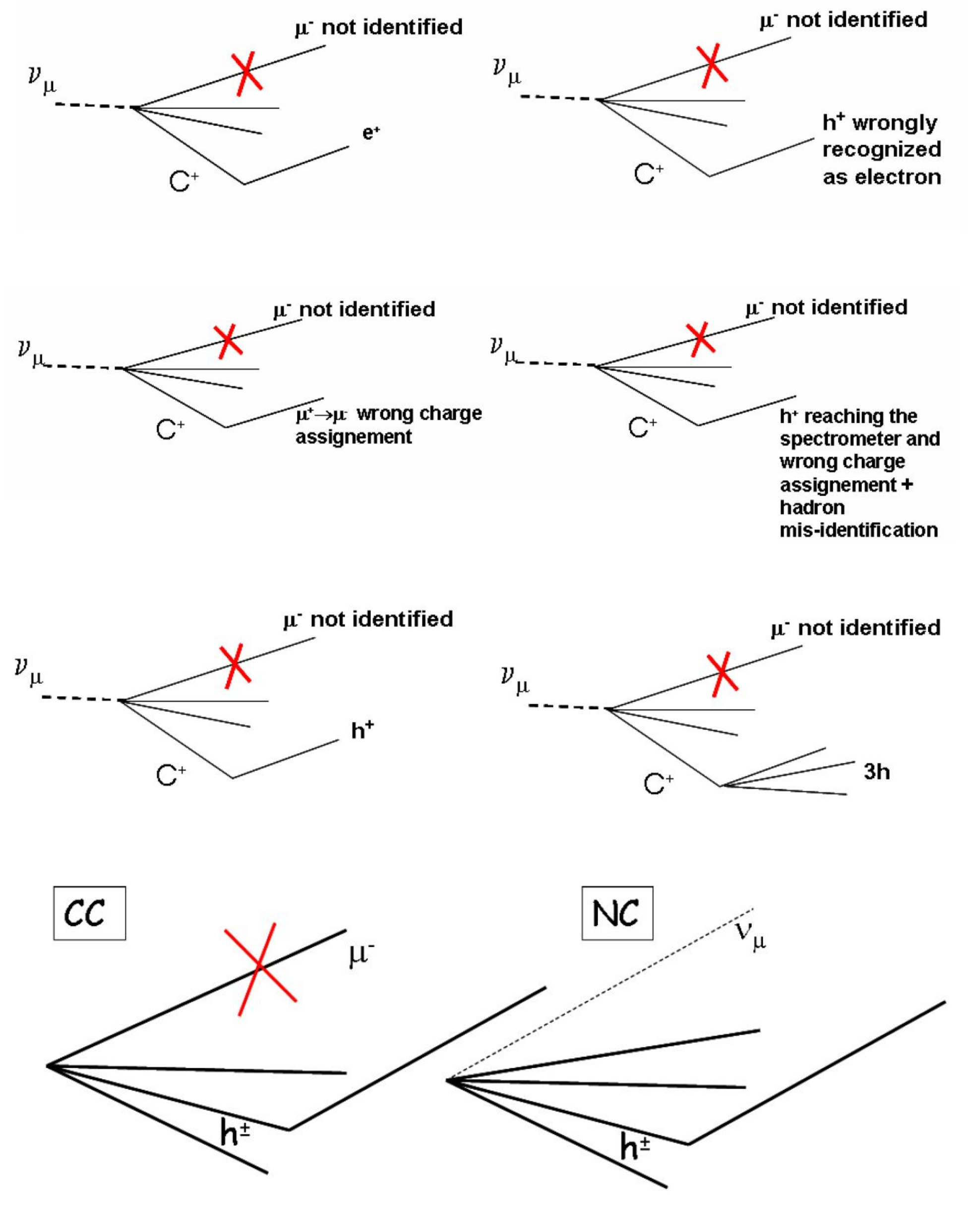

Figure 2.16: (From top to bottom) First three figures are examples of *charmed* particles decays: backgroud for tau decay in electronic, muonic, hadronic channels. The last one is an example of hadronic reinteractions in lead, which is a background for tau decay into hadrons.

short decays by exploiting an impact parameter method. Kinematical cuts are applied to both samples in order to enhance the signal to background ratio.

The $\tau \to e$ decay mode is identified by the distinctive energy loss of the daughter electron in the lead/emulsion brick structure. The main background to this channel is given by charm production in ν_μ CC interactions undergoing electron decay and with the primary muon escaping detection.

Muonic τ decays are characterised by an identified muon originating from the τ track kink. For these events the main background is due to large angle muon scattering in the lead plates.

Hadronic decay candidates are defined as those events in which the kink daughter particle is not identified either as an electron or a muon. In this case, charm production with subsequent hadronic decay and hadronic reinteractions in lead give a similar contribution to the background.

Table 2.3 summarises the expected numbers of background and τ events for different values of Δm^2 and full mixing, under the assumption of five years of running in the CNGS beam, operated in shared mode; a summary of the τ detection efficiency in the three decay channels is given in Tab. 2.4

Assuming $\Delta m^2 = 2.5 \times 10^{-3}$ eV^2 and full mixing, the probability to observe the number of events required to obtain a 4σ significance, is $\sim$97%.

Decay mode	Signal (2.5x10^{-}3eV^{2})	Signal (3.0x10^{-}3eV^{2})	BG
$\tau \to$e^{-}	3.5	5.0	0.17
$\tau \to \mu^{-}$	2.9	4.2	0.17
$\tau \to$h	3.1	4.4	0.24
$\tau \to$3h	0.9	1.3	0.17
Total	10.4	15.0	0.76

Table 2.3: Expected numbers of τ and background events in OPERA after five years of data takingper kton. τ events are reported for two values of Δm^{2} assuming maximal mixing.

Decay mode	Efficiency
$\tau \to$e^{-}	3.4%
$\tau \to \mu^{-}$	2.8%
$\tau \to$h	2.9%
Total	9.1%

Table 2.4: τ detection efficiencies for the differente decay modes.

Chapter 3

Nuclear Emulsions

Nuclear emulsion detectors provide three-dimensional spatial information on particle tracks, with excellent space resolution (of the order of $\sim \mu$m), as well as high angular resolution (of the order of $\sim$mrad): they are, therefore, ideal for the unambiguous detection of short-lived particles as OPERA needs.

3.1 Basic properties of emulsions

Nuclear emulsions are made of micro-crystals of silver halides (usually AgBr) suspended in a gelatin composed of organic materials (Fig. 3.1). The passage of charged particles inside a nuclear emulsion can become visible through a chemical amplification of the perturbation occurring at atomic scale induced by energy losses of ionizing particles.

Nuclear emulsions are basically the same as general purpose photographic emulsions even if they have several distinguishing features from the second one:

- the silver halide crystals are very uniform in size and sensitivity (that leads to the capability to detect tracks with good efficiency);

- the silver to gelatin ratio is much higher than in a conventional emulsions and the thickness is larger.

Richard Lee Maddox invented in 1871 the first *dry* photographic medium, the gelatin-suspension of light-sensitive silver halide crystals: this rapidly replaced the *wet* colloidon (nitro-cellulose) process of photography. The crucial difference between gelatin and colloidon is that gelatin is permeable to water so after preparation it can be dried for the exposure process and, after, it can be re-wetted to allow the developing solution to access the interior atoms of the emulsion. The drawback is that possible gemetrical distortions can affect the emulsions.

The linear dimension of the crystals range from 0.1 μm to 1 μm. The size of the microcrystals for OPERA emulsions is ~ 0.2 μm and is well controlled by the current industrial technologies developed for photographic films (Fig. 3.2).

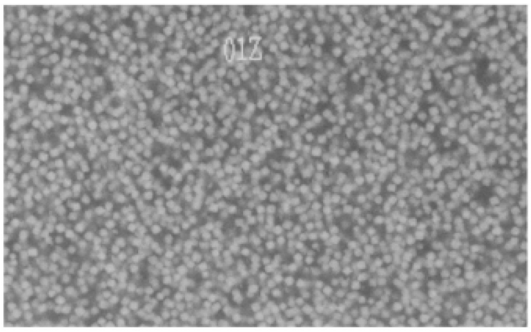

Figure 3.1: Micro-photograph of the crystals distributed in an emulsion layer of the OPERA experiment. Micro crystals can be recognised as white grains.

3.2 The photographic processes

A characteristic of silver halides is that, when particles release energy to the cristal by ionization, this energy produces a *latent image* which is almost stable during time.

A developing agent reduces the AgBr to metallic Ag more rapidly than in the crystals not irradiated and, when an emulsion is developed, all the crystals containing a latent image center are reduced to metallic silver. The

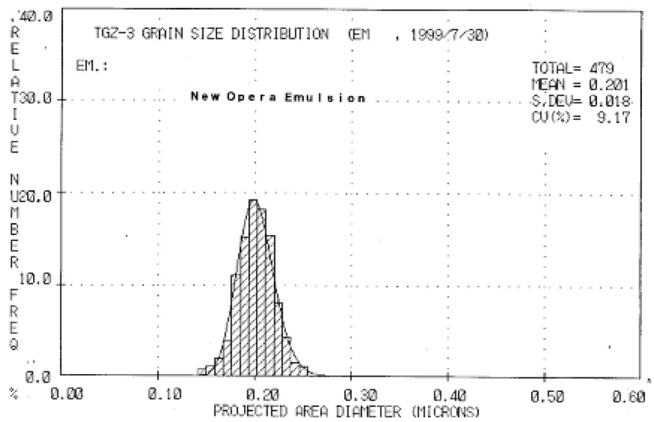

Figure 3.2: Crystal diameter distribution of the Fuji emulsions which were produced for the OPERA experiment.

other crystals are removed by fixing, and the result is a series of dark silver grains of about of 0.6 μm size, which can be observed by microscopes. The paths of an ionizing particle is visible as a sequence of these grains.

3.2.1 Formation of the latent image

When light or an ionising radiation hits a silver halide crystal, it has the effect of liberating mobile electrons and a positive hole $(AgBr)^+$. This can move through the crystal lattice, because of capture and release of electrons from adjacent bromine ions, while the electrons are trapped by impurities (for example S used for sensibilization).

It is important for latent image formation that a significant proportion of electrons and positive holes are trapped separately, otherwise they could recombine and regenerate halide. The silver halide crystal contains free (interstitial) silver ions, which can move through the lattice. When an interstitial silver ion encounters a trapped electron, the charges are neutralised and an atom of metallic silver is formed. In this way a stable aggregate of four or more atoms of silver can be built up. The site is then known as a latent image center, and the entire crystal may be reduced to metallic silver by development.

The formation and preservation of the latent image depends on external conditions such as temperature, humidity, pressure. As temperature and humidity increase, the sensitivity decreases and the latent image is less stable: this effect is called *fading*. The fading can be artificially induced in order to erase the image of unwanted tracks accumulated before the exposition (Relative Humidity $90 \div 98\%$, T $\sim 40°$C, 3 days) (Refresh). The sensitivity of refreshed emulsion films shows no degradation.

3.2.2 Development

Photographic development is the process by which the latent image contained in an emulsion is made visible through the reduction of silver ions in the silver halide crystal to metallic silver.

For developing nuclear emulsions, a developer is chosen which reduces completely those crystals containing a latent image center, while leaving unchanged those not containing a center. The development time used for processing should be sufficient for those crystals with a latent image center to be reduced completely, but not so long to develop also the unexposed ones. Some crystals will be however developed even if they do not contain a latent image center. These grains, when developed, constitute what is known as *fog*.

In chemical development, silver ions are provided from the silver halide crystal containing the latent image center. The action of a chemical developer produces a mass of filaments bearing little resemblance to the original crystal.

Chemical development, like many other chemical reactions, is dependent on temperature. In general, development occurs more rapidly at higher temperatures - below 10°C development virtually stops. For this reason it is important to keep the processing temperature constant during development, otherwise it will not be possible to assess the correct development time.

3.2.3 Fixation

The purpose of fixation is to remove all the residual silver halides, leaving the metallic silver to form the image; if the silver halides were left in the emulsion, they would slowly go brown and degrade the image.

It is important to use a fixer which has not been exhausted when processing nuclear emulsions, otherwise some silver halide will remain in the emulsion.

After fixation, the emulsion must be washed very thoroughly, to remove all development residuals.

3.3 Processed emulsion

3.3.1 The *fog*

Random developed grains constituting *fog* are found in emulsion because there are always a few grains of the large number that develop as quickly as the track grains.

The number of fog grains increases linearly with the time of development, until about twice the period required for a track; if this time is extended still more, the density of fog starts to rise more rapidly. Fog produced by visible light is limited to the surface because only a thin layer of the emulsion is penetrated by the light.

Another type of fog consists of a very large number of grains so tiny to be visible with the highest resolution: it is generally attributed to colloidal silver and has been observed to increase as the sulfite content of the developer is increased.

3.3.2 Track visibility

Fog is an especially serious problem when one is making a study for which it is essential to see minimum ionizing tracks. In order to see the minimum ionizing particle in an emulsion, it needs almost 30 developed grains every 100 μm of path (Grain Density) and the accidentally developed grains concentration should be < 5 in 1000 μm^3 (Fog Density).

If the depth of field of the objective is lowered by using a larger numerical aperture, the thickness of the emulsion which is seen in the focal plane is reduced, and correspondingly a higher ratio of fog density can be tolerated because a smaller proportion of the fog grains will be in focus. The track visibility is reduced if it is inclined.

3.3.3 Shrinkage factor

After processing, an emulsion will occupy less volume than before unless some material is added to replace the silver halide dissolved by the fixer. If the emulsion plate is mounted on a glass or plastic base, the most conspicuous evidence of this effect is a reduction of the thickness of the emulsion layer.

For any quantitative measurements of tracks density, ranges, and angles in the emulsion, it is important to measure the precise original thickness.

The *shrinkage factor* is the ratio of the thickness of emulsion at the time of exposure divided by its thickness at the time of scanning.

Both gelatin and glycerin are hygroscopic so that the actual equilibrium thickness (and also the index of refraction) depends on the ambient humidity. Normal processed emulsion changes its thickness with the ambient humidity in a way that is given roughly, when the humidity is near 60%, by:

$$\frac{\Delta t}{t} = \frac{RH^2}{3 \cdot 10^4}$$

where t is the nominal thickness, Δt is the increase from the dry thickness and RH[1] is the relative humidity in percent.

[1]The relative humidity of an air-water mixture is defined as the ratio of the partial pressure of water vapor in the mixture to the satured vapore pressure at a prescribed temperature. It is normally expressed as a percentage and is defined as:
$RH = \frac{p(H_2O)}{p^*(H_2O)} \cdot 100\%$ where $p^*_{(H_2O)}(T) = \alpha e^{\frac{\beta T}{\lambda + T}}$ (T expressed in Celsius)

3.3.4 Distortions

Ideally, the processing of an emulsion should lead to a uniform contraction in thickness – in the z-direction – leaving unchanged the x,y coordinates of any points. In practice, distortions which limit the precision of measurements on tracks occur. Distortions can vary from one region of the emulsion sheet to another, but in well-processing conditions they do not change rapidly in passing over distances of the order of a centimeter.

The simplest form of general distortion is a uniform shear: straight tracks remain rectilinear but their direction and length change by an amount which depends on the magnitude and direction of the shear.

A more serious source of error is due to differential shear of the emulsion in which both the magnitude and direction of the shear change with depth. Such distortion changes the tracks of an energetic particle from a line into a curve.

In the case of emulsions mounted on a glass or plastic base, the points on tracks are assumed to be unaltered by the processing [30]. The lateral displacement in the x and y can be expressed by the distortion vector $\mathbf{k}$ (the distortions are mainly of the quadratic type):

$$\mathbf{k} = \mathbf{k_1}\frac{z}{s} + \mathbf{k_2}(\frac{z}{s})^2 + ...$$

where s is the thickness of the unprocessed emulsion and z is the distance from the displaced point to the base in the unprocessed plate, $\mathbf{k_1}$ and $\mathbf{k_2}$ are in general vectors having different directions (Fig. 3.3). Since in the free

surface of the emulsion (the surface between emulsion and air, where $z = s$) the direction of a track usually remains unchanged

$$\left.\frac{d\mathbf{k}}{dz}\right|_{z=s} = \frac{\mathbf{k_1}}{s} + \frac{2\mathbf{k_2}}{s} = 0$$

it is possible to find a relation between $\mathbf{k_1}$ and $\mathbf{k_2}$:

$$\mathbf{k_1} = -2\mathbf{k_2}$$

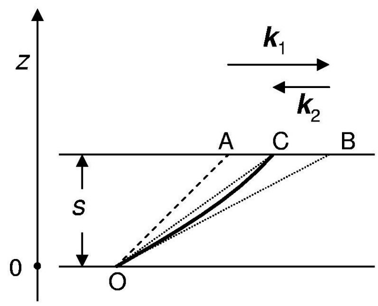

Figure 3.3: Distortion scheme in an emulsion layer; OA is the track in absence of distortions, OB is the track with only linear distortions, OC is the track with total distortions;

The horizontal projection of the track, as observed by an optical microscope, is shown in Fig. 3.3.

This kind of distortion changes an originally straight track into a parabolic form and is referred to *C-shaped* distortion. Less frequently and more especially near the processed edge of the emulsion, the tracks may be bent into an *S-shape*. A third type of distortion is known as *chopping* and results in violent changes in direction of the track, and lateral and longitudinal displacements of many microns

3.4 OPERA Emulsion films

The handmade procedures used in the past experiments done with nuclear emulsion applied to OPERA would be prohibitively time consuming. To overcome this problem, a R&D project has been done by Nagoya University in collaboration with the Fuji Film company to establish a process of automatic coating of nuclear emulsion films. After several tests, it was confirmed that the OPERA emulsion films can be produced by commercial photographic film production lines. Fig. 3.4 shows the cross sectional view of the developed machine-coated emulsion film.

As opposed to hand-made films, the thickness can be precisely controlled as in the case of commercial color films. The measure of the film emulsion

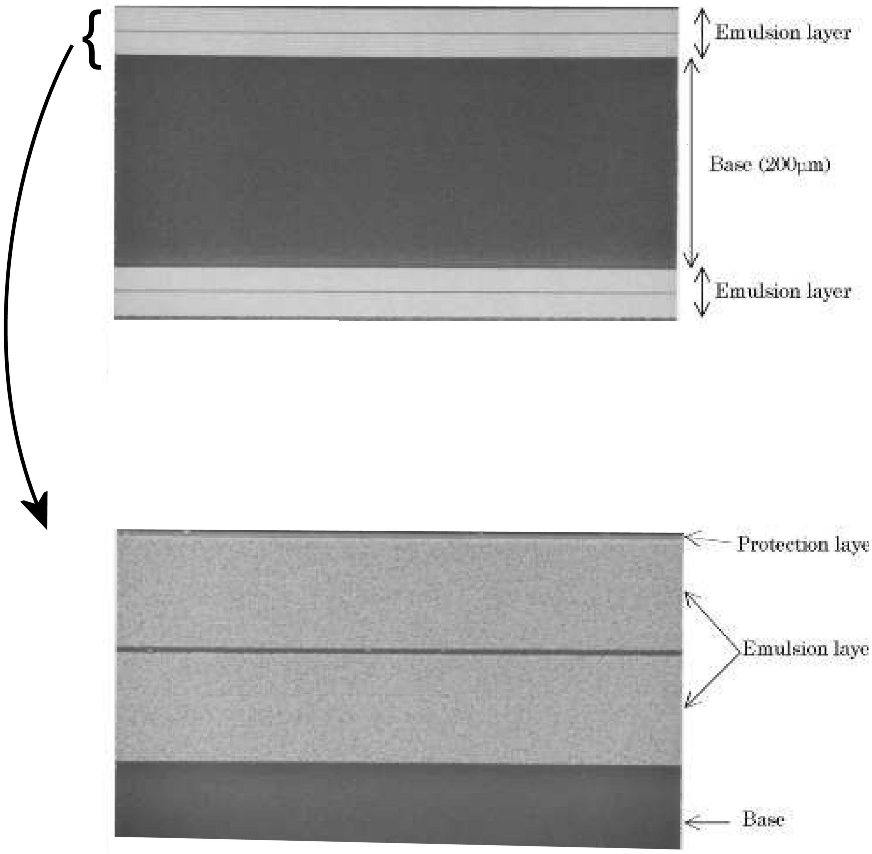

Figure 3.4: Top: photograph of the cross section of a machine-coated emulsion film. The picture was taken with an electron microscope. Diluted emulsion layers of 44 μm thickness are coated on both sides by a 200 μm thick triacetate base. Bottom: enlarged view of the top emulsion layer. A thin (≈ 1 μm) protective film (gelatin) is placed over the emulsion layer at the same time of coating.

layer thickness after development shows a distribution with $\sigma \sim 1.3\ \mu$m.

As shown in Fig. 3.4, each film has a protective gelatin layer of 1 μm thickness. This prevents the occurrence of black or gray patterns on the emulsion surface. These patterns are due to silver chemically deposited during the development. The removal of these stains was the most time-consuming task in the emulsion preprocessing. By means of the protective coating, surface cleaning is not needed anymore and the preprocessing procedure becomes compatible with the daily handling of thousands of emulsion films, as in the case of OPERA.

In addition, the presence of this protective layer allows direct contact with the lead plates. Without this protection, one would have to insert thin insulator sheets in order to avoid chemical reactions between the lead plates and the silver halides contained in the emulsion.

For automatic coating some dilution of the gel is required. Under normal conditions, the grain density, defined as the number of grains per 100 μm along the particle trajectory, decreases almost linearly with the dilution factor although part of the sensitivity loss may be regained in the development phase. This problem has been solved by increasing the sensitivity of each crystal using the technology of crystal growth developed for standard photographic films.

As shown in Fig. 3.2, the crystal diameter distribution in the emulsion layer is rather uniform around 0.20 μm. The currently achieved grain density of the machine-coated emulsion films is 30 grains/100 μm even in the case of a factor of two dilution.

The so-called emulsion fog is due to accidental grains randomly distributed in the emulsion volume (Fig. 3.5). They constitute a background which should be kept at the level of ≤ 5 fog /1000 $\mu\mathrm{m}^3$.

The intrinsic position resolution of the emulsion films can also be investigated by measuring for a MIP track the position residuals of the centre of each grain with respect to a fitted straight line. The result is shown in Fig. 3.6. The measured resolution of $\sigma \sim 0.06\ \mu$m can be compared with the expected value of 0.058 μm $\sim 0.2\ \mu\mathrm{m}/\sqrt{12}$, where 0.2 μm is the diameter of the original crystal. This result implies that the crystal uniformly grows

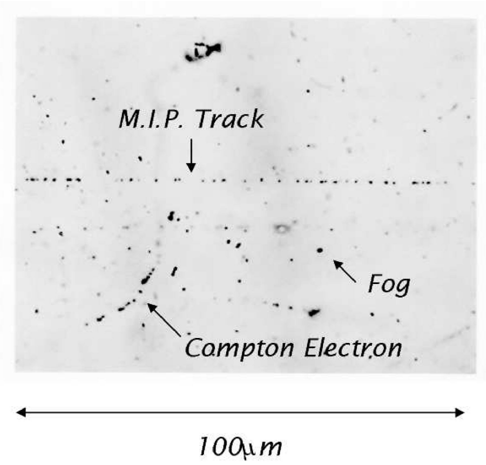

Figure 3.5: Photograph of a minimum ionising particle (mip) recorded in an emulsion layer. The grain density is defined as the number of grains per 100 μm track; the fog density is defined as the number of fog grains per 1000 μm^3,

under development up to a grain with diameter of ~ 0.6 μm.

The physics properties of the emulsion layer are the following: density $\rho = 2.71$ g/cm^3, average atomic number $\langle A \rangle = 18.2$, average atomic charge $\langle Z \rangle = 8.9$, radiation length $X_0 = 5.5$ cm, $(\frac{dE}{dx})_{mip} = 1.55$ MeV/g/cm^2 or 37 keV/100 μm, nuclear collision length $\lambda_T = 33$ cm and nuclear interaction length $\lambda_I = 51$ cm.

The base material of the films is cellulose triacetate (TAC), which is one of the commonly used base materials for photographic films. Its physics properties are: density $\rho = 1.28$ g/cm^3, optical index n = 1.48, radiation length $X_0 = 31$ cm, nuclear collision length $\lambda_T = 47$ cm and nuclear interaction length $\lambda_I = 67$ cm.

Emulsion film distortions have also been investigated. As said before, distortion is a phenomenon which shifts the position of the recorded trajectories in the emulsion layer because of stresses accumulated in the gelatin layer. In hand-made emulsion plates, shifts of several μm are frequently observed, caused by a disuniform drying at the plate production.

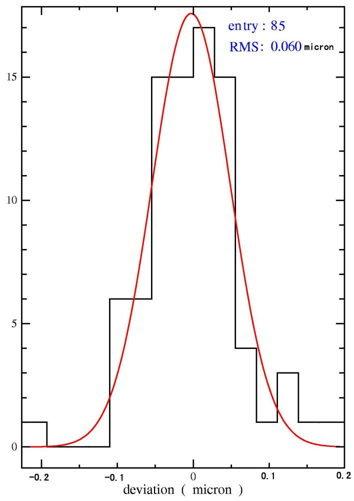

Figure 3.6: Position residuals of the grain center with respect to a fitting straight line.

Distortions can affect the efficiency in connecting two micro-tracks[2] in the two emulsion layers of a film, however the base tracks constructed with connected micro tracks have positions and angles not affected by distortion.

Fig. 3.7 shows the typical distortion pattern in the central part of an emulsion film. The distortion effect is very suppressed in industrial films down to $\sim 0.4\ \mu$m. This result is due to the more uniform drying process at the production and also to the careful development treatment specially devised for OPERA.

Usually the distortion becomes larger near the edge of the film.

The *fading* and *aging* features of the industrial emulsion films have been investigated. Fading is the loss of the latent image occurring prior to development. Aging is the degradation of the emulsion sensitivity during the exposure.

Fading is not a severe problem for this experiment, since brick will be extracted and developed within one week after the event occurred. Within about one month, possible extra bricks required for further analysis (candidate events) are extracted and developed. Moreover, one can take advantage

[2]micro-track is a track reconstructed in one of the two gelatine layer

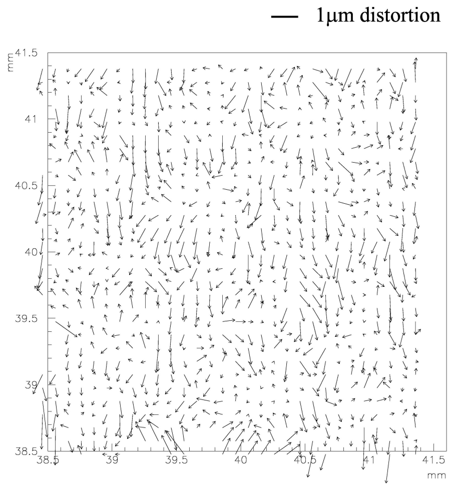

Figure 3.7: Measurement of the emulsion distortion at the centre of an emulsion film (from the OPERA proposal). The scanning area is ≈ 3 mm x 3 mm. The vectors indicate the distortion direction. The absolute value of the distortion is indicated by the length of the arrow.

of the existence of some fading, which contributes to erase unwanted cosmic ray tracks accumulated during film production and transportation before the run. In principle, the fading time constant depends on the environmental temperature, humidity and on the oxygen density. One example of these properties is shown in Fig. 3.8.

In order to check the features of the Fuji emulsion in maintaining their sensitivity with age, tests on sensitivity has been performed by exposing all plates of emulsions to an electron beam and by developing them soon after. The results are that even the oldest plates still show enough sensitivity, i.e. ≥ 25 grains/100 μm.

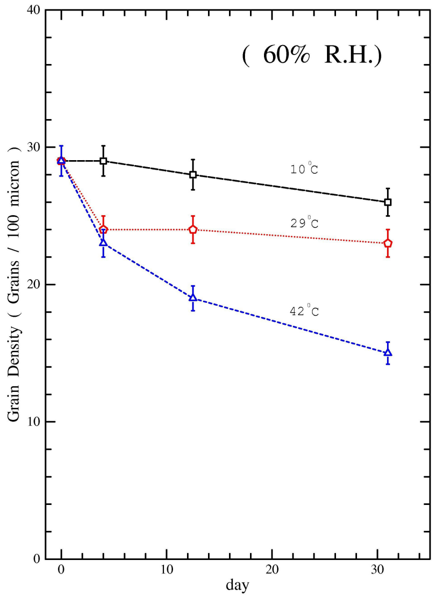

Figure 3.8: Example of fading. Each film is packed at 60% R.H. and 20°C. After a beam exposure, the samples have been stored at different temperatures. At 10°C the time to reduce the grain density from 29 to 25 grains/100 μm is estimated to be 1.5 to 2 months.

Chapter 4

The automatic system for emulsion scanning

4.1 Introduction

Nuclear emulsions have been used for more than 60 years in nuclear and particle physics and are connected to many major discoveries, as for example the pion decay in 1947, etc, ...

The amount of emulsions used in the early experiments was relatively small and the measurements were made manually with microscopes by moving the stage, adjusting the focal plane of the objective, and examining a magnified image of tracks in nuclear emulsions by eyes. Later, the stage was motorized and the image made available also on a TV screen.

Because of the limit in human resources for scanning and the intrinsic slowness of the data readout the use of nuclear emulsions has gradually decreased after the development of electronic detectors.

However the increased sensitivity, the packaging method, the industrial production, the scanning and measuring instrumentation have given the possibility to plan and realize large detectors also based on emulsions.

Automatic scanning systems allow for fast extraction of physical information from emulsion after they have been exposed to particle radiation.

The pioneering work in automatic scanning was done at the the University of Nagoya (Japan) and a first complete application of the automatic system was used in the CHORUS experiment data analysis in the late '90s [32]. The so-called Track Selector was designed to detect tracks with a predicted angle in the field of view of a CCD camera.[1] An improved version is now used in Nagoya. The track recognization algorithm, based on tomographic images taken at different depth, is completely implemented on hardware: tracks are extracted by shifting horizontally the images to find coincidences.

European groups followed a different approach, initiated by the Salerno. It is based on multi-track reconstruction regardless of their slope and on the use of commercial products.

4.2 The principle of automatic scanning of emulsions

An automatic scanning system for nuclear emulsions consists of a computer driven mechanical stage, an optical system, a photodetector (typically a CCD sensor or CMOS camera) and its associated readout as shown in Fig. 4.1[27].

The aquisition is done by moving the focal plane of the objective inside the emulsion at constant speed, view by view, and grabbing a sequence of images. The horizontal and vertical movements and the intensity of the light is controlled by a computer (Fig. 4.2).

The vertical speed of the optical axis v is determined by the the frame rate of the camera (fps), the emulsion thickness S and the number of layer to be grabbed n:

[1]The system used a grabber board connected to a CCD Camera (512 x 512 pixel at 120 Hz frame rate) and a Fast Programmable Gate Array (FPGA) for image processing and tracking. The area of the view was $\sim 150 \times 150\ \mu\mathrm{m}^2$.

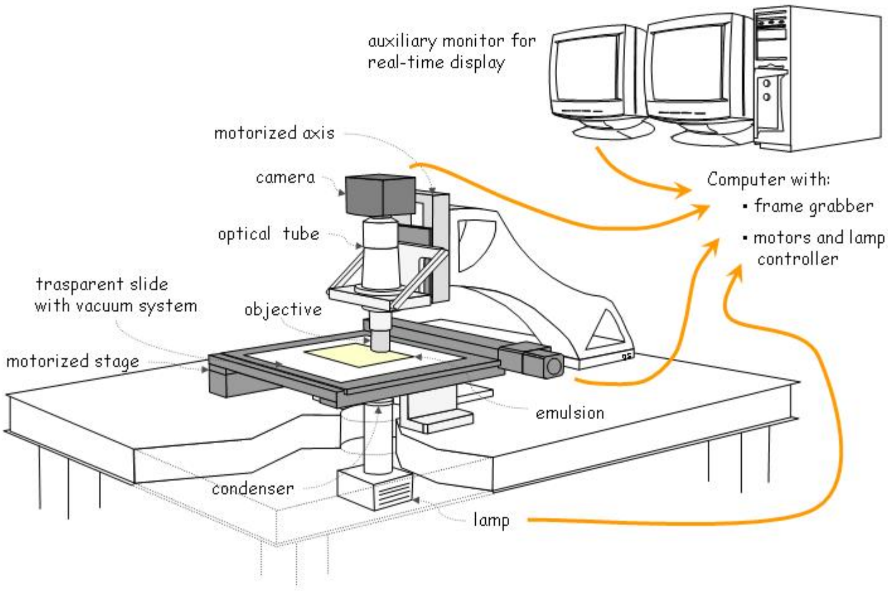

Figure 4.1: Layout of the components of a typical automatic scanning system for nuclear emulsion.

$$v = \frac{S \cdot fps}{n} \qquad (4.1)$$

The number of layers must be sufficient to allow a good recognition of tracks; the distance between consecutive layers Δz is a critical parameter because it should be small enough not to lose grains but larger than the depth of view of the objective in order to not acquire the same grain in too many layers.

Since the grain density of a minimum ionizing particle is about 30 grains per 100 μm in an unprocessed emulsion and the depth of view $\approx 0.5 \div 2$ μm, the number of layers must be chosen to have a layer distance of:

$$\Delta z = S/n \approx 2 \div 3 \ \mu m \qquad (4.2)$$

Grains belonging to different layers are then searched for to see if they form a straight line as shown in Fig.4.3.

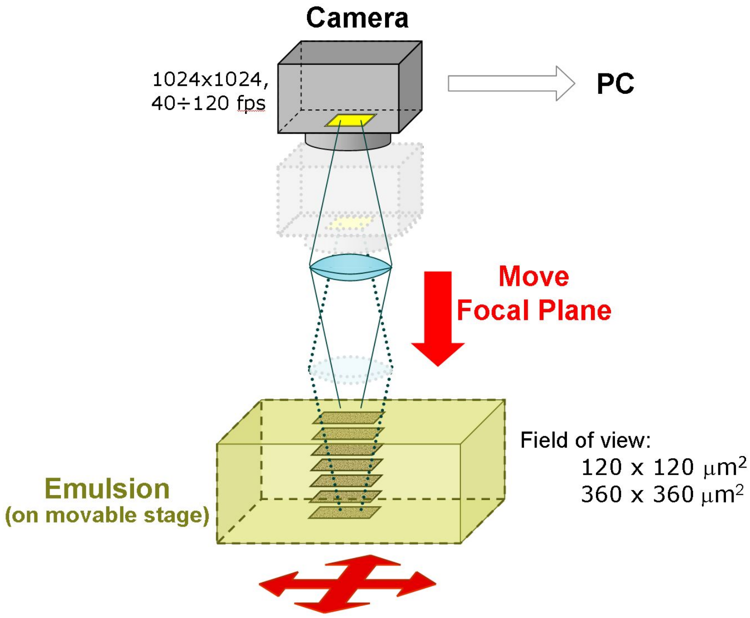

Figure 4.2: The readout: for each field of view several tomographic images of the emulsion are taken by moving the optical axis and hence the focal plane inside the emulsion.

The scanning system should take care of a high acquisition speed and high angular and position accuracies. The requests are:

- mechanical high performances with position accuracy better than one micron and small mechanical settling-time;

- wide field of view with resolution below the micron and working distance tuned to see both emulsion sides;

- mega-pixel resolution camera with high frame rate;

- powerful image processors.

In Fig.4.4 is shown one of the automatic systems installed in Bologna.

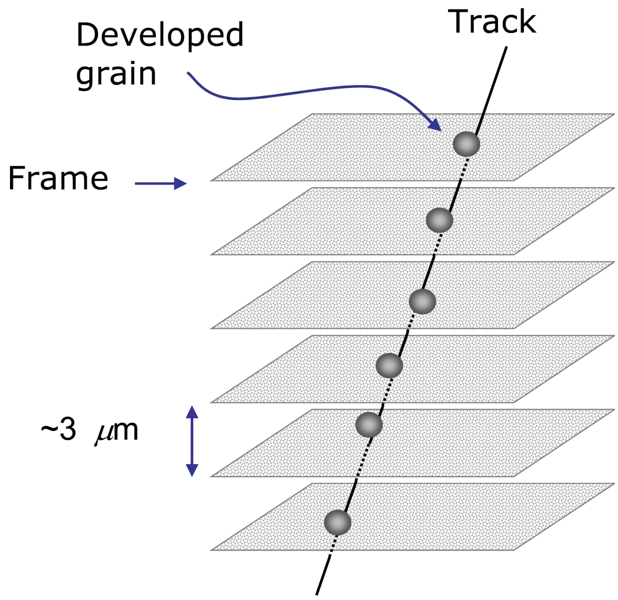

Figure 4.3: The track is found by connected grains in each layer.

4.3 Mechanics

Since the precision of optical measurements depends on position stability, the microscope is mounted on a high quality table which provides a virtually rigid and vibration-free working surface that holds the components in a fixed relative position; the legs supporting the tabletop include an air suspension mechanisms to reduce vibrations.

A *scan table* with 20.5x20.5 cm^2 range on horizontal directions is mounted on the tabletop. The horizontal coordinates are read out by two linear encoders with an accuracy of 0.1 μm. The movement of the scan table is delimited by two optical limit switches which prevent the stage to damage the objective.

The vertical linear stage is mounted on a granite arm as shown in Fig. 4.4. The vertical position is read out by an integrated linear encoder with an accuracy of 0.01 μm. The limit switches are integrated in the stage, but the lower one has been modified and substituted with an optical switch based on a photodiode to have a better precision and to avoid that the objective scratches the emulsion.

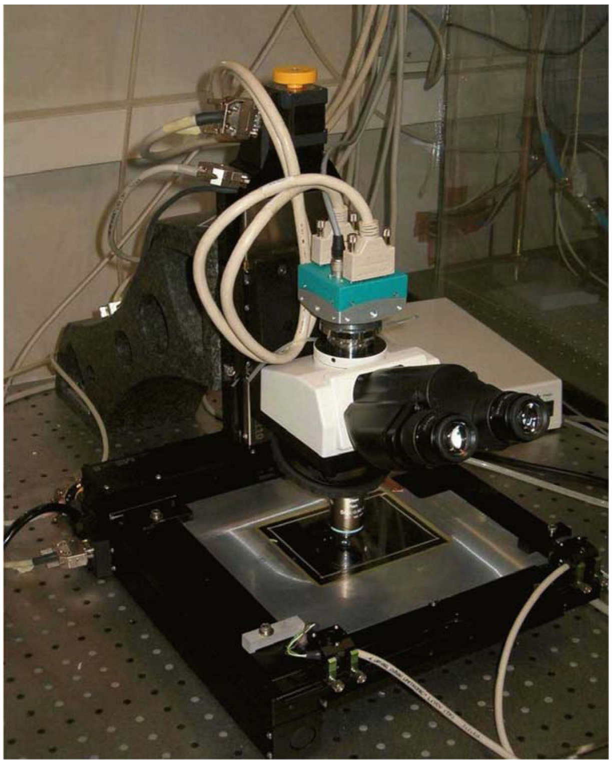

Figure 4.4: One of the microscopes installed in Bologna.

A stage glass with a vacuum pump designed and realized by Silo factory in collaboration with INFN helps on keeping the emulsion sheet flat during acquisition.

Both vertical stage and scan table are equipped with the steppers motors model NanoStep RFK Series 5-Phase Microstepping Systems produced by Vexta. Stepper motors are excellent for precise positioning control.

The stage controller is a FlexMotion board provided by National Instruments and is inserted into the host PC.

4.4 The optical system

The optic is composed by the objective, trinocular and the mounting tube from the Nikon manufacturer. Several tomographic images of the emulsion layers must to be taken by the automatic system: hence, the *Working Distance* (WD) of the objective should be at least 300 μm to see the back side of the emulsion.[2]

The thickness of the emulsion sheet between the focal plane and the front lens of the objective is variable and depends on the depth at which we take the image: from 0 at the top surface of the emulsion to $\sim$300 μm at the bottom surface.[3]

Moreover the *Numerical Aperture* (NA) of the objective should be as large as than possible (as is explained below) and, since the spherical aberration increases as the cube of the NA, the variation of the intermediate medium (between objective and focal plane) which can be tolerated, is only ± 20 μm. For this reasons, in order to use *dry* objectives, it is mandatory to compensate in some way the *cover glass* thickness variations (some objectives used in biological analyses have a collar that permits this kind of correction by moving a group of lenses inside the tube).

Typical immersion oils have a refractive index of 1.51, so light rays passing through the emulsion sheet encounter an optically homogeneous medium because the refractive index of emulsion and plastic base are respectively: $n_{\text{emulsion}} = 1.51 \div 1.52$ and $n_{\text{base}} = 1.48$.

Another important feature to be considered is the longitudinal resolution or *Depth of Field* (DOF), which is the axial range through which an objective can be focused without any appreciable change in the image sharpness.

Inside the emulsion, in order to measure with high accuracy the distance z between grains and the surface and the horizontal coordinates x and y, the DOF should be as low as possible. This value at high numerical aperture is

[2]The Working Distance (WD) is the distance between the objective front lens and the best focal plane.

[3]A *dry* objective is designed to minimize the aberrations considering a fixed thickness of air between the front lens and the best focal plane and, mostly, the standard thickness of the cover glass (0.17 μm with refractive index of 1.515)). When using high magnification dry objectives, cover glass thickness variations of a few micrometers result in dramatic image degradation due to wrongly corrected spherical aberrations.

determined primarily by wave optics[4] and is given by the formula:

$$\mathrm{DOF} = \frac{n\lambda}{\mathrm{NA}^2} \tag{4.3}$$

where λ is the wavelength of illumination, n is the refractive index of the imaging medium, NA is the objective numerical aperture.[5]

Notice that the Depth of Field shrinks inversely with the square of the numerical aperture, so to reduce the DOF, objective with high NA should be used.

The last crucial point is the *Resolution* (R), that is defined as the smallest distance between two points that can still be distinguished as two separate entities and is given by: [6]

$$R = 0.61\lambda/\mathrm{NA} \tag{4.4}$$

The objective magnification depends on the camera sensor used to acquire the tomographic pictures (some pixel per micron are needed): with the chosen camera it is mandatory to have a magnification M>40.

4.5 The CCD Camera

The digital camera that is used is the model MC1310 produced by Mikrotron[7]: it has a megapixel CMOS sensor of 1280 x 1024 pixels, whose surface is 12x12

[4] It derives from a *Rayleigh criterion*: the minimum resolved distance is when the optical path distance between the two waves (focused and not-focused) is equal to $\lambda/4$.

[5] NA is the angle between the microscope optical axis and the direction of the most oblique light rays captured by the objective(angular aperture) multiplied by the refractive index of the intermediate medium: $\mathrm{NA} = n \sin\alpha$.

[6] The resolution can be expressed by another *Rayleigh criterion*: it is the radius of the circle of least confusion which is the image generated by the objective from a point-like source. When all the aberrations of the systems are corrected, it is the central disk (Airy disk) of the diffraction pattern of the point.

[7] Mikrotron GmbH Landshuter Str.20-22 D-85716 Unterschleissheim, Germany

μm^2 for each pixel. Analog to digital conversion takes place inside the camera and the communication interface is a *Full Camera Link* [8]. This camera can grab images at 500 frames per second (fps) at the maximum resolution; this implies a data flux of ∼600 MB/s. The automatic system requires the frame rate to be set at 376 fps.

The images are grabbed in 256 grey levels mode (0 = black, 255 = white): the light that hits a pixel is digitized into an 8 bit signal and sent to the frame grabber.

Both the frame grabber and the image processor are integrate inside the board (a Matrox Odyssey) wich is equiped with a processor Motorola G4 Power PC and 1 GB of DDR SDRAM: the communication bus can support up to 4 GB per second.

In Fig.(4.5) is shown a tipical emulsion picture as it appear on the monitor.

Figure 4.5: Tipical emulsion picture grabbed by the CMOS camera. The field of view has the dimension of ∼390 x 310 μm^2 (1280 x 1024 pixels).

[8]Camera Link is a specific communication protocol for high speed digital cameras

4.6 The illumination system

The illumination system has been designed and developed in collaboration with Nikon Italia in order to obtain the so called *Koeler system* and is located under the scanning table.

In the koeler illumination system an image of the light source is focused with a lense (the *collector*) on the condeser diafram to produce a parallel light beam through the plane where the specimen is located. The condenser concentrates the light into a cone shape which illuminate uniformly the field of view: the NA of the condenser should be equal to that of the objective. A field diafram controlls the amount of light that enters into the condenser.

4.7 The online acquisition software

The online acquisition software, called SySal, was developed by the Salerno group for the CHORUS [33] experiment and then re-arranged for OPERA experiment. It is written in MS Visual C++ with use of dlls, COM and ActiveX technologies. It includes many tools for acquisition, reconstruction and analysis.

The acquisition application has an object-oriented structure; the main code acts as framework for several modules. Each of these modules corresponds to a class interfaced and stored in a DLL file which accomplish a specific task (image processing, stage controller,...).

The logical scheme of the DAQ process is the following:

- execute an optical tomography of the whole thickness of the emulsion;
- recognize the grains in an emulsion image;
- detect the local alignments of the grains and reconstruct the particle tracks in the volume;
- correct the distortion of the tracks and extract their global geometrical parameters;
- store the tracks for further analysis.

4.7.1 Image processing

The image is digitized and converted into a gray scale of 256 levels (0 = black, 255 = white). Digital images are analyzed for the recognition of the dark spots (*clusters*) in the image: some of these spots are track grains of the emulsion; most clusters are spurious grains, not belonging to tracks but physically existing in the emulsion (the so-called fog grains); some clusters come from noise in the electronic signal.

The image of the emulsion is not too clear due to shadows caused by grains that are not in the focus plane so a *convolution* filter is used to enhance the contrast between focused grains and background. An example is a 3×3 high pass filter kernel:

-1	-1	-1
-1	9	-1
-1	-1	-1

Convolution is a local operation: the output value v_{ij} of the pixel at a specific coordinate is the weighted sum of the input values of the neighborhood pixels, the weights w_{lk} are given by the filter kernel; for a 3x3 kernel:

$$v'_{ij} = \sum_{l=-1}^{+1} \sum_{k=-1}^{+1} w_{lk} v(i-l)(j-k) \tag{4.5}$$

Then a *threshold* is applied to extract the dark spots that are candidate to become grains; the pixels are divided in two classes: the ones with the filter response above threshold, whose values in the binarized image are set to 0, correspond to the "white" pixels, and the ones with filter response below the threshold whose values are set to 1, are the "black" pixels.

In Fig. 4.6 and Fig. 4.7 the results of the processing of the grains and of a large area of the image are shown.

The last step of image processing is the *clustering*: the image is scanned row by row. Each sequence of black pixels found is called "segment" and stored in memory; this process is the most time-consuming, because it has to deal with huge amount of data. After a row has been scanned, the segments

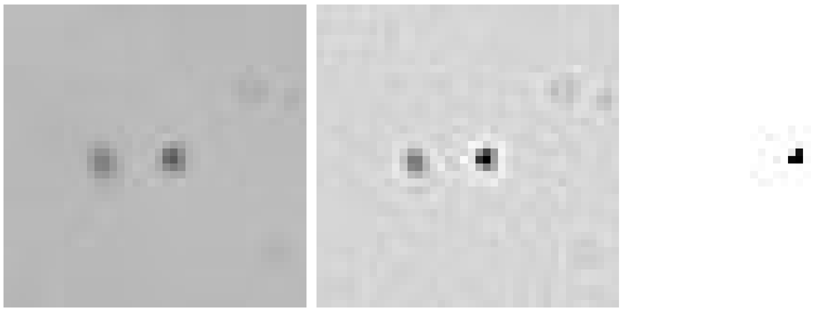

Figure 4.6: Image processing steps of an image with two grain at different focus. The first picture shows the grabbed image, the second the effect of the high pass 3×3 filter and the last the effect of the threshold. The second image has been scaled to have a 256 gray level image and to be properly displayed.

are compared with the segments in the previous row and adjacent segments are merged into a cluster. If two or more clusters come in contact, they are also merged. Finally, position, area and shape of clusters are given as results.

Depending on the illumination and the processing parameters, small clusters, i.e. composed by only 1 pixel, can be discarded since they are mostly due to the noise in the camera signal.

4.7.2 Track Recognition

The following step consists in combining grains from different layers to recognize geometrical alignments. The tracking efficiency can be affected by distortions of the track, then the algorithm must take into account this phenomenon.[9]

The field of view is subdivided in cells about 20 μm wide. Local align-

[9] The tracks should be straight; but due to the developing process, straight tracks are turned into parabolas: the point lying at the interface between the emulsion and its support remains in its original position, and the slope of each track at its exit point in air is left unchanged. In any case, since the OPERA emulsion are very thin, distortions vector can be small and the effect not dramatic.

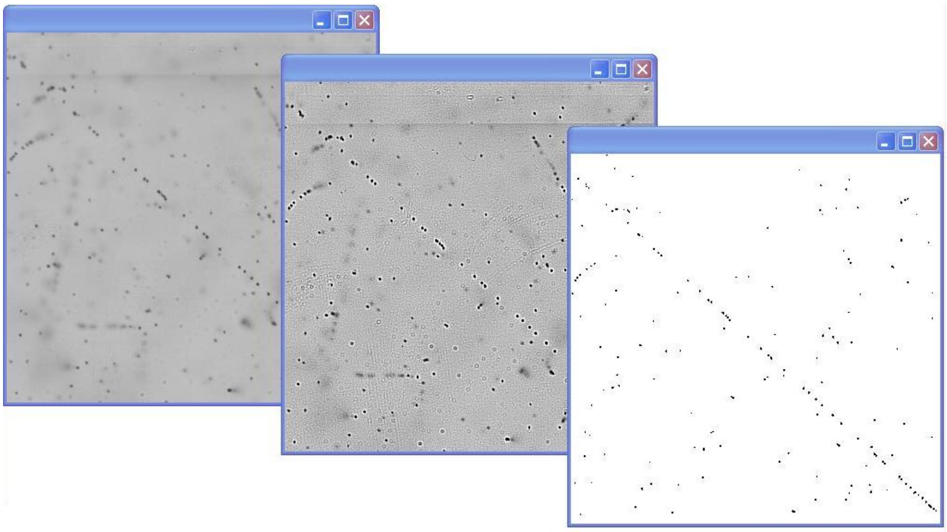

Figure 4.7: Image processing on a large area of the image: grabbed image, high pass filter and threshold.

ments of grains are then detected within each cell and across boundaries of neighbouring cells.

The search starts from a combination of all the grains in two distant layers and then requires some aligned grains in the inner layers (*track startup*), Fig. 4.8; the requested alignment tolerance and the layers to be used in this phase depends on the feature of the emulsions and on the quality of the track to be searched for. When such alignment is found, the computer looks for more aligned grains in the cell of the next layers which is predicted by the track fitting, (*track following*). This procedure stops when one or more empty layers are found.

While a track is being built, it may cross some already existing track. In this case, if the tracks share three consecutive grains, they are joined together in a single entity.

When a track stops both in the upward and downward directions, the number of points collected is compared with a minimum threshold (for example 8 points), required to store the track in the final data array.

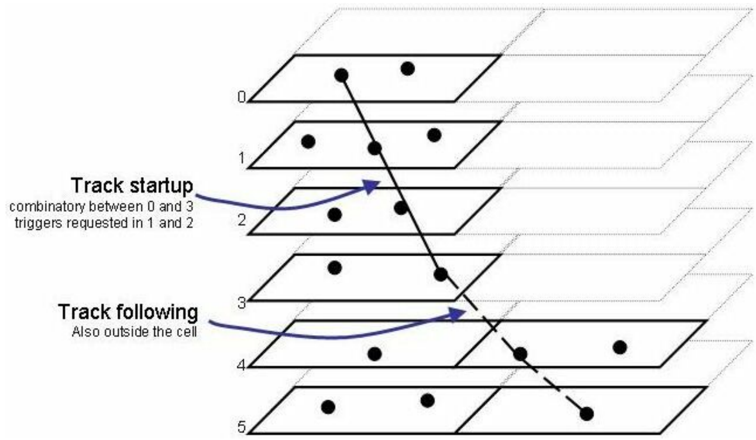

Figure 4.8: The tracking algorithm. The track startup takes place only in a cell stack to reduce computing time. The track following phase is allowed to change cell stack.

4.7.3 Track Postprocessing

After all the tracks in a field have been recognized, they must be corrected for geometrical distortions.

The tracks that pass the whole thickness of the emulsion layer are used to estimate the distortion vector, which is then used to correct the positions of the grains of all the tracks in the current field. This correction relies on the assumption that the slope at the exit point is the original one [31], Fig.4.9. Sometime this is not exactly true, and gives rise to some systematic deviation of the computed slopes from the real values. However, this kind of measurement error is not unrecoverable, and also an off-line correction is possible. Another requirement is that the point lying at the interface between the emulsion and its support remains in its original position.

As already stated, emulsions shrink during the developing process. So, when they are scanned, the thickness is usually less than the original one. The reconstructed tracks are then "expanded".

Finally, for each track some global parameters are calculated: slope, intercept with the emulsion base, standard deviation of the grains to the fitting line

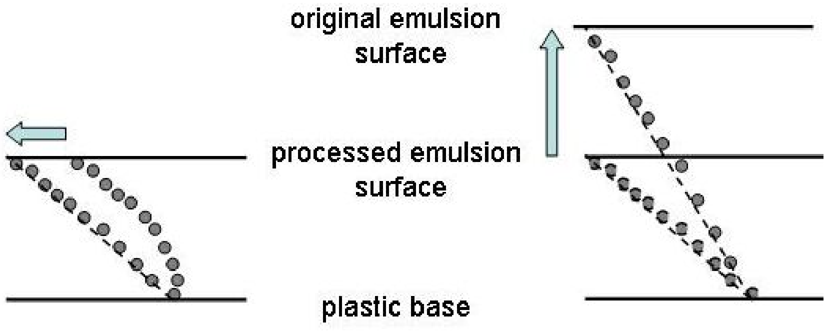

Figure 4.9: Distortion corrections applied to the reconstructed tracks.

The process described above is repeated for each of the two sides of the emulsion. When this process is over all the tracks in the scanning field are reconstructed without any selection in slope so that the whole information present in the emulsion is stored and available for the analysis.

The base-track is defined by joining the two micro-track points closest to the plastic base. Since these points lie in regions unaffected by distortion effects, the base-track has an angular resolution approximately one order of magnitude better than the micro-tracks. Thus the angular difference between micro-tracks and basetrack will provide an estimation of the micro-track angular resolution [26].

The base-track reconstruction is performed by projecting micro-track pairs across the plastic base and searching for an agreement within given slope and position tolerances. For each couple of micro-tracks that satisfy position and angular cuts, a χ^2 is calculated as

$$\chi^2 = \frac{1}{4}\left[\frac{(\theta_{xt}-\theta_{xB})^2}{\sigma_x} + \frac{(\theta_{xb}-\theta_{xB})^2}{\sigma_y} + \frac{(\theta_{yt}-\theta_{yB})^2}{\sigma_y} + \frac{(\theta_{yb}-\theta_{yB})^2}{\sigma_y}\right] \quad (4.6)$$

where $\theta_{xt(b)}$ and $\theta_{yt(b)}$ are the projections of the top (t) and bottom (b) micro-track angles in the z - x plane and z - y plane, θ_{xB} and θ_{yB} are the same projections for the base-tracks (B) and x and y are the micro-track angular resolutions.

4.8 Performances of the Bologna scanning system

From 2002, when the first prototype was installed in the Bologna Laboratory, a large effort was made to improve the stability of the system, to understand possible sources of inefficiencies and to increase the purity in order to fit the requirements of the experiment.

The system reached its final configuration in summer 2004 and became suitable for physics measurements. In this section I will present the performances of the Bologna system in terms of angular resolutions, efficiency and purity. I have obtained these results during my second year of PhD school and they were obtained from the track reconstruction in seven consecutive emulsion films (without lead in between) exposed at the CERN-PS.

4.8.1 Test beam exposure

The test beam exposure was performed in July 2007 at the CERN PS-T9 beam line. The equipment set-up was made of 2 multi-wire chambers and two scintillating fibers. Although the T9 beam can be normally operate up to 15 GeV, it was used a 10 GeV pion beam defocused on a total surface of about 10 x 10 cm^2 with an electron contamination at 6 GeV of about 1%. The angle distribution as measured with multi-wire chambers is shown in Fig. 4.10. The double peak visible on the Y-projection is due to the beam splitting upstream of the beam line. A track density of about 5 particles/mm^2 was integrated for each incident angle. 80 films were exposed and were distributed among different labs. The films were vacuum packed in two different packs of 40 films each.

The brick was tilted at 7 different angles (in the projection x) in order to study the angular dependence of the system performance. The 7 angles on X projection are 0. 100. -200. 300. -400. 500. -600. (mrad): Tab. 5.2 reports the number of events for each angle as measured with electronic detectors during the exposures.

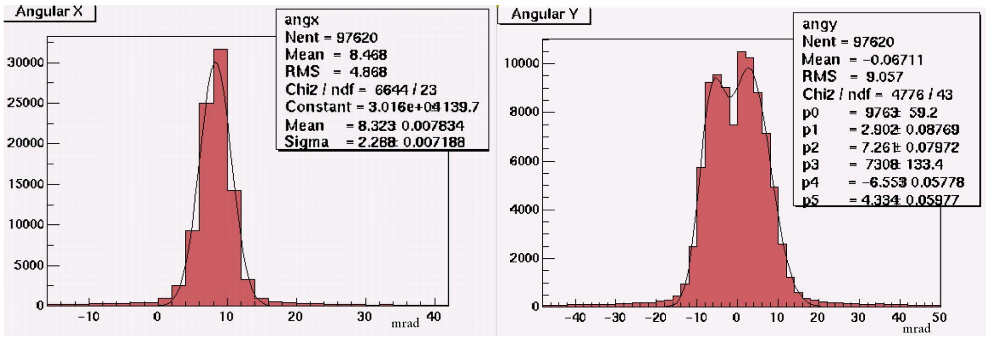

Figure 4.10: Angular distribution of the π beam at CERN PS-T9.

θ_x (mrad)	electronic counter
0	53158
100	52910
-200	53136
300	53529
-400	53713
500	52914
-600	54029

Table 4.1: Details of the exposure for the single-refresh sample at 10 GeV π.

4.8.2 Track analysis

Since the beam was uniformely distributed on the emulsion surface, for each angular exposure, a scanning of about 2.5 cm^2 was performed at the centre of each emulsion plate. Using the base-tracks χ^2 defined in Eq. 4.6 and the number of clusters associated to the linked micro-tracks, two populations emerge from the sample. A quality cut is defined to reject base-tracks with large χ^2 and small number of associated clusters (fake tracks):

$$\chi^2 \leq 0.66 \cdot PH - 9 \qquad (4.7)$$

where PH is the total number of clusters associated with a basetrack

This cut was applied to all the base-tracks of the scanned plates, and volume tracks have been reconstructed. In Fig. 4.11 the angular distribution of the reconstructed volume-tracks that passed all emulsion plates are shown. By considering only tracks measured in all the plates, the base-track angular and position residuals were calculated with respect to the fitted volume tracks. These residuals are dependent on the measured angles in the range from ~1 to ~7 mrad (Fig. 4.12). The corresponding position resolution ranges from ~1 to ~3 μm depending on the slope of the track.

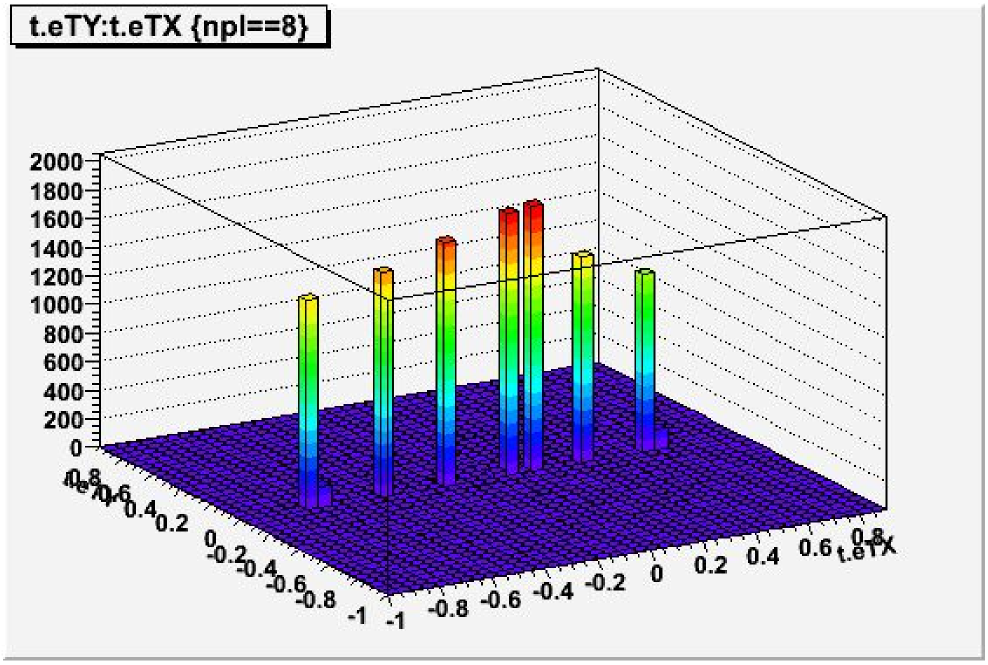

Figure 4.11: Reconstructed slopes of tracks obtained *linking* basetracks from different plates.

4.8.3 Efficiency and background estimation

During the exposures the emulsion sheets accumulated significant quantities of background due to cosmic rays and environmental radioactivity. While some tracks can be removed off-line with the quality cut, many cosmic ray

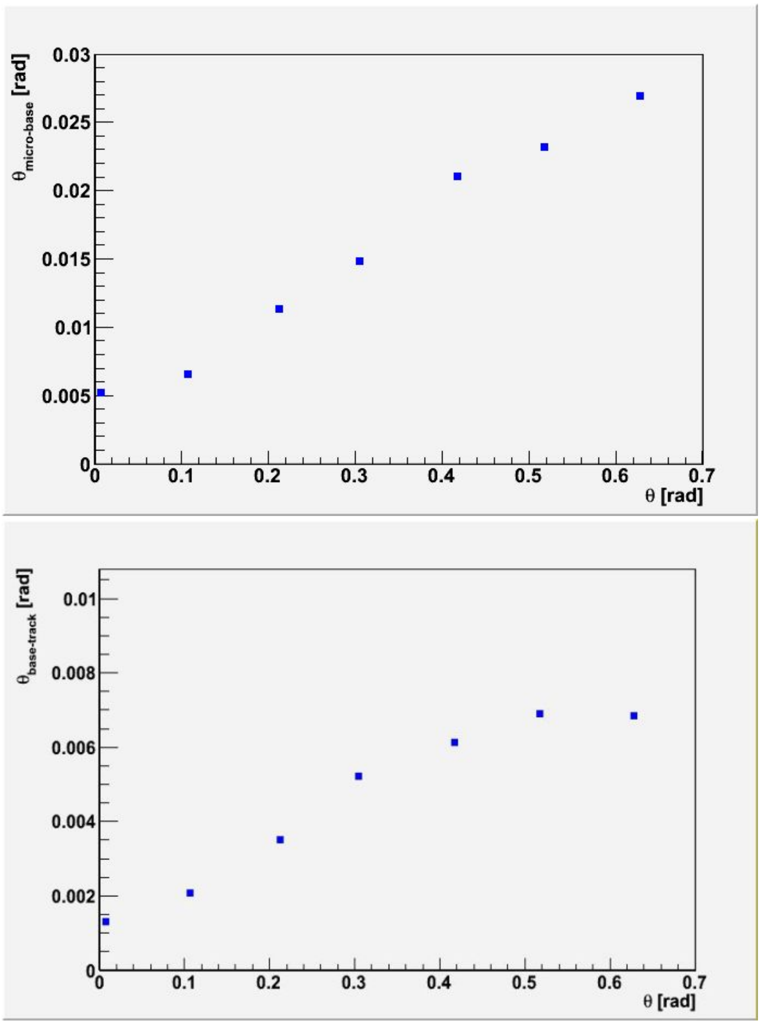

Figure 4.12: (top) The angular resolution of the micro-tracks as a function of the base-tracks slope. It is evaluated comparing micro-track angles with respect to the base-track angles. (bottom) The angular resolution of the base-tracks as a function of the volume track slope. It is evaluated comparing base-tracks angles with respect to the volume-track angles.

tracks can be mistakenly identified as beam-related tracks. In order to minimize the number of base-tracks not related to the pion beam, efficiencies have been evaluated taking into account volume-tracks with at least six (not necessary adjacent) base-tracks and with a reconstructed angle within 3 sigma of the beam directions. The base-track finding efficiency is then defined:

$$\epsilon_{tracking} = \frac{Number\ of\ measured\ base - tracks}{Number\ of\ base - tracks\ searched\ for} \tag{4.8}$$

where the number of base-tracks searched for is given by the number of the volume track sample times the number of scanned plates. The base-track tracking efficiencies have been calculated separately for each beam direction with respect to the optical axis; the results are shown in Fig. 4.13.

The mean efficiency is $\sim$80% and the shape of this curve is due to the number of grains associated to the base-tracks. As it is shown in Fig. 4.13, the number of grains has a minimum between 200 and 300 mrad and, from θ $>$ 300 mrad, increases with the slope. Base-tracks with a slope close to zero have more clusters due to the *reinforcement* of grains with their shadows.

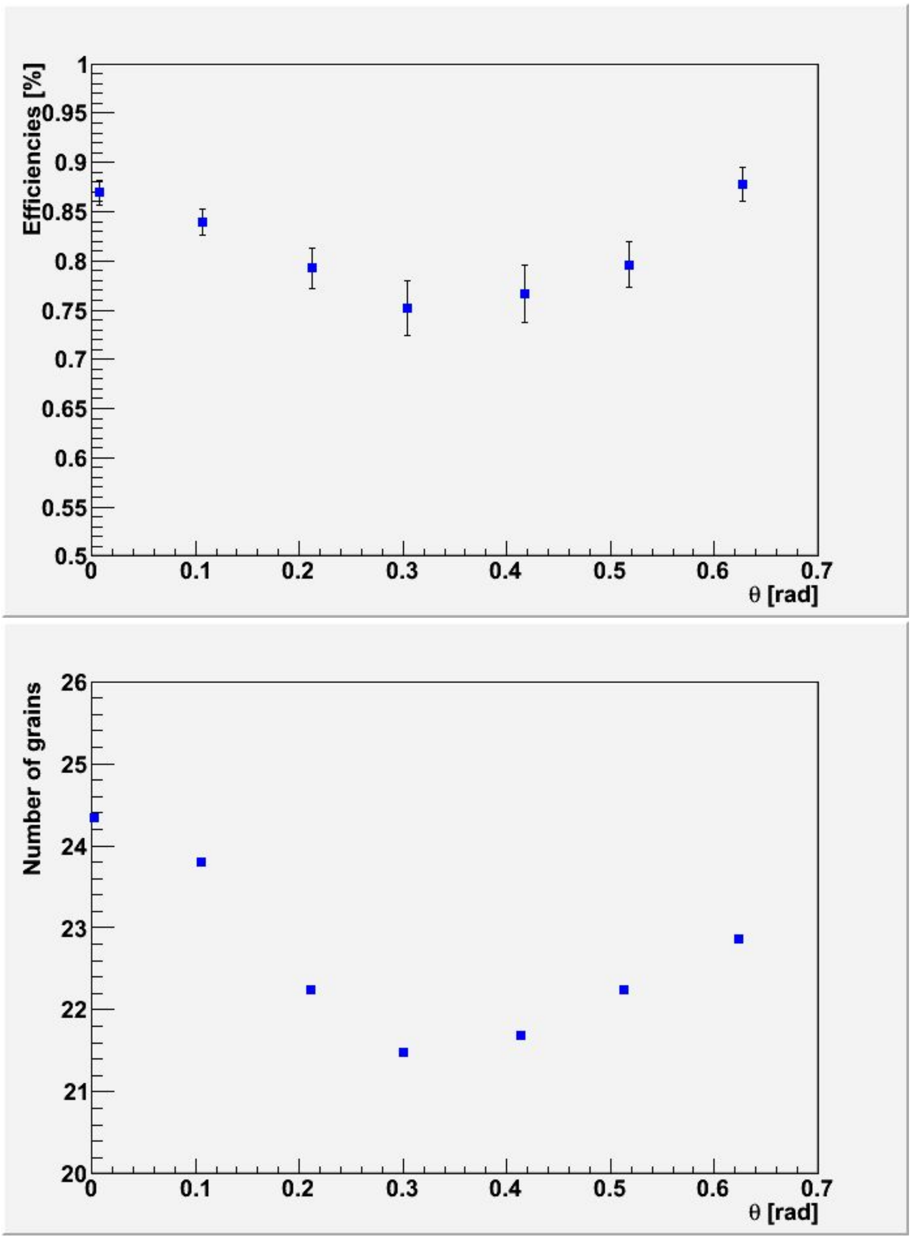

Figure 4.13: Top: Base-tracks finding efficiency as a function of the reconstructed volume tracks slope. Bottom: Avarage number of grains associated to a base-track as a function of track slope

Chapter 5

Localization and reconstruction of interactions vertexes in the OPERA bricks

When a neutrino interaction occurs in the OPERA detector and is triggered by electronic detectors the following procedure is applied:

- a 3D probabilty-map is evaluated using electronic detectors data to find the position of the brick in which the interaction took place, and it's extracted the one with the highest probability to contain the neutrino interaction;
- this brick is removed from the target wall by the Brick Manipulator System and exposed to X-rays for film-to-film alignment in the undergroud laboratories. Two different exposures have to be done: the first one is needed to ensure a common reference system to the Changeable Sheets doublet and the brick (frontal exposure) while the second one produces thick lateral marks on the brick edges, used for internal alignment and film numbering;
- after that frontal X-Ray marking is done, the CS doublet is detached

from the brick and developed underground, while the brick is kept in a box made of 5 cm thick iron shielding to reduce the radioactivity background waiting for the CS response;

- if the CS analysis confirms the electronic predictions the brick is exposed underground to the second X-ray marks. The brick is then taken to the surface laboratories and exposed to cosmic-rays in a pit for about 24 hours with an iron shielding used to select pentrating tracks and to provide straight tracks for sub-micrometric film-to-film alignment;

- after the cosmic rays exposure the brick is sent to the development facility. At this step the brick is dismounted and labelled with a frontal optic marks system which give another reference system (not aligned because the marking is done after the brick has been disassembled) and label the emulsion plates. Five automatized developing machines are working at LNGS and during the 2008 run they developed ~800 bricks and more than 1600 CS;

- the last step is to deliver bricks to scanning labs.

The goal of the this theses is to set-up and tune the procedures needed to localize and reconstruct events in the OPERA bricks.

In the following sections I'll describe the procedures which I've applied in the Bologna scanning laboratory for neutrino-interaction localization and reconstruction and the results obtained, with some details on the run-2008.

To illustrate the differet phases of the work I will use also as example the first OPERA neutrino event triggered in the detector (2-Oct-2007) during the first physics run held in the 2007 with 40% of target section filled with bricks. The run was very short in duration, due to failures of the ventilation control units of the proton target at CERN, caused by high radiation level in the area where the units are installed. The first brick where the first interaction took place was sent to the Bologna laboratory and I've specially worked on it.

5.1 TT-CS connection

Data are extracted from the DAQ data base every 12 hours and all events are processed through the OPREC reconstruction package. In time events are selected and stored. Then all in time events are sorted by categories:

- magnet interaction;
- rock muon;
- in target event CC or NC like (according to the muon identification).

The interactions in the material surrounding the OPERA target are analysed separately and are used to monitor the CNGS beam and the OPERA detector. The CS extraction is done according to a probability map: the CS with the highest probability to have the interaction inside is developed.

The connection between electronic detector and CS is performed at the LNGS scanning station which is equipped with 6 ESS. Each emulsion is scanned according to an area depending on the event type: for CC events the area scanned is ~5x5 cm^2 around the Target Tracker prediction. For NC events the whole emulsion surface is measured. A prediction is confirmed if it is seen on both emulsions films as a basetrack. In Tab.5.1 is shown the efficiency of finding the muon predicted from electronic detectors in the CS doublet evaluated with real data. The efficiency of finding the muon as a double base track (4 micro-tracks) is ~69% and increases to ~73% using one base-track plus one micro-track. In Fig. 5.1 is shown the residuals between the muon predicted by electronic detectors and the track found in the CS emulsions: the agreement is better than 1 cm and ~15 mrad.

If no muon candidate is found, the brick can however be developed if some others tracks are found in the CS which can be related to the event (for example converging tracks). For NC events no tracks are predicted by electronic detectors: the brick is developed if double base-tracks are found in the CS (hopefully converging).

In Fig. 5.2 is shown the electronic detector hits which occured for the first OPERA event. A penetratring muon is clearly visible.

CC measured	344
CC muon candidates found in CS	253
CC muon candidate found with double basetracks	237
Efficiency$_{4/4}$ [%]	$\sim$69$\pm$4
Efficiency$_{3/4}$ [%]	$\sim$73$\pm$3

Table 5.1: Summary table for muon connections in the CS. An estimate of the efficiency to recongnize the muon in the CS has been evaluated from real data.

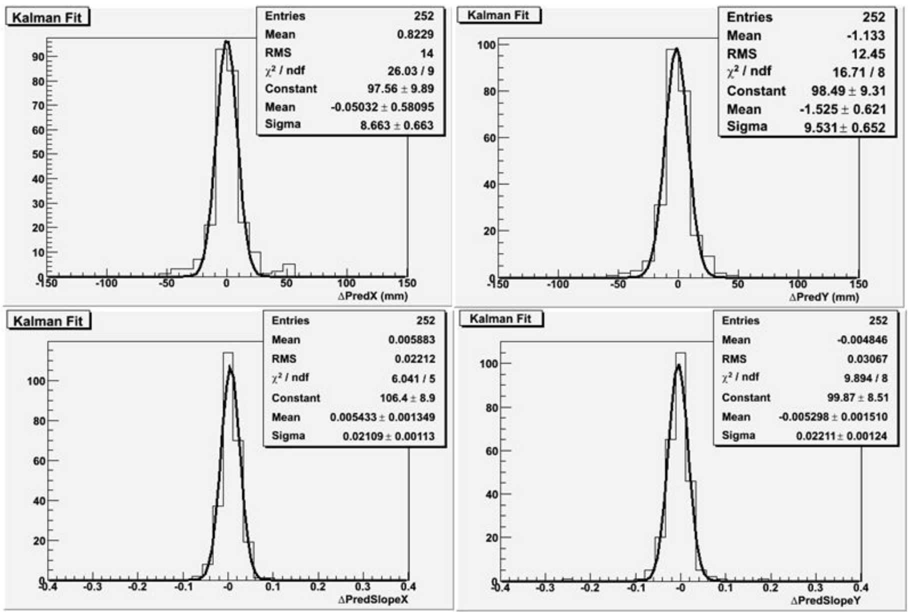

Figure 5.1: Residuals between predicted muon tracks by electronic detectors and tracks found in the CS emulsions.

In the CS measurements the muon track was not recognized even if three converging tracks were found: thus the brick 1029351 was developed.

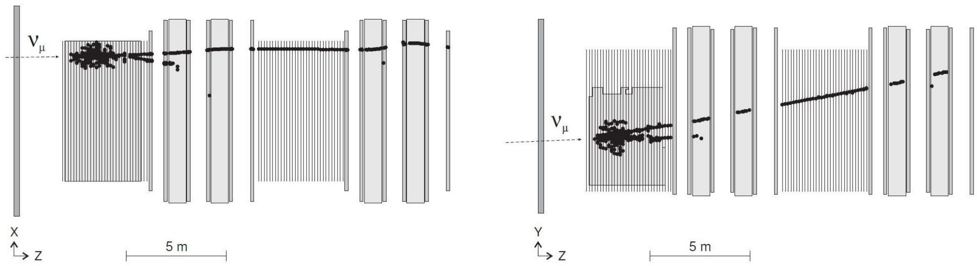

Figure 5.2: Top and side views of the electronic detector hits for the first OPERA event occured during the first short physics run in October 2007: the muon track is clearly visible.

5.2 CS-Brick connection

The connection between CS and brick represents a very crucial phase due to the fact that CS are put inside a plastic box, 4500 micron far from the brick. During the commissioning of the experiment the CS-brick connection has been tested with $\sim$100 bricks and it was found that opening a window of 300 μm and 30 mrad the connection is possible.

Using these cuts the CS-brick connection is made for the OPERA events; in Fig.5.3 are shown the residuals between a sample of the tracks found on CS which have been connected to the brick in plate 57 for the physics run. However the plate 57 (the more downstream) can be quite distorted due to the BAM spider pressure and so the connection sometimes failes on this plate and it is mandatory to look for the candidate on plate 56 or 55. The X-ray marks printed on the CS doublet are printed only on the plate 57 of the brick so we have to change themarks system in order to have a common reference frame for all the films of the brick. The choice can be taken between the two reference marks-systems.

I've chosen the lateral X-ray reference system to avoid to spend time in the acquisition of three areas to collect cosmic rays for plate-to-plate alignment.

During the first part of the run, bricks were marked only with two lateral X-ray marks: passing from a system with four marks (CS frontal exposure) into one with only two marks (lateral X-rays exposure) has an intrinsic "prob-

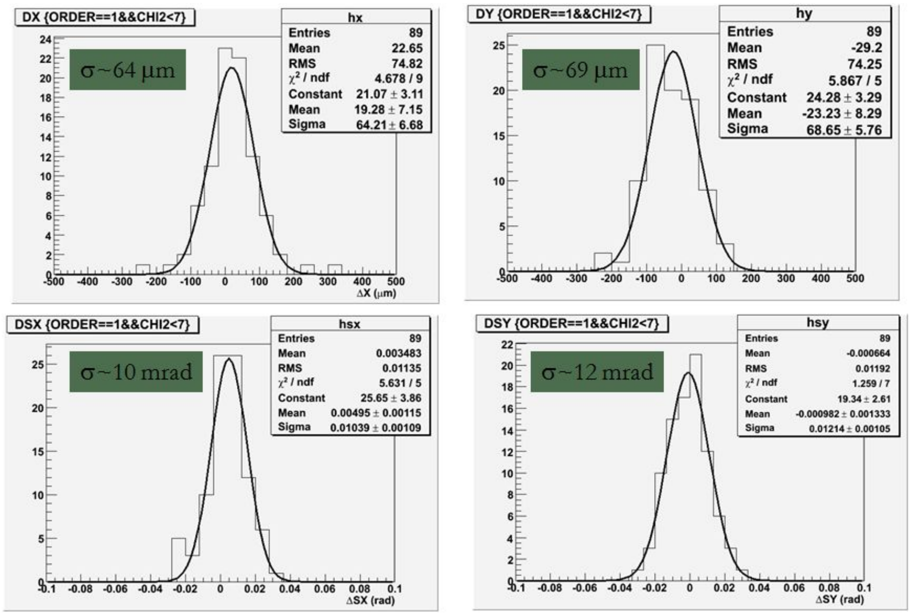

Figure 5.3: Residual between tracks (not only muons) found in CS and in the brick. The position residuals shows a sigma of ~70 μm and slope residuals of ~10 mrad.

lem" due to the fact that with only two points the affine transformation from one system to the other is not *well evaluated*. As a matter of fact, with two points only four independent parameters can be evaluated: two for traslation, one for rigid rotation and one for the scaling (same scaling for both axis). In Fig.5.4 (left) is shown the distance between a certain point evaluated in the four marks system and the same point evaluated in the 2 marks system: it is clearly visible that this distance increase if we go far from the 2 marks. In Fig. 5.4 (right) is shown the same map evaluated for the 4 marks system (4 CS-frontal marks to 4 lateral marks).

This "offset" between maps is relevant only for the "connection" between CS and brick if, for example, the preditions are not seen in plate 57 and it is necessary to look for them in plate 56 (on which there is not the X-ray Spot marks): in this case, with only two marks the position tolerances should be increased to take into account this *mathematical* problem.

For the 2008 run, the bricks are marked with four lateral marks to have a

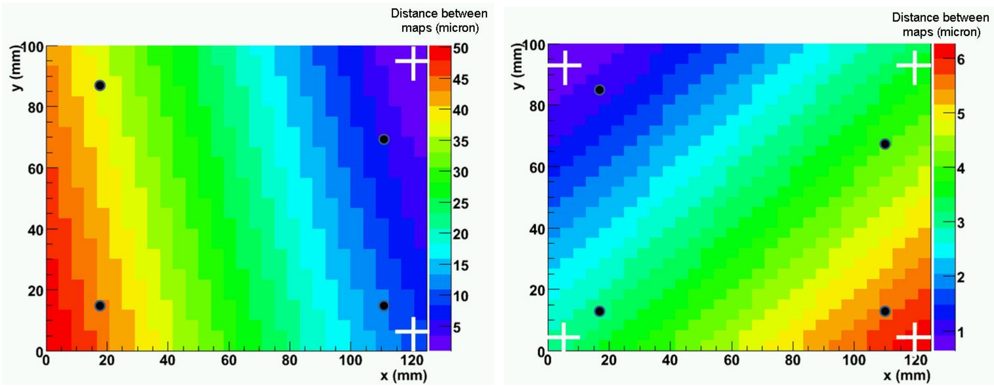

Figure 5.4: Distances between maps in micron: the rough positions of the marks used are shown in black spots (CS marks, the 1^st map) and in white crosses (lateral marks, the 2^nd map). The color code gives the distance evaluated for a given point between two differet maps for the whole emulsion surface. Left: distance between points evaluated using a 4 marks system and the same points evaluated using a 2 marks system. Right: distance between points evaluated using a 4 marks system and the same points evaluated using a 4 marks system. It is visible that this distance is less than 7 μm passing from the 4 CS marks to the 4 lateral marks while increase increase up to 50 μm for the other case.

better estimation of the transformation parameters and to have a redundancy in the case that some marks are not well printed.

Concerning the first OPERA event (the so called *opera-baby*) the three converging candidates found at LNGS are matched in the brick on plate 57. The tracks doesn't present distortion due to the spider pressure and the residuals between the predicted tracks and the found ones are shown in Tab.5.2.

5.3 Scanback

After that the match has been found all the tracks are followed inside the brick with a procedure called *scanback*; it is a procedure completely

track ID	dx [μm]	dy [μm]	dsx [mrad]	dsy [mrad]
1	10	-33	10	-6
2	8	-28	1	3
3	12	-44	-7	-6

Table 5.2: Residual between tracks measured on CS and propagated to pl57 (nominal distance -4500 μm) and the tracks measured on plate 57 for the first OPERA event.

automatized which relies on a continuous access to an Oracle Data Base (DB).The procedure starts from the most downstream plate and is done in two phases: the plate to plate intercalibration and the searching phase. The plate to plate intercalibration can be done in two different ways:

- the first one is made by localizing three fiducial spot-marks, and then by scanning three areas (0.8x0.8 mm^2) one far from the others in order to reconstruct cosmic ray tracks; for each plate in the areas a pattern match of cosmic ray tracks is made to find the affine transformation parameters to be used to track predictions across the whole brick;

- the second one is faster and consists in the acquisition of four lateral X-ray marks which are used as a unique reference system and which provide the plate to plate alignment (and this one is the procedure chosen in the Bologna laboratory).

The searching procedure is then applied on each plate: for vertical tracks the microscope moves to the X,Y predicted coordinates and looks for a base track that is in agreement with the X, Y, positions and TX, TY slopes of the prediction within 80 μm and 30 mrad tolerances respectively inside one field of view. For a not vertical track the tolerances increase according to these relations:

$$\Delta\text{pos} = 80 + 6 \cdot \theta[\mu\text{m}] \tag{5.1}$$

$$\Delta\theta = 0.030 + 0.05 \cdot \theta[mathrmrad] \tag{5.2}$$

If no track is found in a given plate, the prediction is extrapolated to the following plate and searched for in the corresponding area. If no track is found in a number of consecutive plates defined taking into account the scanning efficiency (in our case 5 for plates)[1], the track is defined as a *stopping track* and the position of the last measured base track is defined as the *stopping point*. Stopping points are further investigated looking for interactions.

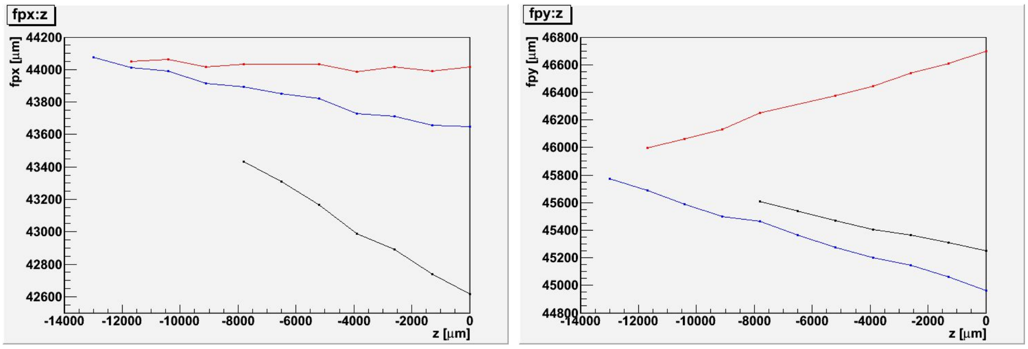

Figure 5.5: Scanback of the three predictions: X-Z projection (left) and Y-Z projection (right).

An optional tool is available in the online software to give the possibility to the user to visual inspect the tracks every time the system doesn't find them and, if the user finds the tracks, the system permits to to send the manual measurments flagged as *last seen basetrack*. In this way when a track really stops the user can have checked manually that the stop is not a fake one. Concerning the first OPERA event all the three prediction have been followed down inside the brick until the stopping point. Fig.5.5 shows the scanback pattern obtained for the first (*opera-baby*) event: one track stops on plate 51, quite far from the other two tracks but it seems however related to the interaction.

[1]Considering for example an efficiency of ∼80% the number of fake stops ranges from ∼40% if we consider as stopped tracks after 2 holes, down to ∼0.4% if we consider as stopped tracks after 5 holes.

5.4 Totalscan

A volume scan around each stopping point is performed in order to confirm (or disproof) the existence of a vertex from a neutrino interaction. This procedure is called *Total Scan* (TS). A TS volume is defined by 1 x 1 cm^2 in 13 consecutive plates: the plate containing the stopping point, five plates upstream and seven plates downstream. The Total Scan volume is tilted as the scan back track slope.

The analysis procedes through the following steps:

- Virtual Erasing;
- Alignment and tracking;
- Stop confimation and vertex Reconstruction;

5.4.1 Virtual Erasing

The virtual erasing procedure is needed to discard those tracks which crossed the emulsions during the fly from Japan to Europe. During the transport emulsions were piled up without lead and in the reverse direction with respect to the one used inside the brick: erasing from the data-files the cosmic rays accumulated during the transport reduces the background of basetracks not related to the cosmic esposure (used for the fine alignment) and to the neutrino interaction. In Fig. 5.6 is shown the alignment peak between two consecutive emulsion films for the *opera-baby* event.

5.4.2 Alignment and tracking

The next step is to perform the alignment and the tracking ordering the emulsions as they are in the brick. In Fig.5.7 is shown the pattern match between two consecutive emulsions in the exposure order after that the virtual erasing procedure has been done.

As I have shown in the previous chapter the tracking efficiency depends not only on the emusion quality but also from the slope of the tracks. For

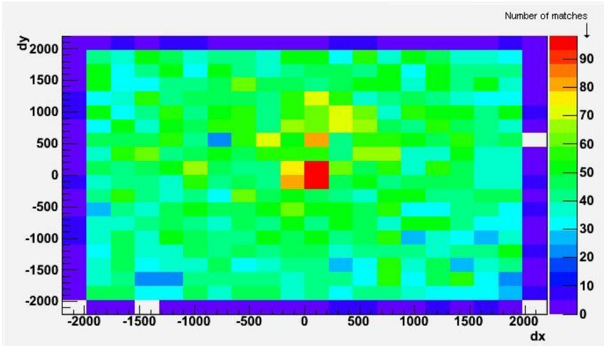

Figure 5.6: Matches between two consecutive emulsion sheets in the transportation order: the number of the matches as a function of relative emulsions displacement is shown.

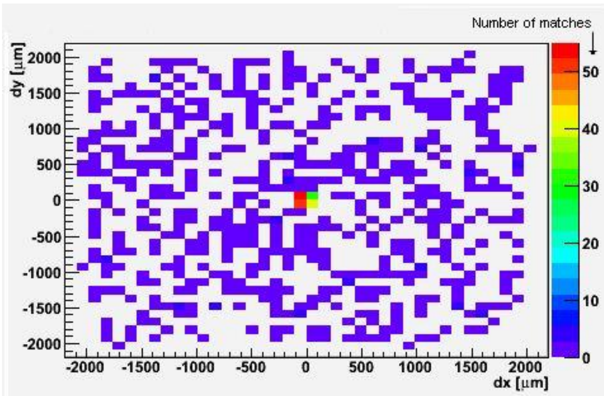

Figure 5.7: Matches between two consecutive emulsion sheets in the exposure order after the virtual erasing procedure: the number of the matches as a function of relative emulsions displacement is shown. A peak due to the cosmic rays exposure is clearly visible.

this first OPERA event I have chosen to performe a volume scan of 5 plates upstream of the stopping point and ten plates downstream (which in this case means up to the end of the brick): this choice is justified by the fact that one of the scanback tracks stops four plates downstream of the other two scanback tracks. The tracks seems however related to the event. In order to reconstruct also this track and may be something related to it the Total

Scan volume has been extended from the "nominal" one (13 plates).

In Fig.5.8 is shown the fill-factor for tracks which pass more than 10 plates as a function of the slope of the tracks: the fill factor is defined as the ratio between the number of measured segments for a given track and the total number of plates that are crossed by the track; a rough estimate of the efficiency is made. The fill-factor is ∼85% up to 0.1 rad and decreases to ∼65% in the range 0.2 - 0.4 rad.

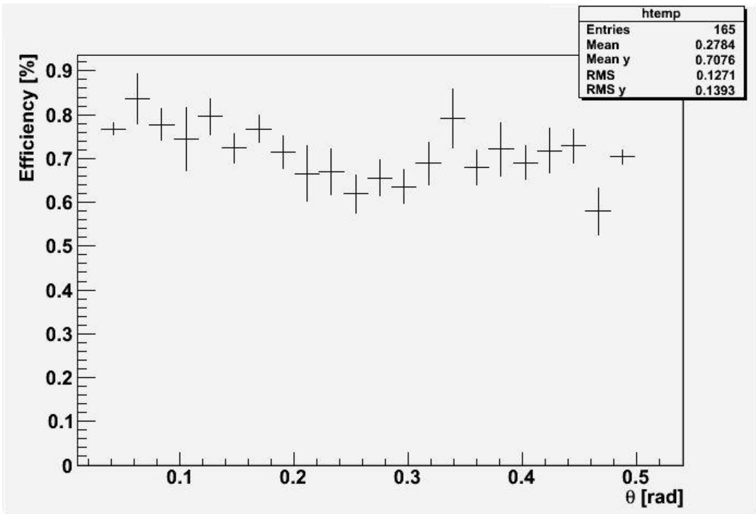

Figure 5.8: Fill-factor for tracks passing at least 11 plates as a function of the slope.

5.4.3 Vertex Reconstruction

The last step is the vertex reconstruction.

The tool used for vertex reconstruction is developed in a c++ ROOT based framework, called FEDRA. Vertex procedure considers all couples of volume tracks and link them into a 2 prong vertexes. This is done on the whole volume and three basic topologies are reconstructed (Fig.5.9):

- vertex with parent track or charged vertex;

- neutral forward vertex;

- back-forward vertex.

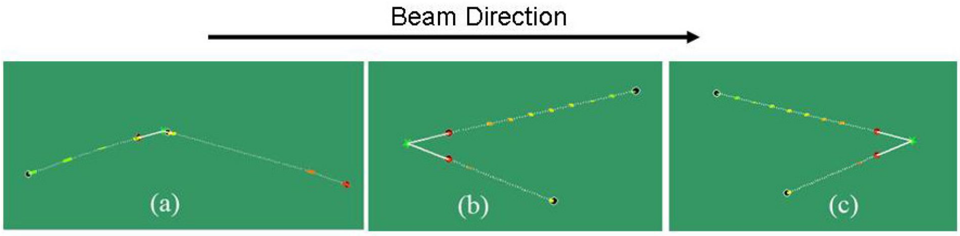

Figure 5.9: Basic vertex topologies reconstructed by the FEDRA analysis tool.

Combining these three vertex categories, FEDRA reconstructs all the other possible topologies. Taking into account the scanning efficiency and the plate to plate alignment accuracy we require the impact parameter (IP) to be smaller than 90 μm and the longitudinal track distance between the end of the measured track and the geometrical point of the vertex to be within 3500 μm: in this way it is taken into account some possible inefficiency in the acquisition of the segments near to the vertex and also the possibility that some tracks can come from a neutral particle emitted from the primary vertex. All tracks attached to the primary vertex which have some "*holes*" near the vertex are manually checked to confirm (acquisition inefficiency) or discard (neutral particle) the track presence.

At the end of the vertex procedure many "vertexes" are found mainly due to background tracks (expecially two prong vertexes have a high background). The first step is to recongnize the scanback track inside the volume and to check if it is attached to one vertex. If the event is a CC one, many cases can occur:

- if the scanback track is a muon and is associated to other tracks into a vertex, the primary interaction has been found and all the tracks beloning to that vertex are manually checked to confirm the interaction;
- if the scanback track is not the muon and is attached to some other tracks, one of which is compatible with the muon predicted by the electronic detector, the procedure is quite the same but the muon track

has to be followed down until the most downstream plate in order to check its presence into CS;

- if the scanback track is not the muon and is not attached to other tracks we try to recognize the muon inside the volume: if a track compatible with electronic detector reconstruction is found, it must be followed downstream until the CS to confirm the candidate;

- if the scanback track is not the muon and is attached to a parent charged track, the parent track has to be followed up to the primary interaction;

Once the real vertex is found I have developed a simple tool to search for tracks related to the vertex: this tool works considering two different approaches. In the first one all tracks which form an angle smaller than 0.05 rad with respect to the vertex point are considered tracks potentially belonging to the event; the second one looks for tracks wich have an impact parameter with respect to the vertex smaller than 90 μm. If a track satisfies both criterions this track is considered as a track of the event regardless of the longitudinal distance from the vertex. In this way it is possible to identify track which are due to a decay of a neutral particle emitted at the interaction point even if the decay occurs far from the vertex.

In Fig. 5.10 is shown the first OPERA event reconstructed by the emulsions. Two tracks quite far from the interaction vertex are *connected* to the vertex from the tool explained above.

I have inspected the two tracks with a high magnification objective (M = 100x). At the microtrack level the picture seems quite clear: the bottom microtrack appears as a "superimposition" of two very near microtracks which in the top emulsion layers appear as a double converging microtracks: this is a signal that those tracks are due to gamma conversions into an e^+e^- pairs.

In order to investigate the decay which leads to a double gamma we guess that they come from a π^0 decay; to test this hypothesis I have manually measured the opening angle between the e^+e^- (using the high magnification objective) for both tracks and then I have measured the γ opening angle

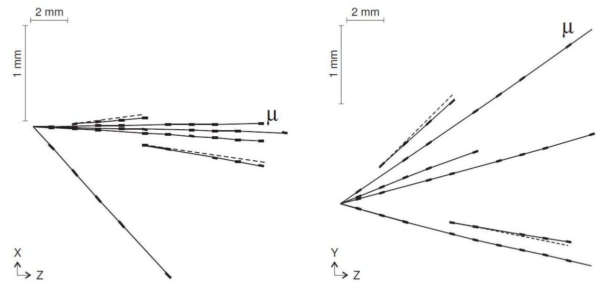

Figure 5.10: Vertex reconstructed in the emulsions. Two tracks quite far from the primary vertex are pointing to the vertex. Those tracks are gamma conversions into an e^+e^- pairs.

considering that the π^0 decay should occur very near to interaction vertex. Then I have estimated the invariant mass to verify the guess.

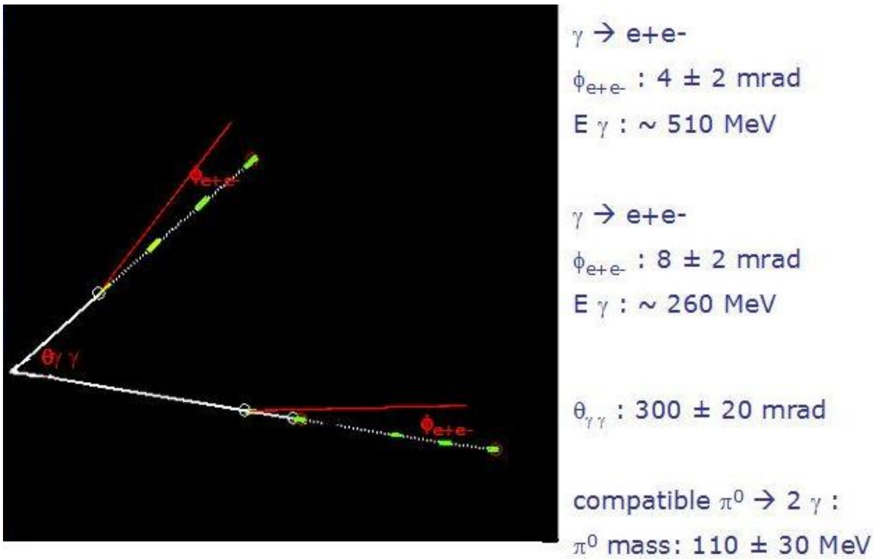

Figure 5.11: Sketch of the π_0 decay. One track of each e^+e^- pair is measured by the automatic system, the relative partner is seen by visual inspection and here is plotted in red (not in scale).

It can be demonstrated that the relation between the energy of the γ and the angular aperture of the electron-positron pair is [39]:

$$E_\gamma \approx 4\frac{m_e}{\phi_{e^+e^-}} \tag{5.3}$$

The invariant mass of the π_0 can be evaluated by the formula:

$$m_{\pi_0} = \sqrt{2E_{\gamma_1}E_{\gamma_2}\left(1 - cos\theta\right)} \tag{5.4}$$

Defining ϕ_1 and ϕ_2 as the angles between e$^+$e$^-$ pairs and θ the angle between the two gammas

$$\phi_1 = 4 \pm 2mrad \tag{5.5}$$

$$\phi_2 = 8 \pm 2mrad \tag{5.6}$$

$$\theta = 300 \pm 20mrad \tag{5.7}$$

the invariant mass is

$$m = 110 \pm 30MeV \tag{5.8}$$

which is compatible with the mass of the π_0 particle.

5.4.4 Momentum estimate

In order to have a kinematical reconstruction of the events the track momentum measurement is needed. This can be done via two methods: the *position* (or sagitta) method and the *angular* method. These methods measure the deviation from a straight line using position or angle measurements. The use of one method rather than the other depends on the accuracy needed and on spacial and angular resolutions. The OPERA emulsions made with two gelatin layers interleaved by a plastic base give an excellent angular resolution (∼1 mrad) so the angular method is chosen. The angular method does not depend one the precise knowledge of the relative position of the different emulsion layers. The Coulomb scattering distribution at small angles is well represented by the theory of Moliere [37]. If we ignore the small probability of large-angle single scattering, the probability distribution is approximately Gaussian in form

$$P(\Theta)d\Omega \approx \frac{s\Theta}{\langle\Theta^2\rangle}exp\left(-\frac{\Theta^2}{\langle\Theta^2\rangle}\right)d\Theta \tag{5.9}$$

The parameter $\langle\Theta^2\rangle$ represents the mean squared scattering angle. The squared root $\Theta_0 = \sqrt{\langle\Theta^2\rangle}$ is know as the RMS scattering angle and should be equal to the RMS scattering angle of the full multiple scattering angle distribution. An estimate of Θ_0 is obtained by using an empirical formula [38] which is valid to within 5% for $Z > 20$ and for target thicknesses x between $10^{-3}X_0$ and $10X_0$:

$$\Theta_0 = \frac{13.6\mathrm{MeV/c}}{pc\beta} z \sqrt{\frac{x}{X_0}} \left[1 + 0.038 \ln \frac{x}{X_0}\right] \tag{5.10}$$

where X_0 is the radiation length of material; x is the thickness of material; p is the momentum of the particle; z is the charge of particle (Θ_0 is expressed in radiant). Concerning the muon reconstructed in the emulsions for the first OPERA event, only few plates are usefull to estimate momentum because the neutrino interaction occured very downstream in the brick. The evaluated value for momentum is:

$$p = 4.0^{+243.6}_{-2.0} GeV \tag{5.11}$$

To improve the momentum estimation the downstream brick is requested, the brick 1029437. The nominal longitudinal distance between these bricks is ~6.1 cm. I try to connect three tracks from the upstream brick (one is the muon, the other two are hadrons which have a "hit" on plate 57). A volume scan of 1.6x3.2 cm^2 multiplied by 4 plates (from plate 1 to plate 4) of the downstream brick was measured and the connection was attempted with a postion tolerance of 5 mm and an angular tolerans of 30 mrad. The match was found and all the tracks were follwed down inside the brick untill plate 57 (scanforth procedure).

In Fig.5.12 is shown the fit to the measured muon reconstructed in the emulsions; the momentum was estimate to be:

$$p = 8.9^{+45}_{-5} GeV \tag{5.12}$$

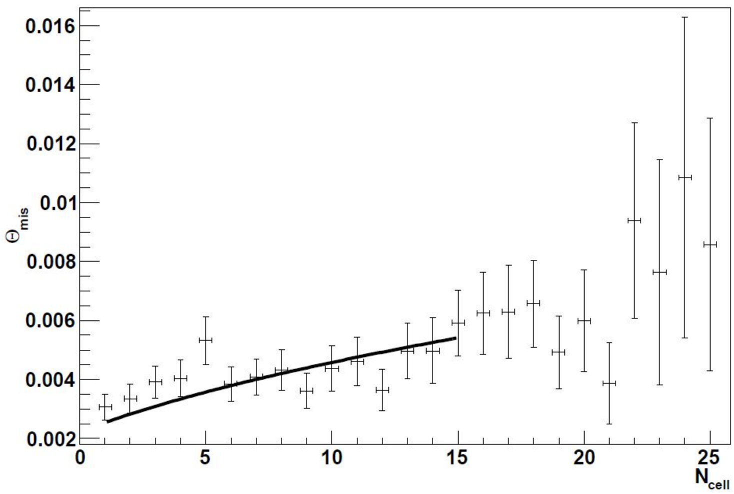

Figure 5.12: Scattering angle as a function of the number of emulsion plates transversed by the track.

5.5 NC Event analysis example

As a significant example on what has to be done to locate neutrino events in the OPERA emulsions in some "difficult" cases I will show here the work that I have done for a NC event which has occurred in the detector in the day 06/07/2008. In Fig. 5.13 is shown the zoom of the electronic detector superimposed with the tracks recognized in the CS. The probability map evaluated by electronic detector recostruction is indicated in Tab. 5.3

The brick 1005538 was sent to the Bologna scanning lab with six CS predictions: three out of six predictions were matched inside the brick but the scanback procedure stops on the plate 57 (the plate near the CS). In Tab. 5.4 is shown the residuals between CS prediction and tracks found in plate 57. The manual check confirms the stopping points and a volume of 1 cm^2 multiplied by 28 plates (from plate 30 to plate 57) were measured in order to check if those tracks can be produced by an electromagnetic shower.

The algorithm for the reconstruction of the shower follows an iterative procedure [36]. For each basetrack (called here "selector") the software looks for base-tracks matching it in the downstream emulsion plates. The matching

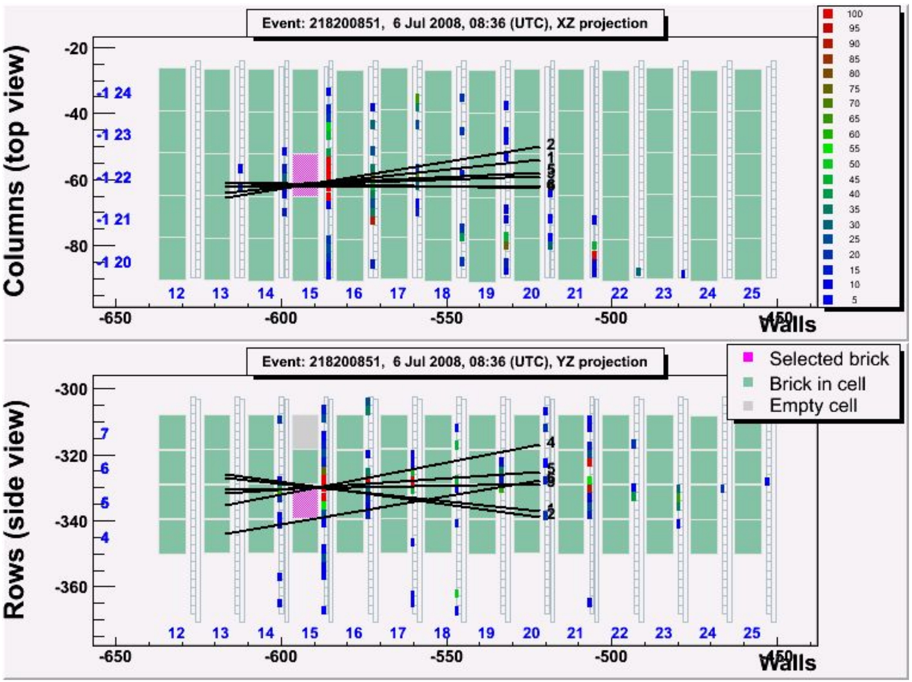

Figure 5.13: Electronic detector display of the NC event 218200851 . CS tracks have been superimposed on the diplay: one track is clearly non related to the event. The pink brick is the number 1005538 which was sent to Bologna: the CS tracks stop inside this brick and don't cross the brick (as it may seem from the above electronic display).

criteria is based on angular and position requirements: the angular displacement $\delta\Theta$ is defined as the angle difference between the selector and the base-track candidate while the position displacement δr is the transverse distance between the selector and the candidate extrapolated back to the selector. Any matched candidate becomes a selector and so on and a base-track candidate is discarded if no match is found in 3 downstream films. To reduce the background, base-tracks must be within a cone (with the axis defined by the slope of the first base-track belonging to the shower) with an opening angle of 20 mrad (angle was optimized by a Monte Carlo): this "showering package" is included into the FEDRA framework.

In Fig. 5.14 (left) is shown the position of basetracks that are matching

Brick	Prob [%]
1005538	24.83
1005524	23.17
1005539	12.30
1004019	4.64
1005526	4.30

Table 5.3: Probability map for NC event 218200851. Some tracks were found in the CS for the brick 1005538 (the one with the highest probability): this brick was sent to Bologna scanning Lab.

track ID	dx [μm]	dy [μm]	dsx [mrad]	dsy [mrad]
1	64	64	-20	-11
2	35	31	-30	23
3	-1	96	-9	-7

Table 5.4: Residual between tracks measured on CS and propagated to pl57 (nominal distance -4500 μm) and the tracks measured on plate 57 for the NC event 218200851.

the criteria written above: it is clearly visible a peak (in red) which is due to a shower in the brick. In Fig. 5.14 (right) is visible a vertex: one of the tracks attached to the vertex contains the basetracks which is the "mother" of the reconstructed shower. In the shower are also present the tracks found in the CS and connected to the brick: this confirms that the tracks in the CS come from the shower. Related to the pair one track was found upstream and was followed with the scanback procedure; it stops on plate 4 where the manual check confirms the stopping point. The totalscan procedure recognizes a three prong vertex as shown in Fig. 5.15.

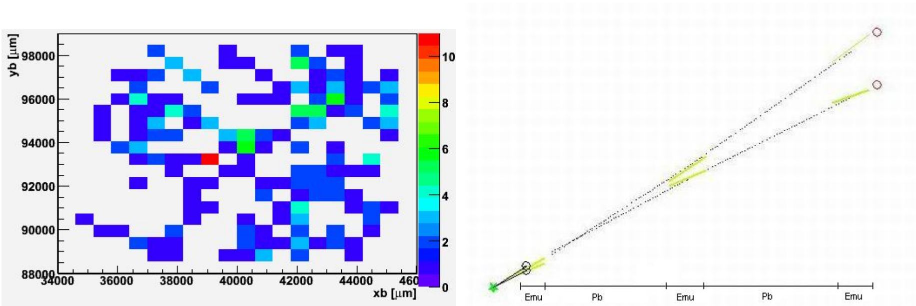

Figure 5.14: Left: Position of the basetracks which are *collected* by the shower algorithm applied to the volume scan of the event 218200851. A shower hint is visible (red bin). Right: Vertex found at the primary of the shower: the base track found to be the primary of the shower is attached to the vertex. A parent track related to the vertex is followed with the scanback procedure.

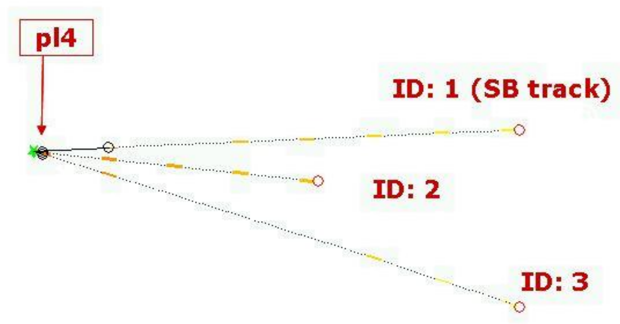

Tracks statistics:

Id	Ip	TX	TY	Nseg	DZ
1	7.1	0.083	0.031	6	-1495.7
2	0.9	0.115	-0.074	5	- 192.5
3	0.2	-0.179	-0.210	5	- 192.5

Figure 5.15: Display of the primary interaction found following the track related to the shower.

5.6 2008 run

The 2008 run starts the 18th of June and end the 3^{r}d of November. In Fig. 5.16 is shown the proton on target (pot) during the run. The start of the run is done with a low intensity beam and it was the commisioning phase.

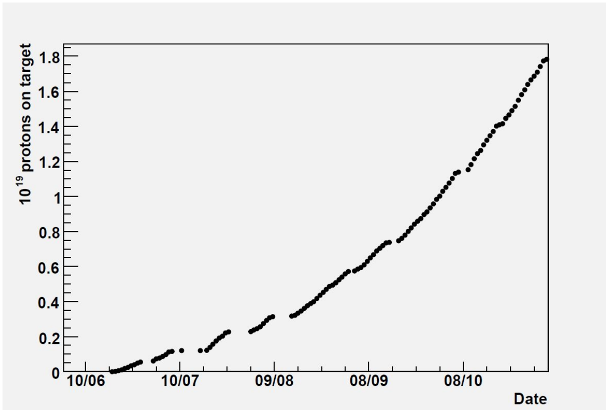

Figure 5.16: Integrated number of proton on target (p.o.t) as a function of time for the 2008 CNGS run (June-November)

During the run there were some troubles that lead to some beam stops (vacuum accident, 10 kV cable accident, ecc.).

The integrated number of pot delivered during the 137 days of data taking was 1.78$\cdot 10^{19}$. The number of events acquired is ∼10.5 millions, ∼10100 of which were on time with the CNGS. ∼1700 evens occurred inside the bricks.

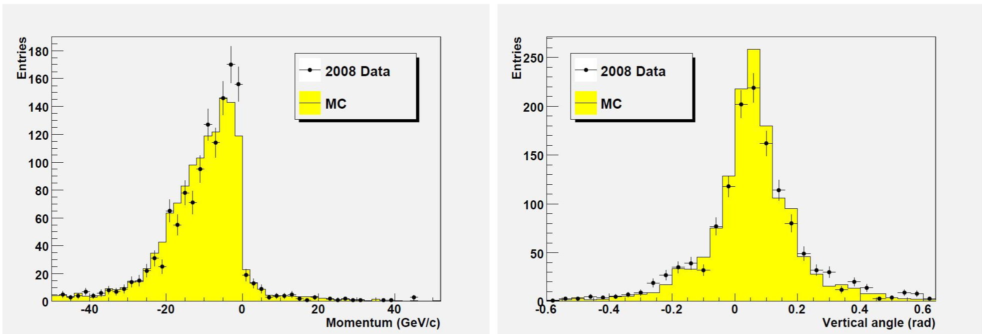

Figure 5.17: Left: momentum distribution of muons produced in CC neutrino interactions inside the OPERA target. Right: angular distribution of the muon tracks with respect to the horizontal axis.

In Fig. 5.18 (left) is shown the angular distribution of muon tracks inside the OPERA target with respect to the horizontal axis; Fig. 5.18 (right) shows the momentum distribution of muons. The beam direction angle is tilted by 3.3°, as expected from geodesy.

5.6.1 Preliminary Results

The analysis of the events collected during the 2008 run is in progress in all the laboratories of the collaboration: however some preliminary results can be shown here.

	NC	CC	Total
Bricks assigned	83	441	524
Bricks received	78	394	472
Scanning started	74	388	462
CS to brick connected	67	368	435
Vertices located in the brick	43	293	336
Passing through	8	23	31
Vertices in the dead material	1	7	8

Table 5.5: Preliminary statistics related to bricks assigned to European scanning laboratories.

As it is shown in Tab. 5.5, up to now 472 bricks were assigned and received by the European laboratories: among these 394 bricks contain a charged current interaction, the others NC interactions. The table above shows that ∼2.4% of the events occurred in "dead" materials[2]. The efficiency in locating the events ranges from 82% to 95% for CC events and from 66% to 91% for NC events: the upper limits are evaluated assuming that all *pending events* will be localized while the lower limits are evaluated assuming that none of the events still not recognized will be found.

[2]dead materials mean scintillator, plastic box near the brick, ecc...

In the Fig. 5.18 are shown the multiplicity of reconstructed events CC and NC (Europe side):

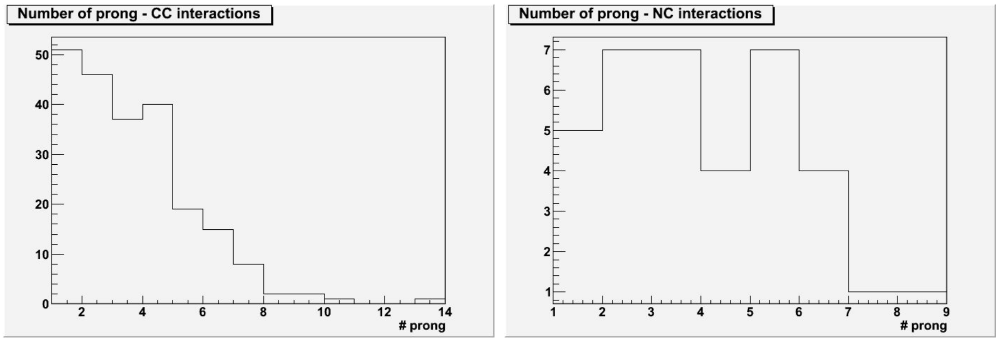

Figure 5.18: Left: number of prong for CC interactions. Right: number of prongs for NC interactions

A very "peculiar" event is shown in Fig. 5.19: the neutrino interaction occurered in the bottom layer of an emulsion film. Therefore, the associated nuclear fragments (large angle heavy ionizing tracks) are visible.

In the Fig. 5.20 is shown the impact parameter of all the tracks attached to the primary vertex: the shape of the distribution shows that the cut applied during the vertex reconstruction doesn't remove tracks from the primary vertex. If we consider the impact parameter of the muon only it has a mean value of ~2.6 μm. As examples, in Fig. 5.21 and in Fig. 5.22 are shown a NC and a CC event, respectively, fully reconstructed in the brick; both occurred during the 2008 run.

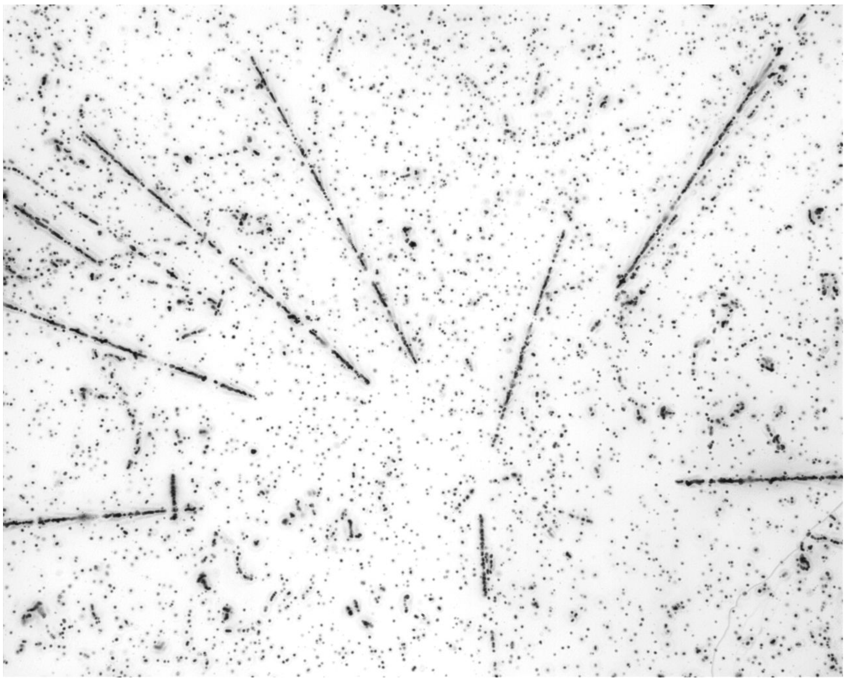

Figure 5.19: Super-position of images grabbed with a high magnification objective by moving the focal plane with steps of $\sim$2 μm. Many black tracks due to nuclear fragmentation are visible: those tracks pass only one emulsion layer (one microtrack is visible).

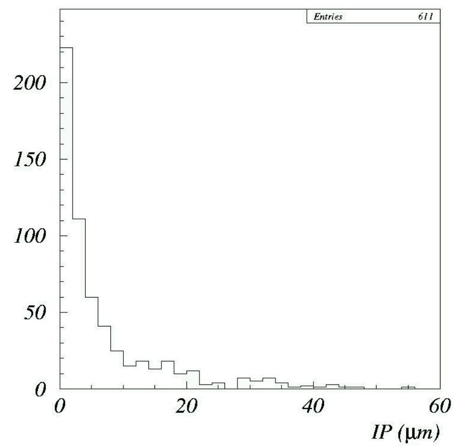

Figure 5.20: Impact parameter distribution of all the tracks attached to the primary vertex.

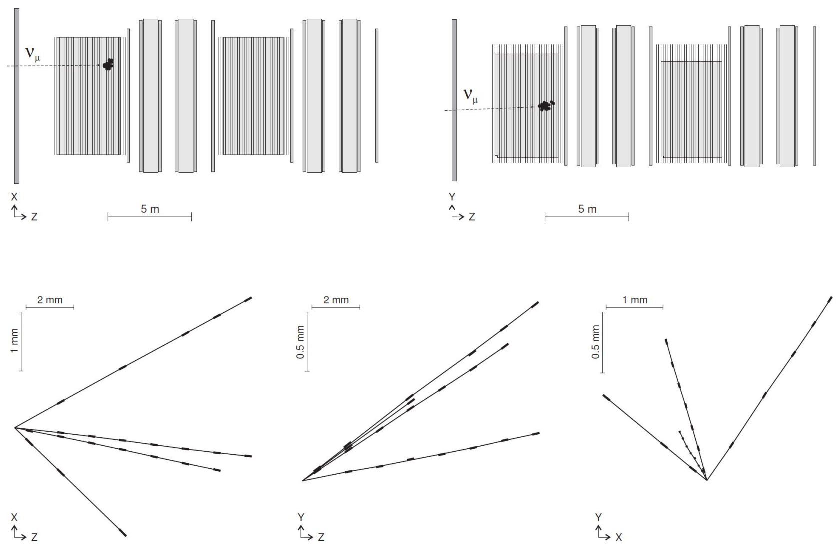

Figure 5.21: Top panels: online display of one NC event seen by the OPERA electronic detectors. The regions filled with bricks are highlighted. Bottom panels: the emulsion reconstruction is shown: top view (left), side view (center), front view (right).

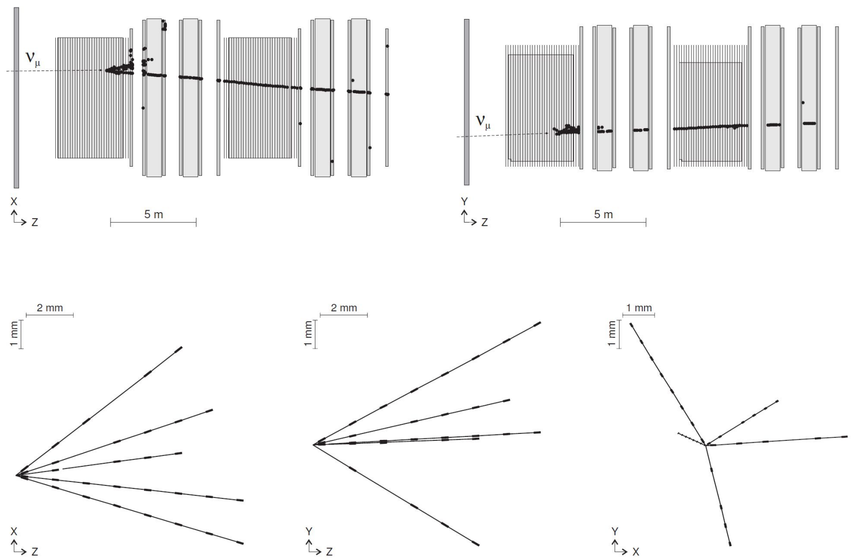

Figure 5.22: Top panels: online display of one CC event seen by the OPERA electronic detectors. Bottom panels: the emulsion reconstruction is shown: top view (left), side view (center), front view (right).

Conclusions

The OPERA experiment is the first "appearance" experiment which should give a final interpretation to a key problem of neutrino physics: if τ neutrinos will be observed in the CNGS beam, the hypothesis of neutrino oscillations will be completely and undoubtly confirmed.

OPERA is a large scale hybrid apparatus equipped with electronic detectors and a highly segmented target section made of *Emulsion Cloud Chamber* (ECC) units. Each emulsion-lead unit, called brick, is composed of nuclear emulsion films interspaced with Pb sheets. The OPERA target is made with $\sim$150000 bricks.

One of the features of the OPERA experiment is the low number of expected background events (less than one event in five years running with a counterpart of $\sim$10 signal events).

One of the challenging tasks of the experiment is the quasi on-line scanning of a large amount of nuclear emulsions which has been accomplished with fully automated optical microscopes, characterized by high scanning speed and high efficiency.

During the 2008 run the number of events classified as interactions in the target were 1663: many bricks were shared among a network of scanning laboratories in Europe and in Japan. The Bologna scanning Lab. is included in the network.

During my research work in the Bologna Lab. I have taken part to the set-up of the automatic scanning microscopes; the first part of this thesis reported on the work which I have done studying and tuning the scanning system performances and efficiencies with emulsions exposed to a test beam at CERN in 2007. The reached scanning speed is $\sim$20 cm^2 per hour, an order of magnitude larger of analogous systems of the past generation. The reconstruction of particle tracks in emulsion is performed at the sub-micrometric level with an efficiency higher than 85% for basetracks (more than 92% at the microtrack level). The corresponding angular resolution is at the level of 1 mrad, better than what is required for a precise reconstruction of a typical tau lepton decay kink.

Once the system had been tuned, the microscopes were used to measure events occurred in the OPERA detector during the first brief physics run performed in the October 2007 and during the 2008 run.

Once the triggered bricks were distributed to the collaboration laboratories, my work was centered on the procedure used for the localization and the reconstruction of neutrino events. I've tested and optimized the procedure used in the Bologna Lab: I have described all the phases of the event reconstruction starting from the matchs between CS and the bricks up to the kinematical reconstruction using as example the first OPERA neutrino event occurred in 2007 which was sent to Bologna and which I have analyzed. The procedures of Scan Back and Total Scan were tested successfully and used on all the bricks received in Bologna during the 2008-run (∼60). In this thesis is also discussed a different procedure based on shower reconstruction used to localize events when the "standard" procedure fails.

Over 70% of the neutrino events delivered to the Bologna laboratory were localized and reconstructed while some events require more analysis, like those located very near to the emulsion edges and so it may be possible that the predicted brick is not the right one.

During the 2008 run the number of expected ν_τ events is 0.6: up to now no tau candidate has been found; there are some events which have not yet been measured in Europe, and more in Japane.

List of Figures

List of Tables

Bibliography

[1] W. Pauli, Fünf Arbeiten zum Ausschlieβungsprinzip und zum Neutrino, Texte zur Forschung Vol. 27, Wissenschaftliche Buchgesell Darmstadt 1977, W. Pauli, On the earlier and more recent history of neutrino (1957) in Neutrino Physics, ed. K. Winter, Cambridge University Press,1991

[2] F. Reines and C.L. Cowan, Nature 178 (1956) 446.

[3] G. Danby et al., Phys. Rew. Lett. 9 (1962) 36.

[4] S.L Glashow, Nucl phys. 22 (1961) 597 ; S. Weinberg, Phys. Rev. Lett. 19 (1967) 1264 ; A. Salam, Proc. of the 8^{th} Nobel Symposium on *Elementary particle theory, relativistic groups and analyticity* edited by N. Svartholm (1969)

[5] B. Kayser, arXiv:hep-ph/0506165 v1, June 16,2005.

[6] Particle Data Group, Physics Letters B 667 (2008) 1

[7] C .Kraus et al., Eur. Phys. J. C40 (2005) 447.

[8] V. Lobashev, Proc. 17th International Conf. on Nucl. Physics in Astrophysics, Debrecen/Hungary, 2002, Nucl. Phys. A 719 (2003) 153.

[9] F. Gatti et al., Nucl. Phys. B (Proc.Suppl.) 91 (2001) 293.

[10] M. Sisti et al., Nucl. Instr. Meth. A520 (2004) 125.

[11] MARE Collaboration, MARE proposal, 19th May 2006. Download at http://mare.dfm.uninsubria.it/frontend/exec.php

[12] H.V. Klapdor et al., MPLA 16(2001) 2409, FP 32(2002) 1181, NIMA 522 (2004), PLB 586 (2004).

[13] Soudan 2 Coll., W.W.M. Allison et al., Phys. Lett. B 391 (1997) 491; Phys. Lett. B 449 (1999) 137; W. Anthony Mann, hep-ex/0007031.

[14] MACRO Coll., S. Ahlen et al., Phys. Lett. B 357 (1995) 481. M. Ambrosio et al., Phys. Lett. B 434 (1998) 451; Phys. Lett. B 478 (2000) 5; Phys. Lett. B 517 (2001) 59; Eur. Phys. J. C36 (2004) 323.

[15] SuperKamiokande Coll., Y.Fukuda et al., Phys. Rev. Lett. 81 (1998) 1562; Phys. Lett. B 433 (1998) 9; Phys. Rev. Lett. 85 (2000) 3999; Nucl. Phys. B Proc. Suppl. 91 (2001) 127; T. Toshito, hep-ex/0105023 (2001).

[16] G.J. Feldman and R.D. Cousins, Phys. Rev. D 57 (1998) 3873.

[17] V. Agrawal et al., Phys. Rev. D53(1996)1314.

[18] G. Battistoni et al., Astrop. Phys. 19(2003)269.

[19] M.Honda et al., Phys. Rev. D64(2001)053011; Phys. Rev. D70(2004)043008.

[20] Y.Declais et al., CERN-SPSC-2002-029 SPSC-059.

[21] R. Bailey et al., CERN-SL/99-034 (DI);INFN/AE-99/05.

[22] M.Komatsu, P.Migliozzi and F.Terranova, J.Phys. G29 (2003) 443.

[23] R.Acquafredda et al., (First events from the CNGS neutrino beam detected in the OPERA experiment) hep/0611023, New J. Phys. 8 (2006) 303

[24] Study of the effects induced by lead on the emulsion films of the OPERA experiment. By OPERA Collaboration, A. Anokhina et al., JINST 3:P07002,2008, arXiv:0805.0123.

[25] Emulsion sheet doublets as interface trackers for the OPERA experiment. By OPERA Collaboration, A. Anokhina et al., JINST 3:P07005,2008, arXiv:0804.1985

[26] Track reconstruction in the emulsion-lead target of the OPERA experiment using the ESS microscope. L. Arrabito et al., JINST 2:P05004,2007, arXiv:0705.3102

[27] Hardware performance of a scanning system for high speed analysis of nuclear emulsions. L. Arrabito et al. Nucl. Instr. Meth. A568 (2006)578.

[28] R.Zimmerman et al. The Precision Tracker of the OPERA detector, Nucl.Instrum.Meth. A 555 435 (2005) [Erratum ibid. A 557 690 (2006)].

[29] M.Guler et al., CERN-SPSC 2008-028, SPSC/P318, LNGS P25/2000, July 10, 2000.

[30] A.J. Apostolakis and J.V.Major, Brit. J. Appl. Phys. 8 (1957) 9.

[31] Tsai-Chu Determination of Distortion Vector in Nuclear Emulsion il Nuovo Cimento, Vol. 5.5, (1957)1128.

[32] S. Aoki et al. Nucl. Instr. And Meth. B51 (1990) 446.

[33] G. Rosa et al., Nucl. Instr. Meth. A394 (1997) 357.

[34] S. Sarkar, Rep. Prog. Phys.59 (1996) 1493, hep-ph/9602260.

[35] High speed particle tracking in nuclear emulsions by last-generation automatic microscopes, N. Armenise et al., Nucl. Instr. Meth. A551 (2005) 261.

[36] Electron/pion separation with an emulsion cloud chamber by using a neural network. L. Arrabito et al. JINST 2:P02001,2007.

[37] H.A. Bethe, Phys. Rev. 89 (1953) 1256.

[38] V.L. Highland, Nucl. Instrum. Methods 129 (1975) 497; Nucl. Instrum. Methods 161 (1979) 171.

[39] A. Borsellino, Phys. Rev. 76 (1953) 1023.

[40] The OPERA experiment in the CERN to Gran Sasso neutrino beam, R. Acquafredda et al. submitted to JINST.

[41] The detection of neutrino interactions in the emulsion/lead target of the OPERA experiment, N.Agafonova et al.